UNIVERSITY OF CALIFORNIA, SAN DIEGO

Hail Ice Damage of Stringer-Stiffened Curved Composite Panels

A Thesis submitted in partial satisfaction of the requirements

for the degree of Master of Science

in

Structural Engineering

by

Jacqueline Linh Le

Committee in Charge:

Professor Hyonny Kim, Chair
Professor Chiara Bisagni
Professor Yael Van Den Einde

2013

The Thesis of Jacqueline Linh Le is approved, and it is acceptable in quality and form for publication on microfilm and electronically:

_____

_____

_____

Chair

University of California, San Diego

2013

DEDICATION

Having lost everything in their possession when they escaped the Viet Cong communist regime in Vietnam in 1981, my parents were forced to start anew when they arrived in their new home country, the United States of America. Since then, they have dedicated their lives to providing me a life full of opportunities to meet interesting people, travel the world, and most importantly, learn. As my father would say, "Education is the only gift we can give you, that no one can rob you of." And for that and so much more, I dedicate this thesis to my parents – Le Trong Uyen and Pham Minh Hue.

TABLE OF CONTENTS

LIST OF ABBREVIATIONS

BVID – Barely Visible Impact Damage

CFRP – Carbon Fiber Reinforced Polymer

FTE – Failure Threshold Energy

NDE – Non-Destructive Evaluation

NDI – Non-Destructive Investigation

SOI – Sight of Impact

SHI – Simulated Hail Ice

LIST OF FIGURES

LIST OF TABLES

ACKNOWLEDGEMENTS

I would like to thank and acknowledge my advisor, Dr. Hyonny Kim, for giving me the opportunity to study under him and guiding me through this research project. I would especially like to thank him for being more than a research advisor, and being a mentor to me. Dr. Kim emphasized the importance of being passionate about my work, whether it be research, design work, or teaching. His patience and guidance has not only aided me through my research, but also in making career decisions.

I would like to acknowledge the full-scale test panels used in this project were manufactured for collaborative research with Stephen Neidigk of Sandia National Labs and Luna Innovations of Blacksburg, VA. I would like to thank Stephen for sharing his research results, which is presented in Section 3.8 Alternative NDE Methods, and his assistance during testing. I would like to acknowledge and thank the FAA William J. Hughes Technical Center for supporting fabrication of the panels. I would also like to thank San Diego Composites for manufacturing the panels.

I would like to acknowledge and thank my lab-mates for helping me prepare for experimentation, as well as maneuver the full-scale panels during testing, especially Daniel Whisler, Mac Delaney, Zhi Chen, Jon Hughes, Isabel Cole, and Sean Luong. The panels were much larger than me; without their assistance, I would not have been able to test.

I would like to thank Scott Ouellette for recommending me to take SE 142: Design of Composite Structures. Had I not been introduced to this class, I would

not have discovered my passion for advanced fiber reinforced composites and had the opportunity to investigate SHI impacting carbon/epoxy panels.

I am grateful to Dr. Yael "Lelli" Van Den Einde for giving me the opportunity to work with her in engineering education research. I am also appreciative of her sharing stories about challenging moments during her doctoral research. It was comforting to know moments of despair and confusion along with joyous epiphanies are a part of the research experience.

Finally, I would like to show my appreciation of my parents and friends, who have provided me with endless moral support throughout my research and trials while writing this thesis. Specifically, I would like to acknowledge the following people: Shelby Royce and Ellen Williams for editing, Jessica Chaisson for reading my mind and assistance with phrasing, Sara White, Lori Jue, and Sam Lee for lending an ear about research moments, and Jacob Gottlieb for drafting and, most notably his patience.

ABSTRACT OF THE THESIS

HAIL ICE DAMAGE OF STRINGER-STIFFENED CURVED COMPOSITE PANELS

by

Jacqueline Linh Le

Master of Science in Structural Engineering

University of California, San Diego, 2013

Professor Hyonny Kim, Chair

Advanced fiber reinforced polymer matrix composite aircraft are highly susceptible to impact damage. One source of impact is hail, which causes matrix cracking, delamination, and fiber breakage. Impacts near joints can cause disbond. Such damage decreases structural integrity, yet can be difficult to detect. Thus, it is important to gain an understanding of impact damage modes and the thresholds at which damage occurs.

Many 61.0 mm diameter simulated hail ice (SHI) impacts at normal incidence angle were performed on full-scale stiffened carbon/epoxy panels to observe what damage resulted as a function of the impact location relative to the stiffeners. The study involved 1.42 m x 1.93 m curved panels made of Toray T800/3900-2 unidirectional carbon/epoxy with 16 ply quasi-isotropic skin, and hat shaped stringers. Impacts were applied at: locations away from the stringers (the middle of the bay), the middle of the stringers, on stringer flanges, and over shear ties. Failure threshold energies (FTE) and the progression of damage modes for each type of impact were established.

Stringer flange impacts were found to be most critical, resulting in flange unzipping with a FTE range of 49-147 J at the free end of the flange, and a FTE of 183 J at the middle of the flange. The resulting damage states were found to be dependent on peripheral boundary conditions affecting local bending stiffness, such as where the skin and stringer stiffeners meet.

1. INTRODUCTION

1.1 MOTIVATION

Aircraft are subjected to a variety of external loads during their service life and they are vulnerable to impacts from several sources such as ground service equipment contact, birds, and hail ice. Many of today's aircraft are manufactured using advanced fiber reinforced polymer matrix composites. Composite application in aircraft started in the 1950s, and initially consisted of only secondary (i.e., not critical) structures. Since then, the use of composites has increased prominently, with composites used for primary structure on the Boeing 737 in the 1980s. Today, composites make up nearly 50% of the structural weight of new generation aircraft such as the Boeing 787 [1]. Despite the widespread use, composites are susceptible to defects and damage reducing its strength and possibly even compromising the structure's integrity.

With a terminal velocity of approximately 30 m/s while falling to the ground, and 200 to 250 m/s while an aircraft is in flight, hail ice impact is a major threat to aircraft (see Figure 1 [2]). In 1995, Dallas Fort Worth experienced a major storm involving hailstones up to the size of grapefruits (approx. 100 mm diameter). Over 100 aircraft parked outdoors were damaged[3]. More recently in July 2011, visible hail damage caused flight cancelation out of Denver International Airport (see Figure 2 [4]).

Figure 1. Hail Damage on Lockheed TriStar 150 [2].

Figure 2. Hail Damage on a Frontier Airlines Aircraft [4].

Hail damage can occur while aircraft are on the ground or in high speed flight at high altitudes. Thus, hail can hit all upward and forward facing surfaces. Hail impact on advanced fiber reinforced polymer matrix composite laminates can result in matrix cracking, delamination, and fiber breakage. Where structural elements are bonded together, hail impact can also lead to disbonded joints. Such damage cannot be easily identified visually. In some cases, the impact may only cause a small indentation on the surface, which is referred to as Barely Visible Impact Damage (BVID), and falls under Category 1 of Damage and Defects [5]. Due to low visual detectability, non-destructive evaluation (NDE) methods are often employed to detect damage. However, any machine-assisted and direct-contact methods can only be used to find non-critical sized damage since, visual detection remains the only practical method of first detection which triggers one to conduct focused NDE of locations of interest.

Since hail impacts can strike anywhere on an aircraft, it is important to observe and understand the formation of ice impact damage on stiffened composite panels. Therefore, the effect of impact location relative to stringer

positions on the resulting damage modes and failure onset thresholds is the focus of this research project. This knowledge allows engineers to design a structure to be resistant against various levels of ice impact threat, and also aids in developing metrics for inspection by having a clear understanding of the damage modes and possible locations. Furthermore, the ability to predict whether non-visible internal damage has occurred or not is instrumental in defining if further inspection of aircraft parts is necessary following hail impact event.

1.2 PREVIOUS WORKS

Hail impact is just one of many different sources of threat. Aircraft are vulnerable to a broad spectrum of impacts: bird strike, hail, runway debris, tool drop, and even incidental contact with ground vehicle [6].

Despite the broad spectrum of impact sources, impacts are generalized/categorized by two extremes of force and displacement responses – static-like impact events and dynamic (wave-dominated) events. Jackson and Poe [7] studied the transition between low and high velocity impacts and highlighted that impact force can be used as a scale parameter for the delamination in simple plates. Low velocity impacts are represented by quasi-static indentation tests and are strongly influenced by boundary conditions. High velocity impacts, on the other hand, are characterized as a truly dynamic event. The response of a structural element due to high velocity impact is governed by local behavior of material neighboring the impacted zone (see Figure 3 [8]). The impact response is generally independent of support conditions because the contact period of the impactor is much smaller than the time period of the lowest

vibrational mode of the structure [7 and 9]. In other words, the peak force develops during projectile-target contact at a much earlier time-scale than the panel's deformation to maximum displacement. By investigating force histories of impact force curves, it was found that impact force is independent of boundary conditions in cases of high velocity small mass. This impact force varies with mass and velocity while kinetic energy is constant. Similarly, transverse shear force varies with mass and velocity while the impactor force is constant. Due to this dynamic nature of high velocity impacts with small mass, Jackson and Poe determined neither kinetic energy nor impactor force can be the sole parameter of damage initiation and damage area prediction in high velocity impacts.

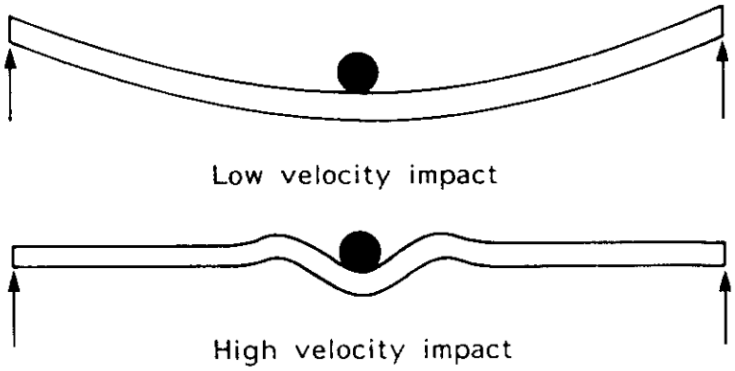

Figure 3. Transverse Impact Load Response [8].

A large body of research emphasizing in low velocity impacts has been done on impacts on composites. Zhang [10] and Davies and Zhang [11] proposed the relationship between threshold load and the initiation of delamination and the thickness of a laminate to be $t^{2/3}$. Through experimentation, Schoeppner and Abrate [12] were able to verify this relationship and show the effects of various parameters on low velocity impacts on the damage threshold. In addition, Davies

and Zhang [10] were able to confirm the application and relevance of applying damage threshold studies on carbon composites coupon tests to realistic structures by testing small coupons and using the corresponding test data to calibrate finite element models. They were able to conclude that failure threshold data of small coupons applied to larger scale structures for damage initiation prediction worked well for carbon composites [10].

In regards to high velocity impacts, research has been carried out on bird strike and hail ice impacts. These two studies range in velocity, deformability of the projectile upon impact, and contact area. They are considered soft-body impacts particularly for birds, and semi-soft for hail (initial behavior is elastic) [13]. The impactor's deformability presents a complex problem due to its time dependent force distribution [14]. Within this velocity regime, energy levels are varied by adjusting the projectile's mass and velocity to find the FTE and to understand the different levels of damage.

Bird strike research has been carried out through experimentation using gel packs and FEA modeling. Hou and Ruiz [14] identified damage initiation velocities and damage progression of bird strike on a variety of composite plate materials including Toray T800H/3900-2. This literature on damage initiation velocities and other experimental results have been used in efforts to validate FEA modeling by Johnson and Holzapfel [15], and Smojver and Ivancevic[16]. Most recently, bird strike FEA models were successfully validated for the Boeing 787 compliance trailing edge by Georgiadis et al. [17].

Kim et al. [18] investigated the effects of hail ice impacts to woven carbon/epoxy composite laminates. FTE values were established and the progression of damage modes due to hail ice impacts with diameters ranging from 25.4 mm to 50.8 mm were discussed. It was concluded that high velocity hail ice impacts are inherently dynamic events, producing very localized deformation at the time of damage initiation (within 100 μs at first contact), and thus the measured FTE and observed damage modes are not highly effected by the panel boundary conditions. Further, it was established that the FTE is directly related to the panel thickness and simulated hail ice (SHI) diameter. Similarly, Rhymer et al. [19] studied FTE values of quasi-isotropic carbon/epoxy composite tape laminates and compared the damage modes to those of woven carbon/epoxy composites by testing 305 mm x 305 mm framed panels. FTE values from Rhymer et al.'s findings have been summarized in Table 1. Rhymer et al. concluded that (i) the FTE data of woven carbon/epoxy and carbon/epoxy tape materials are essentially the same, (ii) the FTE values are linearly related to the ratio of panel thickness to SHI diameter, and (iii) initial damage of carbon/epoxy material is circular but as the damage grows larger, the shape of the delaminated area is dependent on the material. Damage in the tape material grew lengthwise along the 90° axis, while damage in the woven material remained roughly circular.

Table 1. FTE Values of Carbon/Epoxy Composite Tape Laminate Plates [19]

Panel Type (Thickness)	SHI Diameter	Mean FTE Value [J]	FTE Value (10% Threshold) [J]	FTV Value (10% Threshold) [m/s]
8 ply (1.59 mm)	38.1 mm	211	172	115
	50.8 mm	259	258	91
	61.0 mm	226	223	65
16 ply (3.11 mm)	38.1 mm	369	311	154
	50.8 mm	456	456	121
	61.0 mm	507	489	96
24 ply (4.66 mm)	38.1 mm	415	413	178
	50.8 mm	736	733	154
	61.0 mm	938	865	127

In addition to understanding the effects of SHI on monolithic carbon/epoxy plates, the effects of SHI on adhesively bonded composite joints (single lap joints) have been studied. In [20 and 21], the FTE of a single lap joint made of unidirectional carbon/epoxy prepreg (Hexcel F155) was found to be 210 J, which is comparatively less than the FTE of a monolithic plate made of the same material. Within the range of 210 and 250 J, small damage often localized in the overlap region was initiated and spread towards the bondline on the back side of the joint (non-impacted side) and away from the impact site. Impacts greater than 250 J showed widespread delamination of the joint with delamination in the plies adjacent to the adhesive layer being dominant.

Other investigations of joints have been carried out by Kairous and Matthews' [22] and Kim et al. (low velocity) [23]. Through experimentation of glass/epoxy bonded lap joints, Kim et al. [23] identified the following damage progression modes: matrix cracking, fiber failure, localized debonding, and global

debonding. Kairouz and Matthews' [22] observed interlaminar failures (i.e. within the adherends) and no cohesive failures. Other authors have researched impacts on joints, but the majority have studied in-plane loads in oppose to transverse loads [20]. Understanding the effects of impacts on joints is critical for predicting damage initiation and damage progression where structural elements are joined together.

Little work has been done to investigate the effects of impacts on stiffened panels, and even fewer only considering those with soft-body impacts. Greenhalgh et al. [24 and 25] studied the residual compressive strength of stringer-stiffened CFRP panels that were previously damaged by low velocity low mass impacts (representing tool drop) and by embedded defects (representing inclusions during manufacturing). It was observed that the presence of the impact damage in the mid-bay region led to a 7% strength reduction, while impact damage on the stringer flange led to a 29% strength reduction. The damage scans and observations from these experiments were then used to develop an FEA model to predict damage [26]. Similar experimentation was performed by Suh et al. [27] with unstitched, partially stitched, and fully stitched stringer-stiffened impacts. This work looked into the overall strength of stiffened panels given pre-existing impact damage. The current study explores damage initiation energy levels and the progression of damage modes as a function of impact location relative to stiffeners.

1.3 OBJECTIVES

This investigation explores SHI projectile impacts onto full-scale stringer stiffened curved panels in order to observe the interaction between the different components. In particular, FTEs and damage mode progression for impacts at the middle of the bay, the middle of the stringer, the stringer flange, and directly over the shear tie will be identified. The findings will be used to establish scaling factors between FTEs and impact data of monolithic panels, and FTE and impact data of stringer-stiffened panels made of the same material and layup. In the current study, the panels skins were 16-ply quasi-isotropic and made of Toray T800/3900-2 graphite/epoxy unidirectional prepreg tape.

2. EXPERIMENTAL SETUP

Experiments were carried out to better understand damage initiated by SHI as a function of the impact location relative to stiffeners. Full-scale stringer-stiffened curved panels were impacted with 61.0 mm SHI. Impacts were made at the middle of the stringer, the stringer flange, the middle of the bay, and directly over the shear tie to observe the interaction between the components. To maintain realistic conditions of detecting damage of an in-service aircraft, only portable non-destructive investigation methods suitable to in-service inspections were used.

2.1 FABRICATION OF SHI PROJECTILES

Ice spheres with a diameter of 61.0 mm were fabricated to simulate hail projectiles. These SHI were created using split aluminum molds. Distilled water was injected into each mold using a syringe. The molds were then set in a freezer operating between -5 ° (23 °F) and -12 °C (1.4 °F). After a minimum of six hours freezing time, each SHI was removed from its mold and placed in a ZIPLOCK and stored in the freezer. The detailed procedure for SHI fabrication can be found in Appendix A.

Prior to impacting the full size panels, a study was done to refine 61.0 mm SHI manufacturing. The objective was to develop a procedure that would create a consistent projectile and to decrease the rejection rate of SHIs. The previous SHI manufacturing method, which can also be found in Appendix A, had a 50% rejection rate due to various reasons: ice cracking, hemispheric cracks, and non-

homogeneous ice consistency such as elongated ice bubbles in clear ice (See Figure 4a-4c).

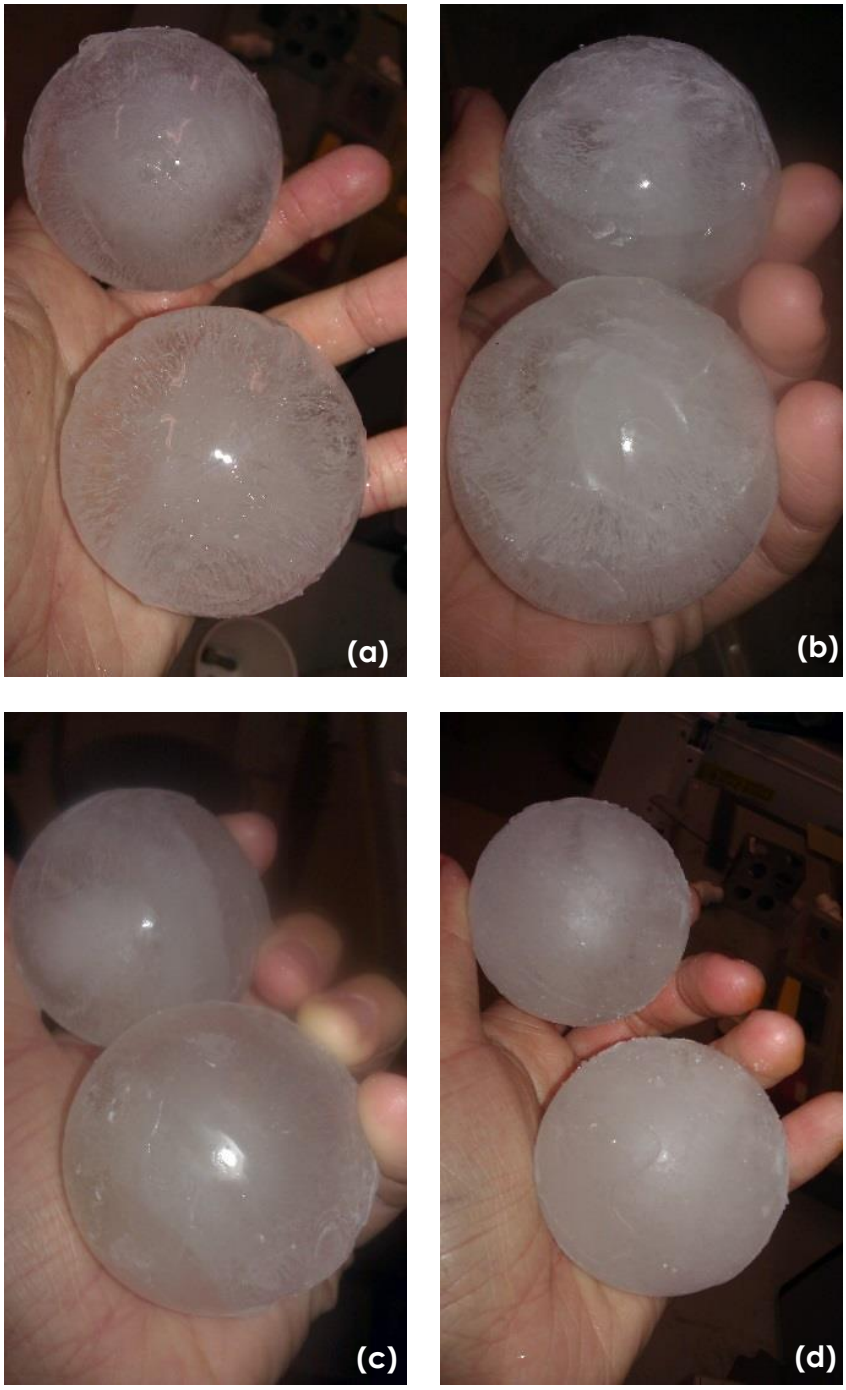

Figure 4. (a) SHI with Radial Ice Bubbles, (b) Crushed SHI, (c) SHI with Hemispheric Cracks, (d) Homogeneous SHI.

Variables that affected the quality of ice include the quality of water used, and the temperature and rate at which the water was frozen [28 and 29]. The quality of ice produced was highly dependent on the quality of water used. The cleaner and purer the water, the clearer the ice would be. Previously, deionized water was used for the production of SHI. De-ionized (DI) water can contain remnants from de-ionizing resins[30]. Distilled water, on the other hand, is water vapor that has been returned to its liquid state. Contaminants have been removed from the water in the distillation process. Rejection rate decreased dramatically when distilled water was used.

Elongated bubbles in ice, such as those in Figure 4a, were caused by entrapped air in the water. As water freezes, it pushes cold water towards the center; thus, causing the air bubbles to elongate. This was resolved by boiling distilled water to remove any entrapped air. In addition, extra care was taken to refrain from creating a turbulent stream by slowly injecting water into the mold. In cases where turbulence was created, excess water was injected until visible bubbles overfilled the cavity and was removed.

SHI was manufactured in a solid aluminum mold that was tightly clamped shut, which meant it was subjected to a compressive force due to the confinement of the mold as the water expanded while freezing. This presented several problems. As the water continues to freeze, the water pushes the mold apart and relieves pressure at the mold split line causing hemispheric cracks, or the cold water pushes towards the water injection hole and crushes the ice at the top of the SHI. To prevent the water from pushing the mold pieces apart and

escaping through the gap, a thin layer of petroleum jelly was applied around the rim of the mold to create a seal. The mold was then closed and hammered over locations where the petroleum jelly was applied to secure the sealant between the mold halves.

In order to address the ice crushing issue and the non-homogeneous nature (i.e., inconsistent crystal ice structure) of the SHI, several adjustments were made. The SHI originally was placed in a freezer at -15 °C (5 °F). This temperature produced too quick of a cooling rate and high temperature gradients, which caused the outside region of the ice to freeze much faster than the interior. Furthermore, when re-casting a new set of ice spheres the aluminum mold and the steel c-clamps were originally immediately employed soon after being removed from the freezer and the prior spheres extracted. This was problematic because these parts were much colder than the water, thus contributing to chilling the water along the outer surface of the sphere more quickly. Based on these observations, a slow and consistent rate of freezing for the whole system (both mold and ice) was critical. Thus, one adjustment of the process was to warm up the mold and c-clamp using warm/hot water prior to filling the molds with distilled water. To further reduce the thermal gradient, the freezer temperature was monitored and adjusted to be as close to 0 °C (32 °F) as possible. Although 0 °C (32 °F) is ideal, the equipment only allowed for -5 °C (23 °F). These adjustments helped to allow the whole system to slowly decrease its temperature and freeze together at the same time (i.e. with less temperature gradients from the outer surface to inner core).

Another important aspect of manufacturing SHI is the mold removal process. The contact of water and ice causes cracking and thus, should be avoided. Further, it is important to warm up portions of the mold evenly. As the steel clamps and aluminum mold pieces expand in the warming process, the compression force between the SHI and the mold can become uneven and also cause cracking. Only minor changes, such as taking extra care to avoid water and ice contact, were made to the mold removal process in order to reduce cracking and inconsistency.

The changes discussed proved to be successful in fabricating SHI with homogeneous crystal structure and decreased the rejection rate of SHI to approximately 20%. Similar methods with changes to the amount of water removed in Step 10 (see Appendix A) have been applied to the manufacturing process of 12.7mm, 38.1 mm, and 50.8 mm SHI and have similarly been successful.

2.2 FABRICATION OF SABOTS

Sabots were used to house and secure (see Figure 5 [31]) each SHI as it travels through the gun barrel, and also to provide insulation between the ice and room-temperature metal barrel (contact would cause melting). These sabots were made of Smooth-On's Foam-It 10, a rigid polyurethane foam with a density of 10 pcf (160 kg/m^3). Foam-It 10 is composed of two parts: a liquid and a hardener. At a one-to-one ratio, the Foam-It 10 was mixed and poured into an aluminum and steel mold. After setting for a minimum of two hours, the foam was removed from its mold and sliced in half length-wise. A rubber o-ring was then placed around the halves to hold the sabot together.

Figure 5. Sabots Housing SHI [31].

2.3 TEST SPECIMENS

Two curved panels (see Figure 6) were manufactured to investigate high velocity SHI impacts damage to stringer-stiffened configurations and to study results of various NDI techniques, which was carried out by Stephen Neidigk of Sandia National Labs. A brief comparison of results is presented in Section 3.8. The panels were designed to resemble full-scale sections of modern composite aircraft fuselage. The geometric makeup of the two panels were exactly alike. The panels were made of Toray T800/3900-2 graphite/epoxy unidirectional prepreg tape (a.k.a. Boeing specification BMS8-276 N) material for the skin and co-cured stringers, and a 6K plain weave for the shear ties. To better represent an aircraft section, the panels had an additional layer 0.05 mm (0.002 in) thick Toray glass/epoxy plain weave (BMS8-331) on the impact side and were painted on the exterior with white aerospace grade paint. The specimens were fabricated and painted by San Diego Composites based on UCSD's specified design shown in Figure 7 to Figure 9.

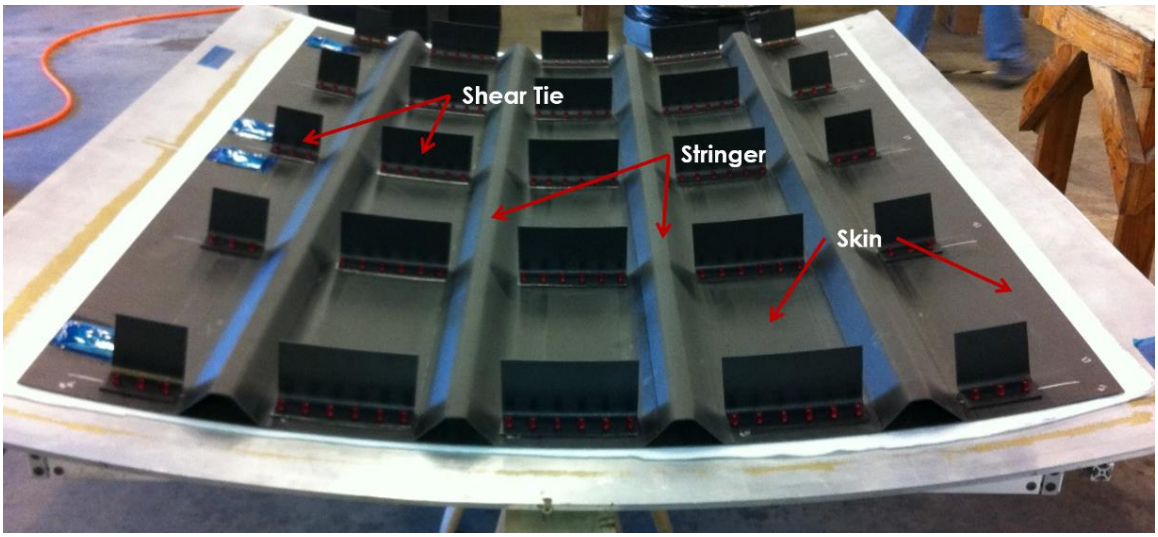

Figure 6. Backside of Full-scale Curved Panel.

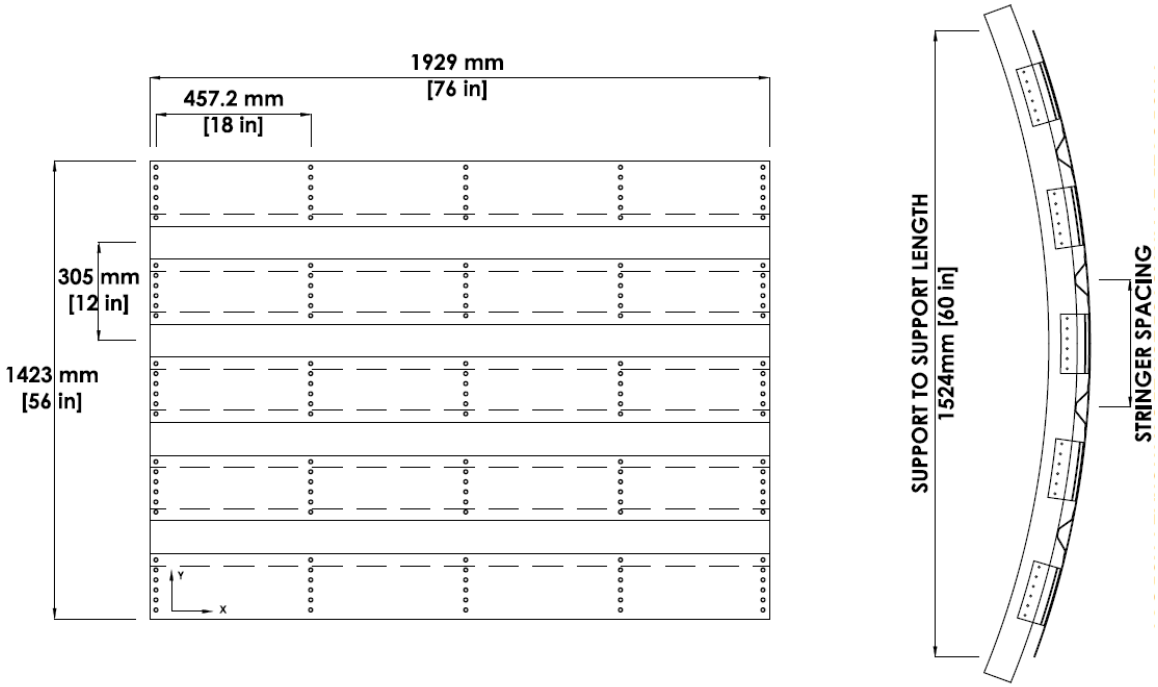

Figure 7. Panel Overall Dimensions.

The overall dimensions of the panels were 1.42 m x 1.93 m (56 in x 76 in). Each panel had four hat-shaped stiffeners spaced 305 mm (12 in) apart. In addition, there were five rows of shear ties spaced equally along the length of the

panel, with each row having five shear ties (25 total). Shims with equal thickness to the stringer flange were placed between shear ties and the flange, to create a flush surface to bolt shear ties to the skin. Details of the layup of these components are shown below in Table 2. The stringers had 38.1 mm (1.5 in) wide tapered flanges. The flanges had a uniform thickness for 19 mm (0.75 in) and taper off at 2.54 mm (0.1 in) increments. The rows of shear ties were placed 457.2 mm (18 in) apart. The geometry of each of these comments are provided in Figure 8 and Figure 9.

Table 2. Component Layup Schedule

Component	Material	Layup	Thickness
Skin	Glass, T800 tape	$[glass[(0/45/90/-45)_2]_s]$	3.18 mm (0.125 in)
Stringer	T800 tape	$[0/45/-45/90/45/-45/0]_s$	3.25 mm (0.128 in)
Shear Tie	T800 fabric	$[\pm45/0/90]_3[0/90/\pm45]_3$	2.9 mm (0.11 in)
Shim	T800 tape	$[0/45/-45/90/45/-45/0]_s$	3.25 mm (0.128 in)

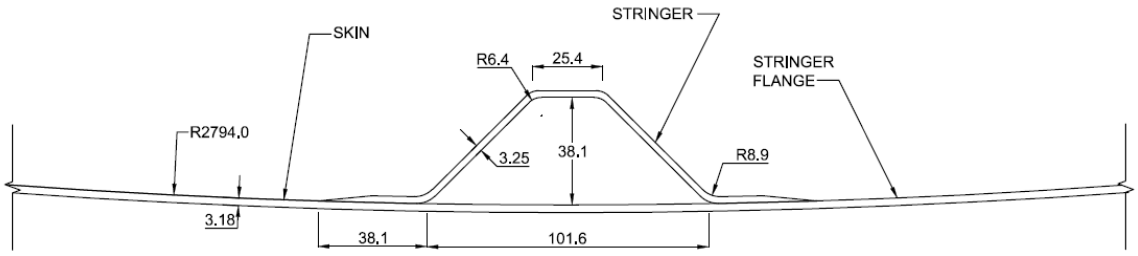

Figure 8. Stringer with Tapered Flange Geometry. (All Dimensions in mm.)

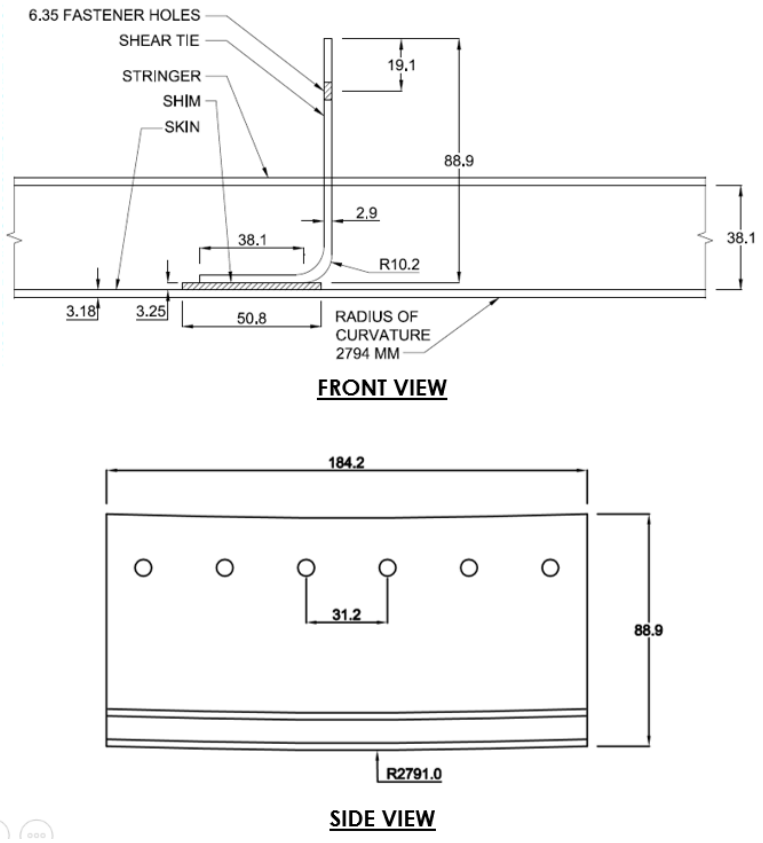

Figure 9. Shear Tie Geometry (All Dimensions in mm).

80 micron polyimide coated telecom grade fiber optic was incorporated into both panels. The fiber was embedded between the eleventh and twelfth Toray tape layers (not counting thin woven glass surface ply) of the first panel (Panel A). It was at approximately 75% depth away from the impact surface. For the second panel (Panel B), the fiber was bonded to the back surface of the skin after the panel was cured and the shear ties were mounted. See Figure 10 for the fiber optic layout of both panels. Luna Innovations of Blacksburg, VA installed the fiber optics and conducted the data acquisition during testing at UCSD.

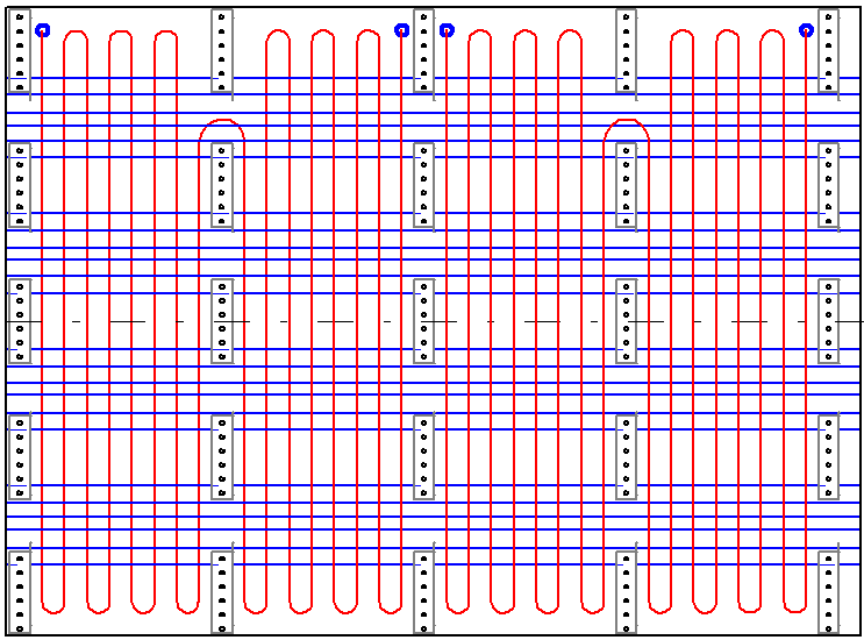

Figure 10. Fiber Optics Cable Path with Panel A Embedded and Panel B on Inside Surface (Away from Impact Side).

2.4 TEST FIXTURES

Since high velocity impacts excite localized dynamic response, and thus cause local damage [7 and 9], the global boundary conditions are not critical. Five 2024 aluminum frames 6.35 mm (0.25 in.) thick and approx. 1.7 m (67 in) representing the hoop-wise stiffness of the fuselage frames, were mounted to the shear ties as shown in Figure 12. These aluminum frames were clamped to the vertical test fixture (hold panel upright during impact) using c-clamps (see Figure 11). To help support the weight of the specimen, a stand was added on the side, which was not supported by the vertical test fixture, as shown in Figure 11.

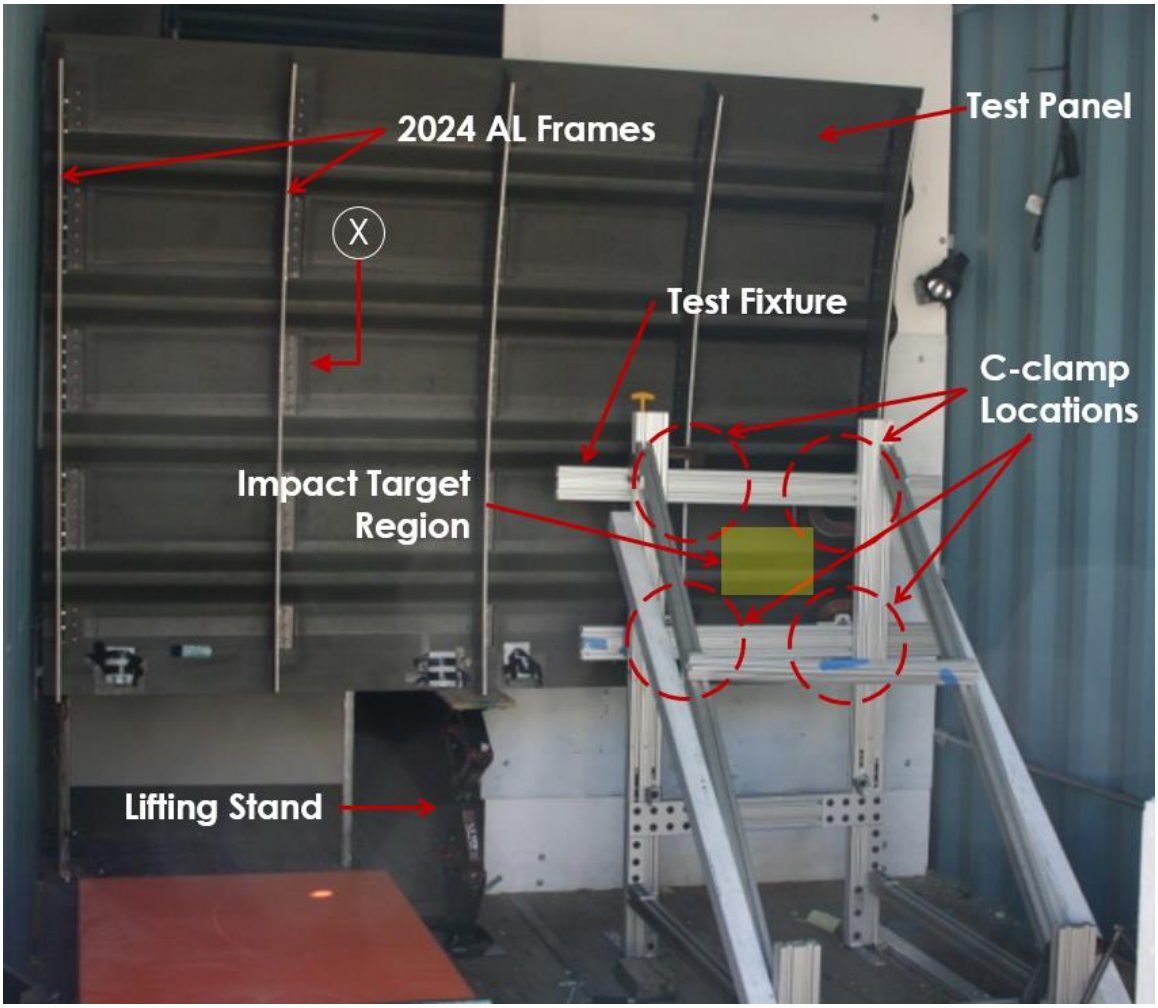

Figure 11. Test Fixture for Full-Scale Curved Panels.

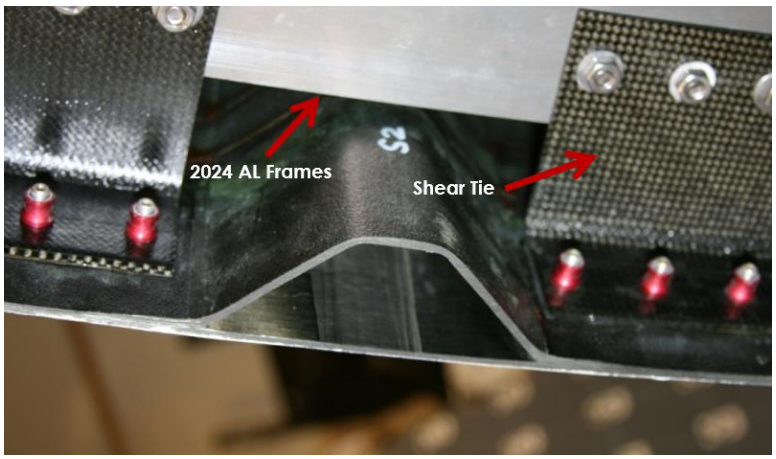

Figure 12. SECTION X: Aluminum Frame Mounted to Shear Tie.

2.5 TEST EQUIPMENT

2.5.1. Gas Gun

SHI were projected using the UC San Diego Gas Gun shown in [31]. This gas gun has six major components: the propellant gas tank, the pressure tank, the ball valve, the breech, the barrel, and the sabot stopper. The pressure tank was filled with nitrogen or helium to pressures up to 6.9 MPa (1000 psi). SHI was placed into sabots, and then the combined projectile package was placed into the breach. When the gun is fired, the ball valve opens via a fast ball valve (driven pneumatically with helium) the gas from the propellant gas tank. This gas expands and exerts pressure onto the projectile package, thereby accelerating it through the 79.3 mm diameter x 2.3 m (3.122 in dia. x 90 in) barrel. Soon after exiting the barrel, the sabot aerodynamically opens slightly before it encounters the sabot stop plate and is kept behind, as the SHI continues to project forward through the velocity measurement system towards the target. A laser mounted concentric with the barrel was used to verify the exact target location prior to impact.

Figure 13. UC San Diego Gas Gun [31].

2.5.2. Velocity Measurement System

A laser photogate system sits at the end of the gas gun setup between the sabot stop and the target. The system is monitored by a 2 channel oscilloscope to determine the velocity of the SHI just before impacting the target. The oscilloscope measures the time, t, between the ball entering and exiting the photogate with a tolerance of ± 1.0%. The distance, d, between the two lasers is 127.5 ± 0.1 mm. Velocity, V, of the SHI prior to impacting the target can be calculated using Eq. (1) with a tolerance of 1.0% per Eq. (2).

$$v = \frac{127.5\ mm}{t}, \left[\frac{m}{s}\right], \text{ with t in units [ms]} \quad (1)$$

$$\frac{\delta v}{v} = \sqrt{\frac{\delta d^2}{t} + \frac{\delta t^2}{t}} \quad (2)$$

2.5.3. High-Speed Video Camera

A Phantom v7.3 digital high-speed camera was used during testing. Set to rates between 7,000 – 15,000 frames per second, the video was used to verify the structural integrity of the ice ball prior to hitting the specimen and also to observe the initial point of contact between the ice ball and the specimen. The video also acted as a redundant method to determining the velocity of the SHI.

2.5.4. Weight Measurement and Timing

An Ohaus Scout Pro SP 20001 scale was used to determine the mass of the SHI. This was done by measuring the empty sabot, and the combined mass of the SHI and the sabot. By subtracting the sabot's mass from the combined mass, the SHI mass, m, was found. The digital scale had a tolerance of ± 0.1 grams, which is

approximately 0.2% of the measured mass. Using this acquired mass, m, along with the velocity, v, from Eq. (1), impact energy, E, was determined via Eq. (3). This led to an error of up to 2.0% in impact energy from Eq. (4).

$$E = \frac{1}{2}mv^2 \tag{3}$$

$$\frac{\delta E}{E} = \sqrt{2\left(\frac{\delta v}{v}\right)^2 + \frac{\delta m^2}{m}} \tag{4}$$

Time between SHI being removed from the freezer and being shot was measured to avoid SHI melting. This time was targeted to be less than or equal to 3 minutes.

2.5.5. Ultrasonic UT A-Scan

A portable ultrasonic testing system (NDT Automation PocketUT) was used during and post impact testing to detect and map delamination by A-scanning. The A-scan used a 5 MHz general purpose contact transducer (NDT Automation CBRZ5X2 SN:282) in the pulse-echo mode.

2.5.6. Testing Procedure

The following procedure was followed during conduct of the tests to provide uniform conditions for each impact. SHI and sabots were weighed and placed back in the freezer. Impact locations were located and marked with a red X on the specimen. The curved panel was then placed on the test fixture, the target X was aligned with the laser, and the panel was secured to the vertical test fixture with c-clamps. The high speed camera and velocity measurement systems were then set to trigger. Next, the timer was started as the ice was removed from

the freezer. The SHI was then placed in the breach of the gun. The breach was secured, the pressure chambers pressurized, and finally the SHI was launched once the desired pressure was achieved.

After the SHI was shot, the breach was opened and test data files were saved. The sight of impact (SOI) and the area around it were inspected for visible damage, tactile damage (i.e., feeling for damage using figure-touch), and delamination. If extensive visible damage or delamination was found, the curved panel is relocated to a new target. If no such damage was found, the same impact site was tested again at a higher energy level. Each impact site was tested up to three times. Post testing, the panels were carefully A-scanned to map delamination areas.

2.6 IMPACT LOCATIONS

SHI impacts were made at the middle of the bay (I), end of the stringer flange (IIa), middle of the stringer flange (IIb), middle of the stringer (III), and directly over the shear ties (IV) to observe the interaction between the different components. Impact locations are defined in Figure 14. Results from these impacts were used to identify the FTE, as well as the damage progression for each type of impact.

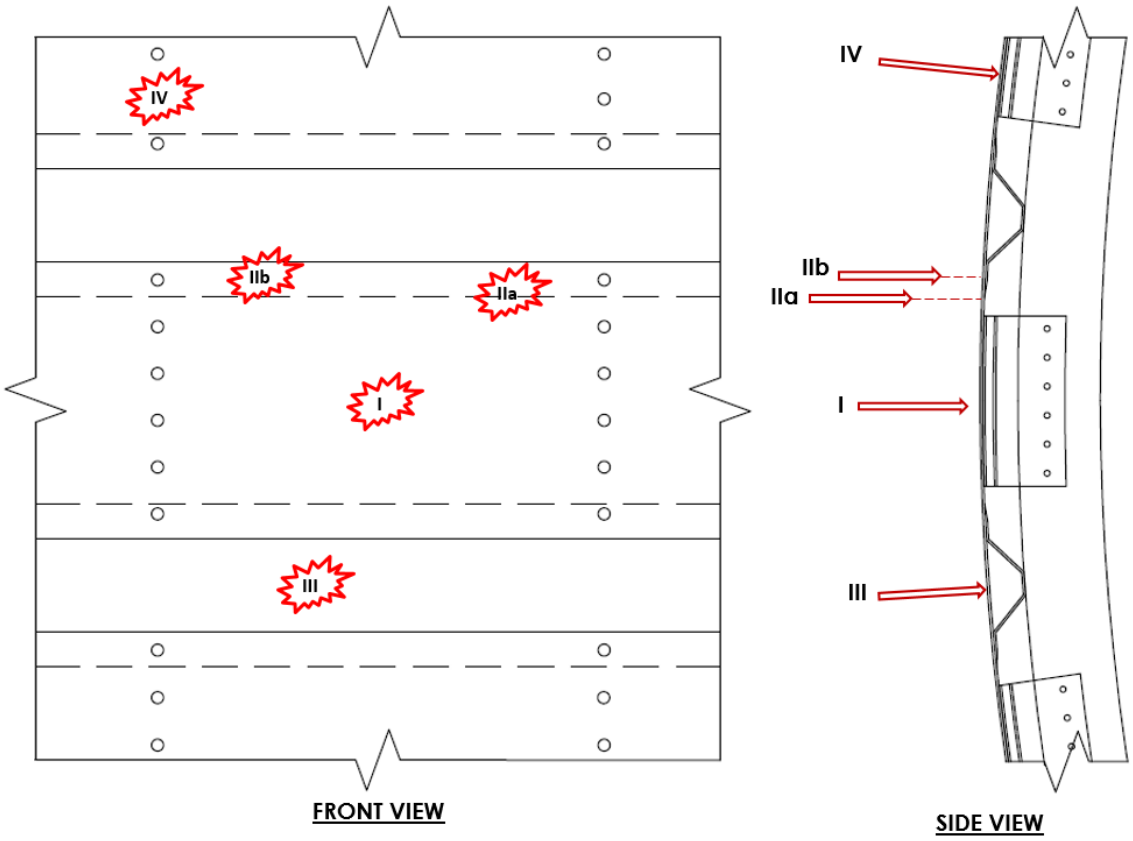

Figure 14. Types of Impact Locations. (I) Middle of the Bay, (IIa) End of Stringer Flange, (IIb) Middle of Stringer Flange, (III) Middle of Stringer, and (IV) on Shear Tie.

2.7 TEST MATRIX

Two quadrants on each of the curved panels were impacted with 61.0 mm SHI. The remaining two quadrants were preserved to be tested with other types of impacts (low velocity and hard metal tips) by Sandia National Labs. These quadrants are shown in Figure 15. The test matrix was developed to focus on damage caused by mid-bay and mid-flange impacts (Types I and IIb). Impacts on the edge of the flange (Type IIa), mid-stringer (Type III), and shear tie (Type IV) were added to compare the severity of damage caused by the variety of impact

locations. The number of tests conducted at each location is summarized in Table 3.

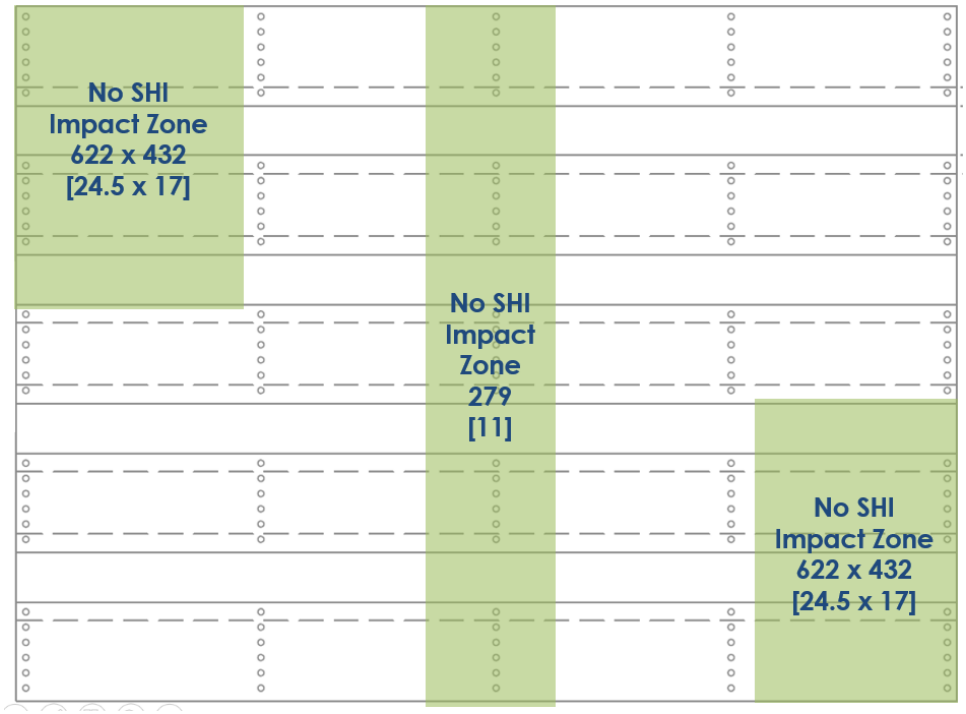

Figure 15. No SHI Impact Zones of Panel (All Dimensions in mm [in]).

Table 3. Test Matrix for Impact Location

Impact Location	No. of Tests
I – Middle of Bay	19
IIa – End of Stringer Flange	2
IIb- Middle of Stringer Flange	13
III – Middle of Stringer	6
IV – Directly Over Shear Tie	5

3. EXPERIMENTAL RESULTS AND DISCUSSION

Data regarding projectile mass and velocity was processed to determine impact energy using Eq. (3) after each experimentation session. In addition, delamination area was mapped using A-scan. These results were analyzed in order to identify FTE and damage progression for each type of impact. Sections 3.1 through 3.3 of this chapter present the methods used for damage mapping, establishing FTE, and damage progression. The remainder of the chapter presents results and a discussion of the individual types of impacts. Discussion of the overall results are covered in Chapter 4.

3.1 DAMAGE AREA MAPPING

Post testing, SOIs and their surrounding areas were inspected using A-scan, visual observation, and tactile sensation (feeling for surface cracks using finger tips). Delamination detected by A-scan was mapped on the painted side of the panel, by finding the extents of delamination and outlining it using permanent ink markers. Each SOI was labeled with its test numbers and its x- and y- coordinates on the panel face. A 1 cm scale was marked with each label. Photographs of the front and back sides were taken of each SOI to document the damage. A compilation of the photographs can be found in Appendix E. Photographs of the delaminated areas were imported into Bluebeam Revu (a PDF creation, markup, and editing software). Delamination area was then calculated based on the 1 cm scale. Any damage visually and/or tactilely detected from the backside of

the panel was highlighted using a silver paint pen, but was not included in delamination area calculations.

3.2 FAILURE THRESHOLD ENERGY (FTE)

Two methods were utilized to identify the FTE of each type (location) of impact. One method was to plot the delamination area versus the impact energy and select the range between which small delaminations transition to large delaminations. Another method was using a binomial logistic regression together with binary graphs of damage detection versus energy level. The number one (1) was assigned to test cases where delamination was detected and zero (0) was assigned to test cases where delamination was not detected. The binomial regression analysis quantitatively allowed for finding the energy level at which damage occurs.

Once the FTE was identified, it was compared to the baseline FTE of 489 J, which has been measured by ice impacts onto flat 305 x 305 mm carbon/epoxies with fixed boundary condition [19].

3.3 DAMAGE PROGRESSION

The various impact locations, namely impacts on the skin, stringers, stringer flanges, and shear ties, generally behaved differently and thus, can exhibit different modes of damage. Because the structural elements (i.e., stringers and shear ties) each have different stiffness levels, they influence the local behavior of the panel depending on their location relative to the SOI. Damage types include

delamination at the SOI and around the SOI, nearly full delamination of the stringer flange, and backside fiber breakage.

3.4 MIDDLE OF THE BAY IMPACTS (TYPE I)

3.4.1. Experimental Results

Middle of the bay (mid-bay) impacts caused the skin within the bay to deflect out-of-plane, thus causing delamination at the SOI (in the skin) and/or delamination between the stringer flange and the skin. Delamination was measured in three manners: (1) delamination area at the SOI (in skin), (2) stringer flange delamination from the skin, and (3) total delamination area (see Figure 16). The delaminated area of each of these have been summarize in Table 4 (ordered by increasing energy).

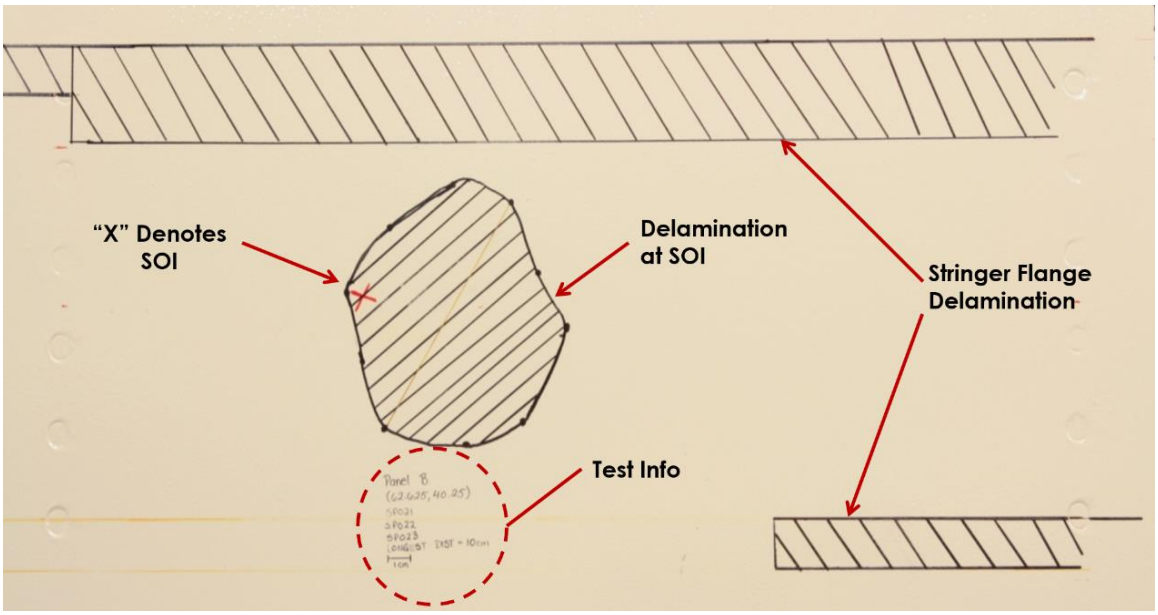

Figure 16. Areas of Delamination Due to Type I Mid-Bay Impacts.

Table 4. Middle of the Bay Impact (Type I) Delamination Area Summary

Test No.-Panel	SHI Mass [g]	Velocity [m/s]	Impact Energy [J]	Delamination Area at SOI [mm^2]	Further Delamination Area [mm^2]	Total Delamination Area [mm^2]
SP043-A	107.0	54.9	161.2	0	0	0
SP044-A	100.3	67.3	227.0	3000	7900	10900
SP042-A	106.9	74.3	295.4	1500	0	1500
SP002-A	104.9	76.5	307.2	0	0	0
SP045-A	99.8	83.4	347.1	0	7900	7900
SP003-A	107.3	89.6	430.7	0	0	0
SP024-B	108.3	89.4	432.9	0	0	0
SP021-B	106.7	91.3	445.0	0	0	0
SP004-A	109.1	91.1	460.3	0	0	0
SP025-B[ǂ]	108.5	100.7	N/A	--	--	--
SP022-B	105.8	101.0	540.0	0	0	0
SP005-A	108.0	100.6	546.8	0	3100	3100
SP010-B	108.1	102.0	562.3	5000	5300	10300
SP008-A	108.9	102.0	566.5	0	0	0
SP023-B	108.1	111.0	665.5	6800	18100	24900
SP009-A	105.9	116.7	720.5	31700	8700	40400
SP026-B	107.4	117.0	734.8	14000	18300	32300
SP011-B	106.2	118.5	745.6	12500	900	13400
SP001-A[ǂ]	107.0	N/A	N/A	--	--	--

[ǂ] Denotes test was omitted due to SHI breaking prior to hitting target

Using the data in Table 4, delamination area was plotted in Figure 17 versus impact energy to find the FTE of mid-bay impacts for (1) delamination area at SOI, (2) further delamination away from the SOI, and (3) total delamination area. Tests SP042 and SP044 produced delamination at the SOI at much lower energies than expected. To be conservative, FTE of Type I is defined as a range between 227 to 567 J. This is inclusive of delamination at the SOI and further away from the SOI. From the point of view of the SOI delamination area, the FTE (subjectively) seems to be at approximately 550 J, resulting in a 1.12 scaling factor. This is close to the 489 J baseline value, with the higher energy here likely due to boundary condition

effects of the 267 x 267 mm support span for the 305 x 305 mm panels used to measure the baseline. For the point of view of around the SOI (namely, delamination of the stringer flanges surrounding the bay), the FTE is considerably lower, at approximately 227 J. This equates to a 0.46 scaling factor. Impact energies greater than 567 J produced extensive delamination in both the skin at the SOI and between the stringer flanges and skin located away from the SOI.

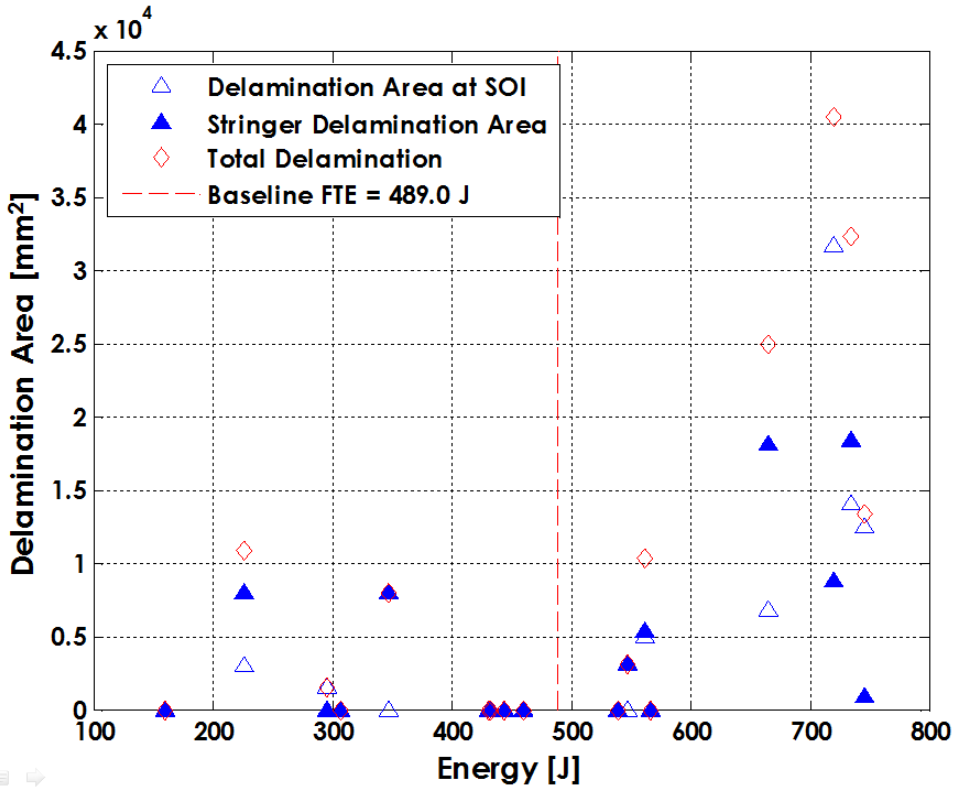

Figure 17. Middle of the Bay Impacts (Type I): Delamination Area Versus Energy Plot.

No apparent damage occurred for impacts with energy levels below the defined FTE range. At impact energies greater than the FTE range, a variation in progression of damage modes were observed depending on whether the impact

was applied to a pristine location (previously not impacted site) or to a previously impacted location.

For pristine locations, impact energy close to the FTE range caused small delamination at the SOI (see Figure 18). Impact energies slightly higher resulted in delamination in the nearest stringer flange. As depicted in Figure 19, energy levels much greater than FTE caused delamination in the stringer flange nearest to the SOI, in addition to the delamination described previously.

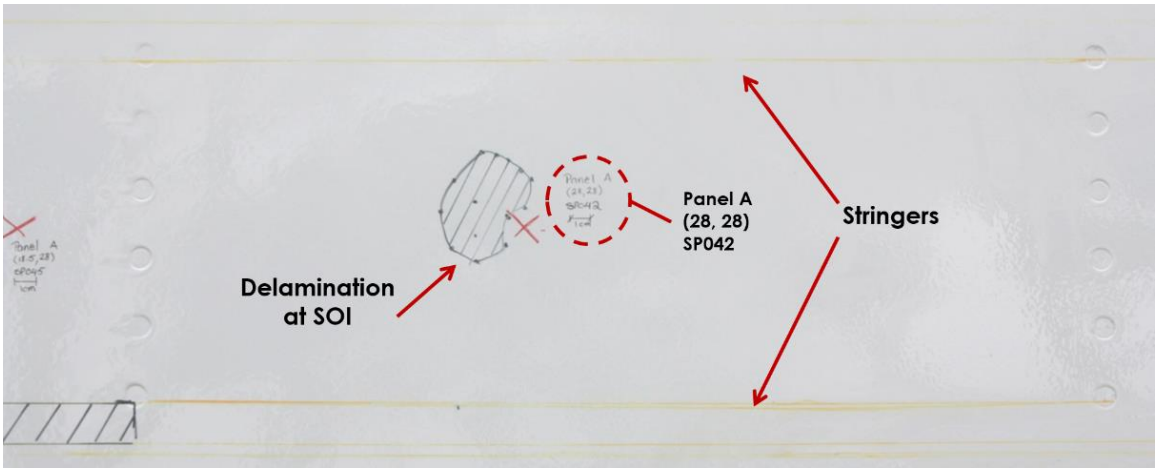

Figure 18. Type I Pristine Impact – Damage Mode I. Test No. SPO42; Single Hit at 295.4 J.

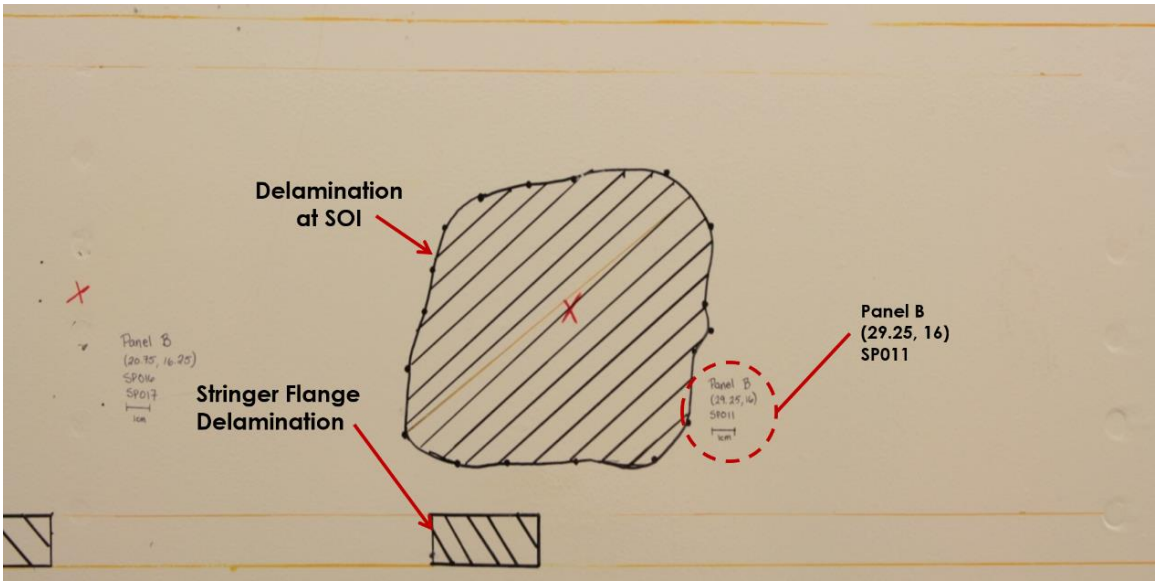

Figure 19. Type I Pristine Impact. Damage Mode III. Test No. SPO11; Single Hit at 745.6 J.

Figure 20 shows the corners of a bay delaminated after being impacted multiple times at increasing energy levels. Another damage mode observed at a site impacted multiple times is delamination at the SOI, in addition to extensive delamination at the corners of the bay (see Figure 21).

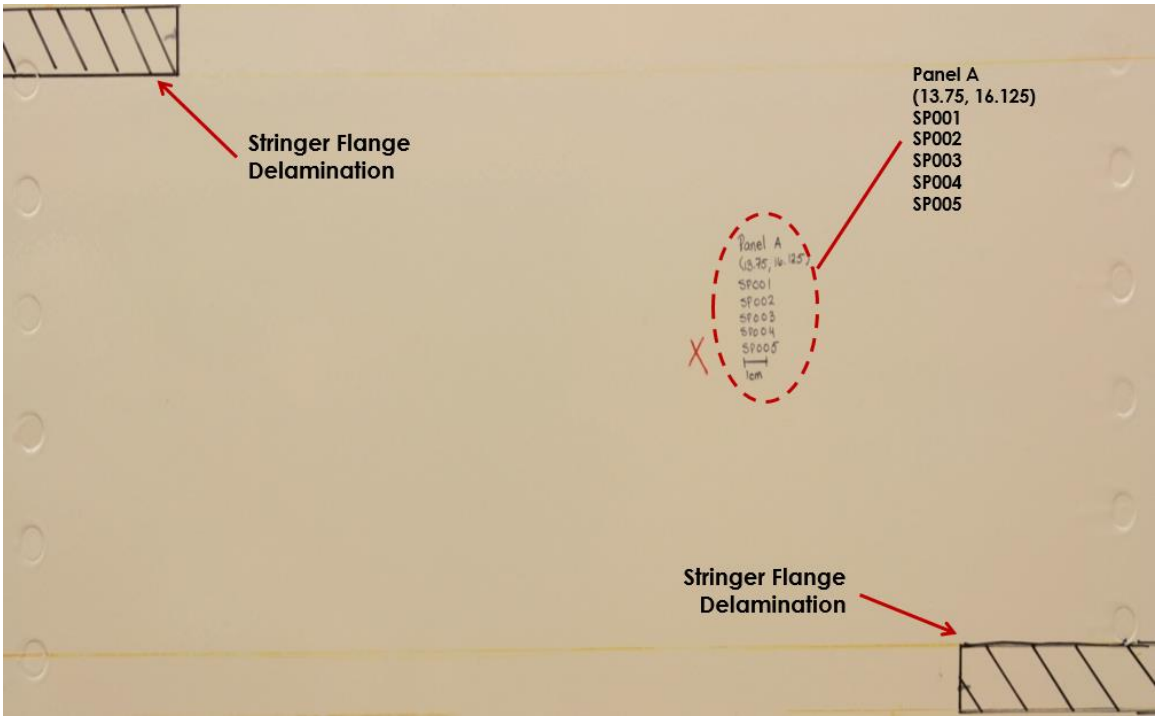

Figure 20. Impact at Previously Impacted Location: Damage Mode 1-Delamination in Corners of Each Bay; Multiple Impacts at 104.9 J (76.5 m/s), 107.3 J (89.6 m/s), 109.1 J (91.1 m/s), 108.0 J (100.6 m/s).

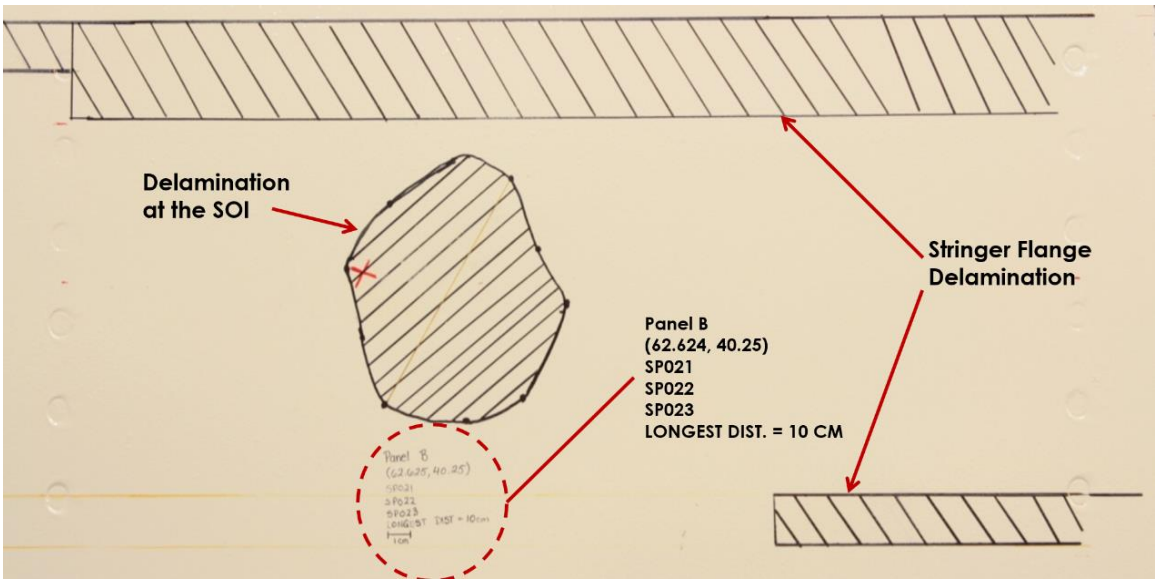

Figure 21. Impact at Previously Impacted Location: Damage Mode 2 - Delamination at SOI and In Peripheral Flanges; Multiple Impacts at 106.7 J (91.3 m/s), 105.8 J (101.0 m/s), 108.1 J (102.0 m/s).

Table 5 describes the general sequence of damage modes for Type I as impact energy levels increased beyond the FTE for pristine impact locations and previously impacted locations.

Table 5. Damage Mode Progression for Middle of the Bay Impacts (Type I)

Mode	Description
Impacts at a pristine location	
1	Small delamination at the SOI
2	Delamination at the SOI; Delamination in the stringer flange closest to the SOI
3	Extensive delamination at the SOI; Small delamination in the stringer flanges
Impacts at a location previously impacted	
1	Small delamination in stringer flanges at the peripheral boundaries of the bay
2	Delamination at the SOI; Delamination in the stringer flange closest to the SOI
3	Extensive delamination at the SOI; Delamination in stringer flanges at peripheral boundaries

3.4.2. Discussion

The first series of tests at mid-bay were in search of damage at the SOI. A preliminary FTE of 493 J was obtained, corresponding a 1.0 scaling factor, which is within 10% of the baseline FTE. After finding an FTE for damage at the SOI, further testing was carried out to find the onset of delamination between the stringer flanges and the skin. During these experiments, tests SP042 and SP044 behaved anomalously. These tests applied impacts at only 46% of the preliminary FTE, but resulted in (small) delaminations at the SOI and delamination of the stringer flanges. Thus, to be conservative and inclusive of the anomalous test results, a FTE range was identified instead of a FTE value. This range was determined to be 227 J to 567 J, giving a scaling factor rage of 0.46 to 1.16, with the lower associated with delamination occurring away from the SOI at the stringer-skin interface.

By nulling the anomalous test data points, the binary logistical regression resulted in an FTE value of 549 J (see Figure 22). This FTE value corresponds to a 1.2

scaling factor for damage at the SOI. With the length of the mid-bay (457 mm) being 50% greater than the length of the monolithic panels of the baseline FTE (305 mm), it was hypothesized that a greater energy level was required to initiate damage at the SOI, due to the skin's ability to deflect and dissipate energy prior to initiating damage; thus, the 20% higher FTE level for SOI delamination.

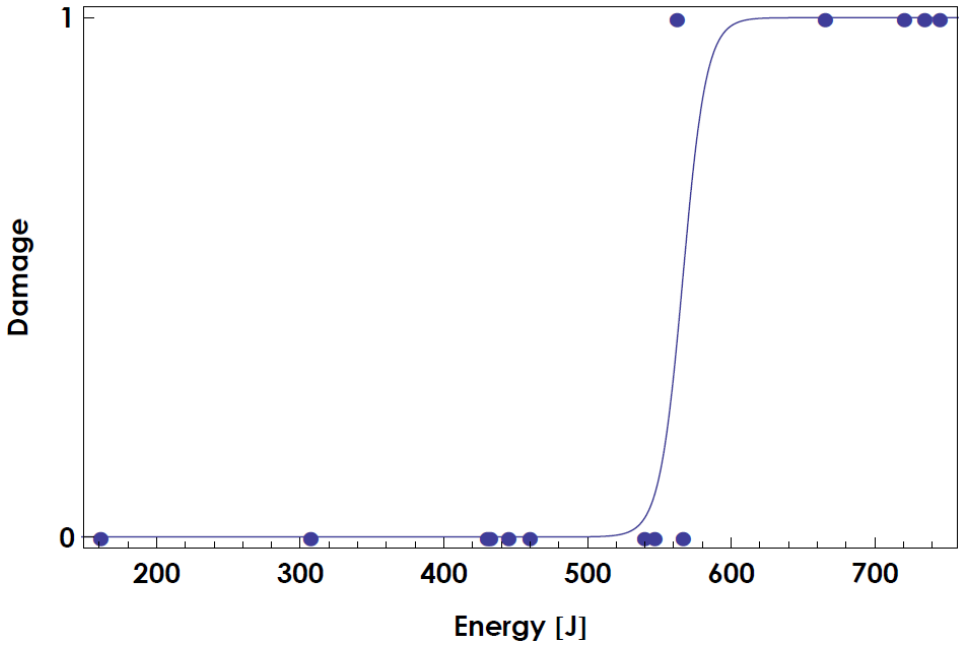

Figure 22. Type I Binomial Logistical Regression Fit with SP042 and SP044 Points Omitted: FTE of 549 J, Scaling Factor = 1.12.

Consistent with Rhymer et al.'s work [19], high variances were found when plotting total damage area of Type I versus impact energy (See Figure 17); thus, it can be determined there is not a strong correlation between impact energy and delamination area. Interestingly, energies greater than 556 J have less variance. This may indicate a correlation between delamination area and energy beyond the 556 J level.

The damage progression of Type I was observed to behave differently depending on whether or not the SOI had previously been subjected to impacts. Multiple impacts in the same area led to extensive delamination at the SOI and also extensive delamination in the stringer flanges. Once a small matrix crack or delamination is initiated by an impact, it acts as a flaw from which more extensive delamination can grow. Any impact following will therefore increase the level of delamination in the region of impact. Therefore the total delamination area at locations that were impacted multiple times are greater than those at pristine sites (See Figure 20).

Unlike the previously impacted locations, pristine impacts do not suffer effects of pre-existing impact damage. The first damage mode was identified as small delamination at the SOI, when impacted with energy levels within the FTE range (see Figure 18). As the energy level increased, the impact energy was dissipated through larger delamination at SOI, which extended towards the nearest stringer flange (mode 2). As depicted in Figure 19, energy levels much greater than FTE cause delamination in the stringer flange nearest to the SOI in addition to the delamination as described in mode 2. Thus, when the impact energy is sufficiently high, local delamination at the SOI will preferentially occur first before the wave energy reaches the bay's boundaries formed by the stringer flanges.

3.5 STRINGER FLANGE IMPACTS (TYPE II)

3.5.1. Experimental Results

SHI impacts to the stringer flange caused varying lengths of delamination between the stringer flange and the skin, leading to almost complete stringer flange unzipping, and occasionally backside fiber breakage in the flange. Stringer flange unzipping was defined as visually detectable backside disbond or delamination of the stringer flange and skin joint. Two specific impact locations were considered, IIa and IIb, at the end of the flange and middle, respectively (see Figure 14).

The stringers had non-uniform geometry where they contacted with the skin. Specifically, the flanges maintained a uniform thickness for the first 19 mm (0.75 in) of their width and tapered for the remaining 19 mm (0.75 in) (see Figure 8). Due to difficulty identifying delamination within the tapered region, only delamination detected by the A-scan within the uniform thickness region was included in delamination area calculations. Although regions where unzipping extended into the tapered portion of the flange were mapped, only delamination within the uniform thickness was included for the area measurements. The maximum extent of stringer flange delamination was the length of the bay (length between two shear ties). Thus, any delamination area greater than 8625 mm^2 indicated delamination along the entire length of the bay. Delamination due to Type II impacts was measured in three manners: (1) delamination area at the SOI (in contact with SOI), (2) further delamination area away from the SOI, and (3) total delamination area. The delaminated areas of Type II have been summarize

in Table 6. The data are first ordered by impact type and second then increasing energy.

Table 6. Stringer Flange Impact (Type II) Delamination Area Summary

Test No.-Panel	Impact Type	SHI Mass [g]	Velocity [m/s]	Impact Energy [J]	Delam. Area at SOI [mm²]	Further Delam. [mm²]	Total Delam. [mm²]	Percentage Delam. Along Length of Bay
SP020-B	IIa	107.9	56.5	172.3	0	5400	5400	63%
SP029-B	IIa	107.1	88.9	423.3	4200	0	4200	49%
SP033-A	IIb	103.2	56.3	163.4	0	0	0	0%
SP034-A	IIb	104.7	58.8	181.2	0	0	0	0%
SP019-B	IIb	107.7	61.1	201.3	5100	0	5100	59%
SP035-A	IIb	104.4	65.9	226.4	0	0	0	0%
SP037-A	IIb	102.4	68.6	241.1	0	0	0	0%
SP038-A	IIb	107.4	70.2	264.7	6400	0	6400	74%
SP036-A	IIb	106.1	72.1	275.9	4000	0	4000	46%
SP007-A	IIb	106.8	72.1	277.1	0	2500	2500	29%
SP013-B	IIb	108.2	71.8	279.1	8400	0	8400	97%
SP012-B	IIb	105.5	73.4	284.5	2600	0	2600	30%
SP028*-B	IIb	102.2	86.6	383.4	7900	0	7900	92%
SP030-B	IIb	103.2	88.9	407.9	2700	0	2700	31%
SP006-A	IIb	104.8	89.6	420.7	6400	0	6400	74%

*Denotes ice crushed prior to impacting target

Binomial logistic regression (shown in Figure 23) was applied to Type IIb, data from Table 6 to identify a FTE value. Any amount of delamination was assigned a value of one (1), regardless of the delamination's location. The FTE was found to be 183 J, resulting in a 0.37 scaling factor. Due to the lack of data, impact at the end of the flange (Type IIa) was only analyzed subjectively. A range of 49 to 147 J (0.10 to 0.30 scaling factor) was established as the FTE range of Type IIa.

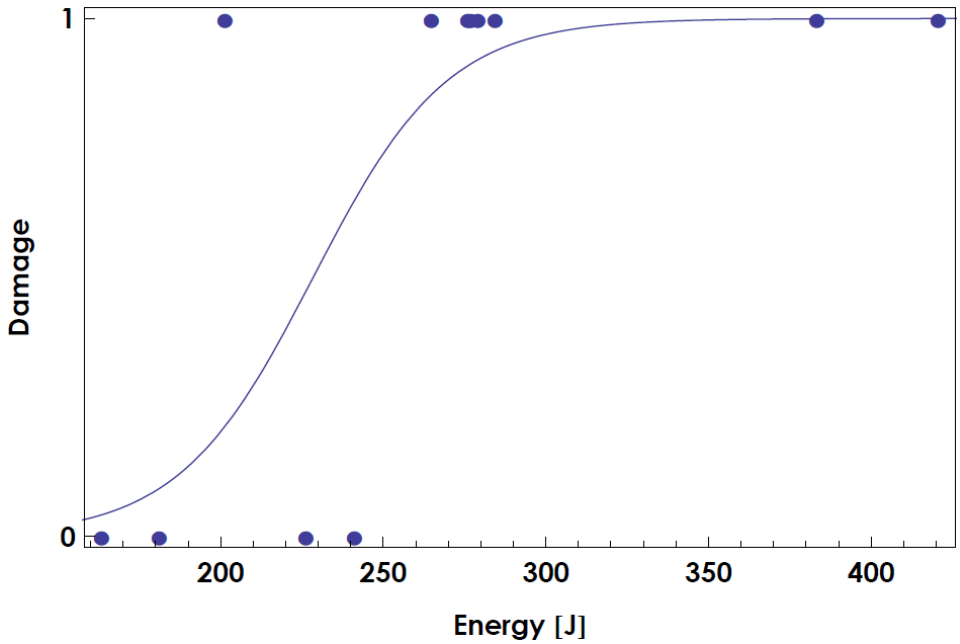

Figure 23. Type IIb: Binomial Logistical Regression Fit: FTE = 183 J; Scaling Factor = 0.37.

Impacts below the established FTE range for impacts at the end of the flange (Type IIa) were not observed. At 172 J, an impact energy greater than the FTE range, test SP020 caused the flange to create an open lip at the backside that was detectable by touch and delamination in the flange in areas adjacent to the SOI (see Figure 24 andFigure 25). Delamination of the flange at the SOI that was tactile-detectable from the backside, as well as delamination of the flange extending beyond the SOI, were produced by an energy nearly four times the FTE range (see Figure 26). These damage modes which initiated for Type IIa impacts are listed in Table 7.

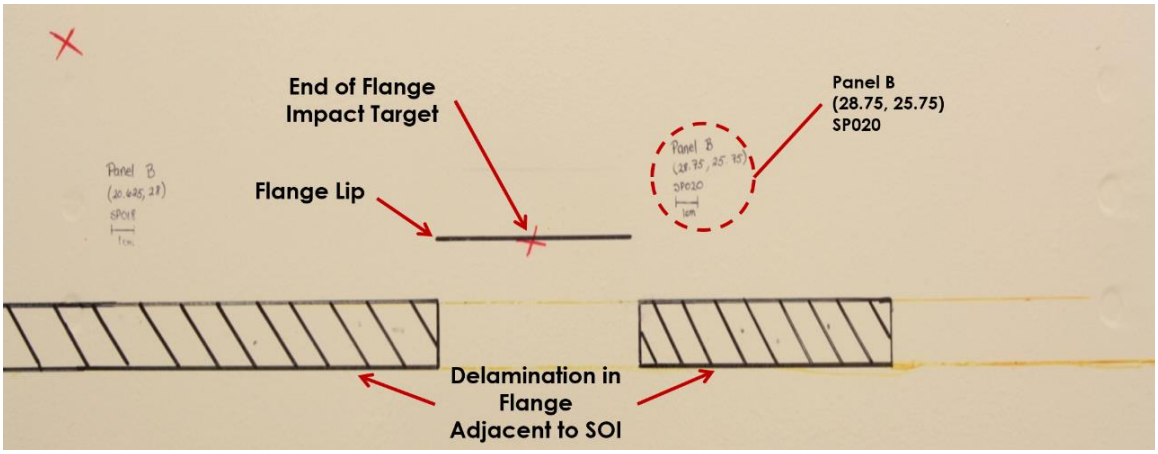

Figure 24. Delamination Adjacent to the SOI Caused by 172.3 J (56.5 m/s) Impact (Type IIa).

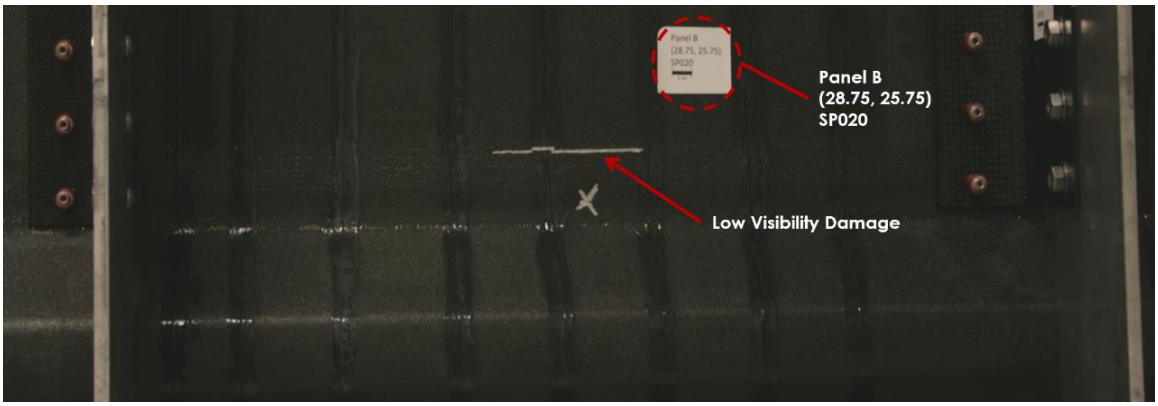

Figure 25. Tactiley Detectable Damage Due to 172.3 J (56.5 m/s) Impact (Type IIa).

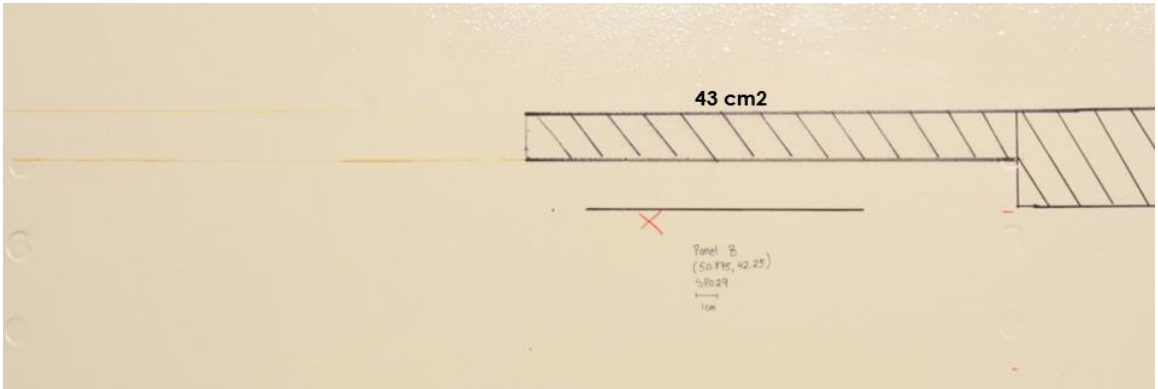

Figure 26. Front Side Damage Caused by 423.3 J (88.9 m/s) Impact at End of Flange - Type IIb.

Table 7. Damage Mode Progression for End of Stringer Flange Impacts (Type IIa)

Mode	Description
1	Tactile flange lip at the SOI; Flange delamination in adjacent areas to the SOI
2	Tactile flange lip at the SOI; Flange delamination at the SOI and extending further

For Type IIb, impacts at energy levels less than FTE did not cause delamination in the stringer flange. In several cases, such as SP035 (refer to Appendix D for photographs), one ply within the tapered region of the flange lifted and was barely sensible by touch (at the panel backside surface), but did not cause detectable delamination. Energy levels near the 183 J FTE caused delamination extending away from the SOI. With impact energy increased to about 50% greater than the established FTE, two damage modes were observed. One mode resulted in delamination in the flange extending nearly the entire length of the bay (Figure 27). The other mode produced backside fiber breakage of the flange in addition to the flange unzipping approximately 60% of the span (see Figure 28). See Table 6 for percentage of delamination along the length of the bay. The damage modes for Type IIb, impacts at the middle of the stringer flange, have been summarized in Table 8.

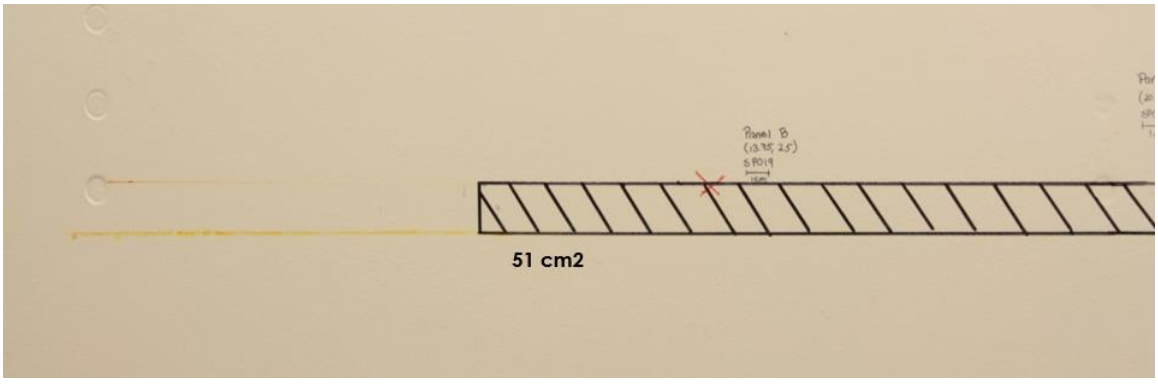

Figure 27. Front Side of 201.3 J (61.1 m/s) Middle of Flange Impact (Type IIb).

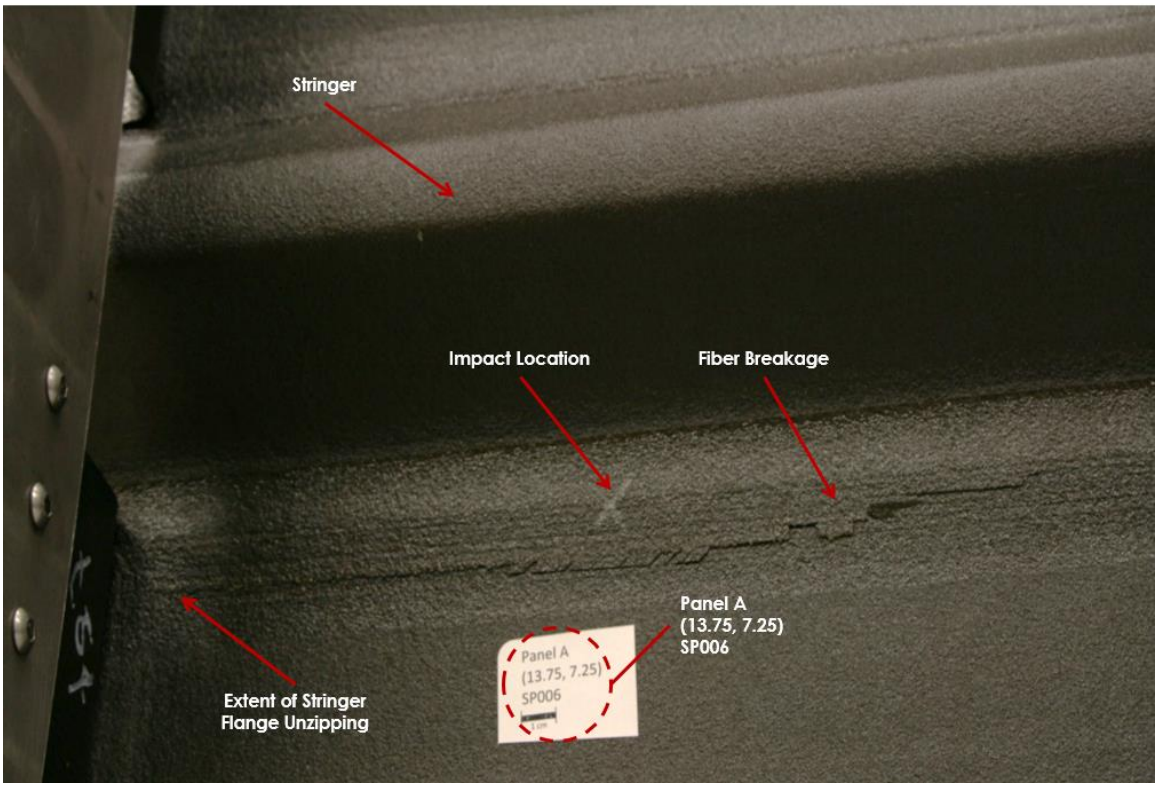

Figure 28. Back Side Damage Caused by 420.7 J (89.6 m/s) Middle of the Flange Impact (Type IIb).

Table 8. Damage Mode Progression for Middle of Stringer Flange Impacts (Type IIb)

Mode	Description
1	No delamination; Barely tactile flange
2	Small delamination away from the SOI
3	Delamination at the SOI and further out
4	Extensive delamination at the SOI; Unzipping delamination of flanges towards ends
5	Extensive delamination at the SOI; Unzipping delamination of flanges towards ends along with backside fiber breakage

3.5.2. Discussion

During testing, low energy level impacts were observed to cause matrix cracking, which were barely detectable via tactile observation. Although this is a mode of damage, it was not used to identify the FTE. FTE parameters were defined by the initiation of delamination because delamination reduces the compressive

strength and stiffness of the panel. Furthermore, it was determined that damage used to identify FTE must be detectable via A-scan. Matrix cracking is not detectable using A-scan. Damage that was only detected visually and tactilely was notated, but not included in establishing the FTE.

The scaling factor of impact at the middle of the stringer flange was found to be 0.37 (183 J). At impact energies in close proximity to the FTE, delamination was found within the flange in the region surrounding SOI. Higher energy levels extended the length of delamination along the length of the flange. At impact energy levels much greater than the FTE, significant delamination and backside fiber breakage in a circular shape occurred in the tapered step lap layers near the SOI.

Backside fiber breakage can be attributed to the stringer flange bending to comply with the moments developed about the stringer width (see Figure 29) caused by transverse loading of the SHI. Because the flange was constrained by the geometry of the stringer, it developed high tensile stress and caused backside fiber breakage in the flange. This breakage led to delamination between the stepped layers along most of the flange (See Figure 28). Due to the need to keep this specimen intact for further non-destructive evaluation studies, it was not possible to further investigate (via sectioning) the exact location of the delaminations in the flange to identify whether the delamination was at the interface between the skin and stringer flange, or within one of the laminates.

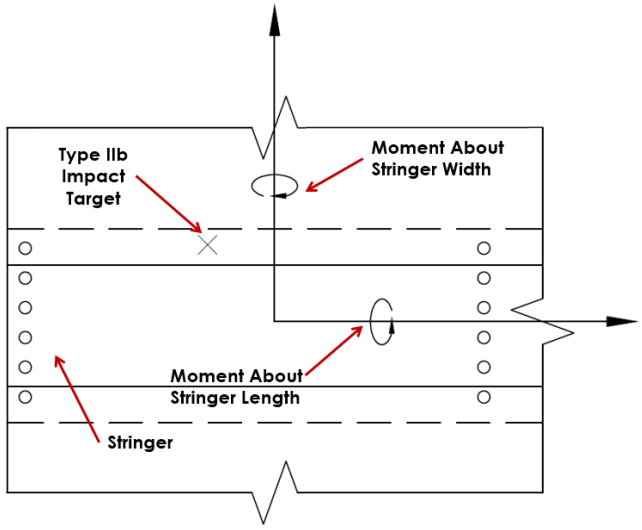

Figure 29. Moments Developed Relative to Stringer in Response to SHI Impact.

The tapered geometry of the flange allows for gradual load transfer between the adherends. Impacts at the middle of the flange (Type IIb) allowed for the load to distribute among all step laps (See Figure 30 [32]). Thus, it is not surprising that impacts at the end of the stringer flange (Type IIa) initiated delamination at much lower energy levels comparatively. Delamination was initiated at levels as low as 172.3 J. With impacts directed at the last steps of the tapered flange, shear stresses were unable to distribute among all lap steps.

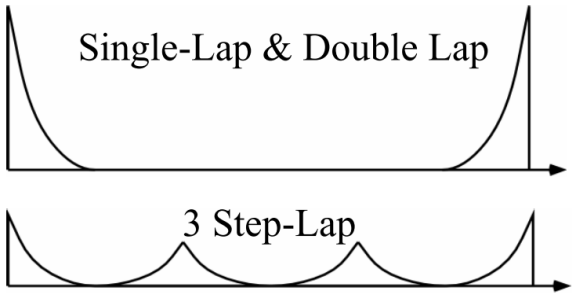

Figure 30. Shear Stress Profiles of Single-Lap and Double Lap Joints in Comparison to 3 Step-Lap Joint [32].

In addition, transverse loading of the SHI develops peel stresses between the individual step layers of the tapered flange. Similar to shear stresses, peel stress peaks at the end of each lap, which are the ends of the bondline (See Figure 31 [23]). Type IIa initiated high peel and shear stresses directly in the last step laps of the tapered flange. Thus, the scaling factor of impacts at the end of the flange (Type IIa) was qualitatively approximated to be in the range of 0.10 and 0.30. This corresponds to a FTE range of 49 to 147 J.

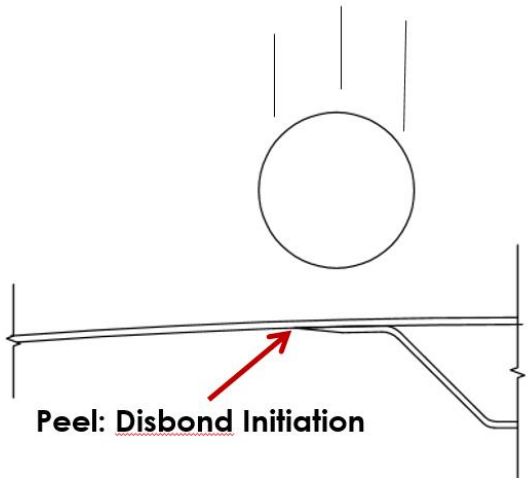

Figure 31. Backside Global Debond Initiated by Impact-Induced Peel Stress.

The 172 J Type IIa impact was significantly greater than the FTE range established. It resulted in the layer closest to the skin of the flange to raise, creating a lip along with delamination that extended 63% of the bay length. Interestingly, delamination did not occur in the flange region directly below SOI (See Figure 24 and Figure 25). The tactile lip can most likely be attributed to high peel stresses (i.e. tensile stresses normal to the skin) in the last several step laps of the flange in combination with high shear stresses between the laminas.

The damage modes identified in this study for stringer flange impacts (Type II) are consistent with those identified in [23] for transversely impacted glass-epoxy bonded lap joints, but differs in the order that they progress. Kim et al.'s [23] investigation established fiber failure to occur prior to localized and global debonding, whereas the current study denotes fiber failure to be the last mode of failure. This difference may be due to the fact that Kim et al.'s [23] study consisted of low velocity impacts (10-50 J impacts) with a hard metal impactor of 25.4 mm diameter, which does not share the crushing characteristics of projectile SHI. Thus, the ice produces a more large-area contact zone, which can suppress the formation of local failures induced by high contact stresses which develop under metal tip impacts.

3.6 MIDDLE OF STRINGER IMPACTS (TYPE III)

3.6.1. Experimental Results

Impacts at the middle of the stringer (i.e., mid-stringer Type III) initiated delamination at the SOI and delamination in the flange region of the stringer. Delamination was measured in three manners: (1) delamination area at the SOI (in skin), (2) stringer flange delamination area away from the SOI, and (3) total delamination area. Due to the close proximity of the test locations to each other and the A-scan malfunctioning between experimentation, the stringer flange delamination areas are an approximation. The approximate delamination areas are shown below in Figure 32. Table 9 summarizes the delamination areas for Type III.

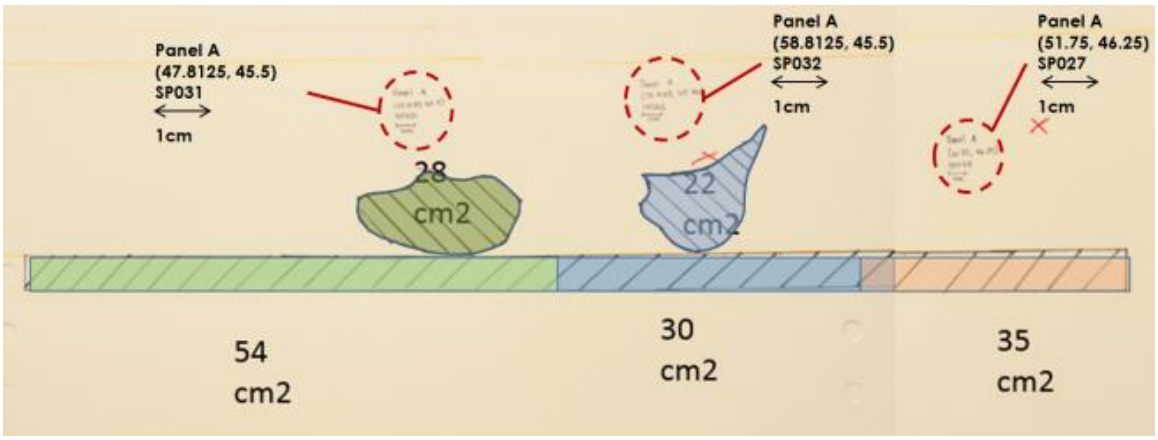

Figure 32. Delamination for Middle of Stringer (Type III).

Table 9. Middle of Stringer Impacts (Type III) Delamination Area Summary

Test No. - Panel	Velocity [m/s]	SHI Mass [g]	Impact Energy [J]	Delamination Area at SOI [mm²]	Further Delamination [mm²]	Total Delamination [mm²]
SP039-A	72.4	105.5	276.5	0	0	0
SP040-A	79.8	104.2	331.7	0	0	0
SP041-A	86.6	103.5	388.3	0	12800	12800
SP031-A	87.4	103.4	394.8	2800	3000*	5800*
SP027-A	91.0	106.8	442.3	0	3500*	3500*
SP032-A	102.0	107.8	560.8	2200	5400*	7600*

*Indicates an approximate value

Binomial logistic regression was used to find the FTE of mid-stringer impacts (Type III) using the data presented in Table 9. The FTE was established to be 357 J, resulting in a scaling factor of 0.73 (see Figure 33). In addition, data from Table 9 were also used to plot delamination area versus impact energy, which is shown in Figure 34.

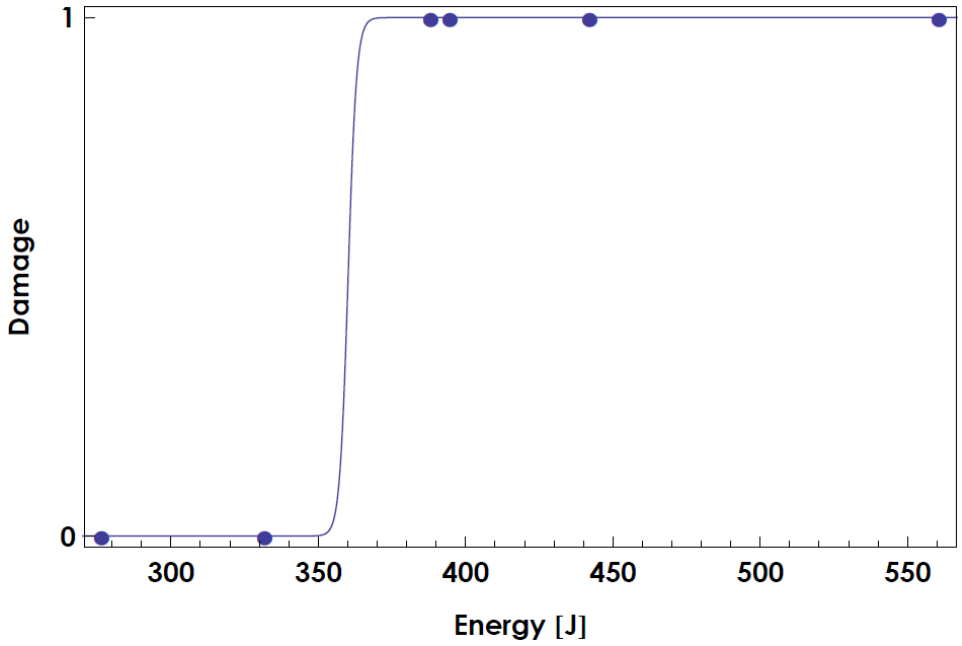

Figure 33. Type III Binomial Logistic Regression Fit: FTE= 357 J, Scaling Factor = 0.73.

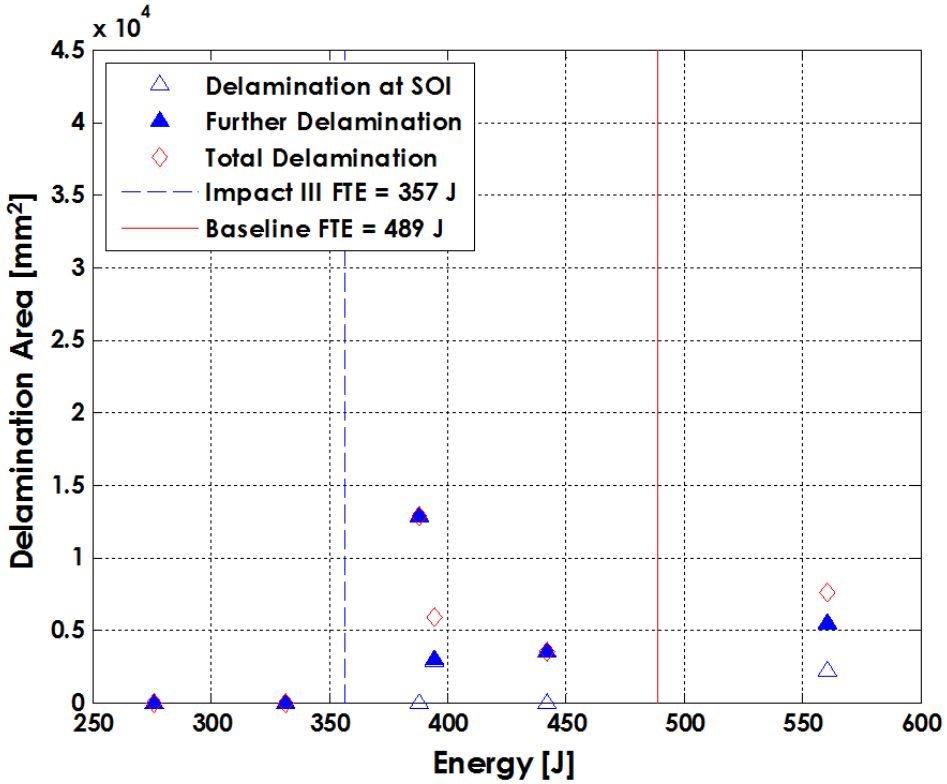

Figure 34. Middle of Stringer Impacts (Type III): Delamination Area Versus Impact Energy Plot.

Delamination was not detected for impacts below the 357 J FTE established by the binomial regression analysis. The first damage mode was identified from test SP041 (388.3 J) with delamination in the flanges directly adjacent to the SOI. On the backside, it was visibly detectable that the flanges had delaminated (see Figure 35). Higher impact levels produced delamination at the SOI and in the flange, as well as unzipping of the flange as depicted in Figure 36. These damage modes have been summarized in Table 10.

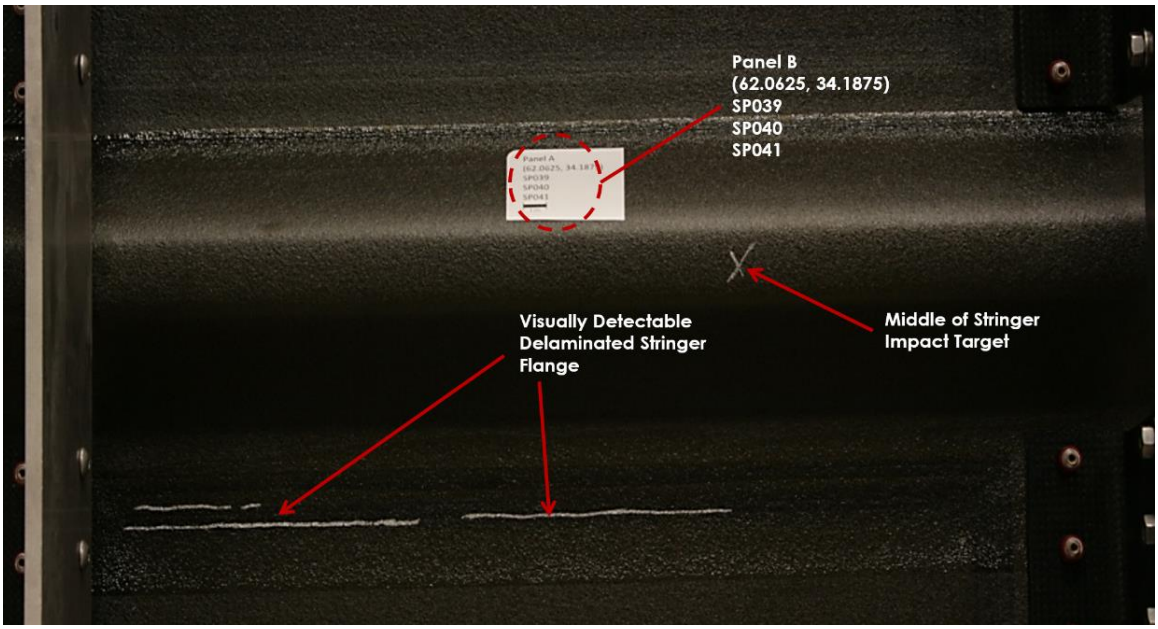

Figure 35. Visually Detectable Delamination Caused by Type III at an Impact Energy Close to the Established FTE Value.

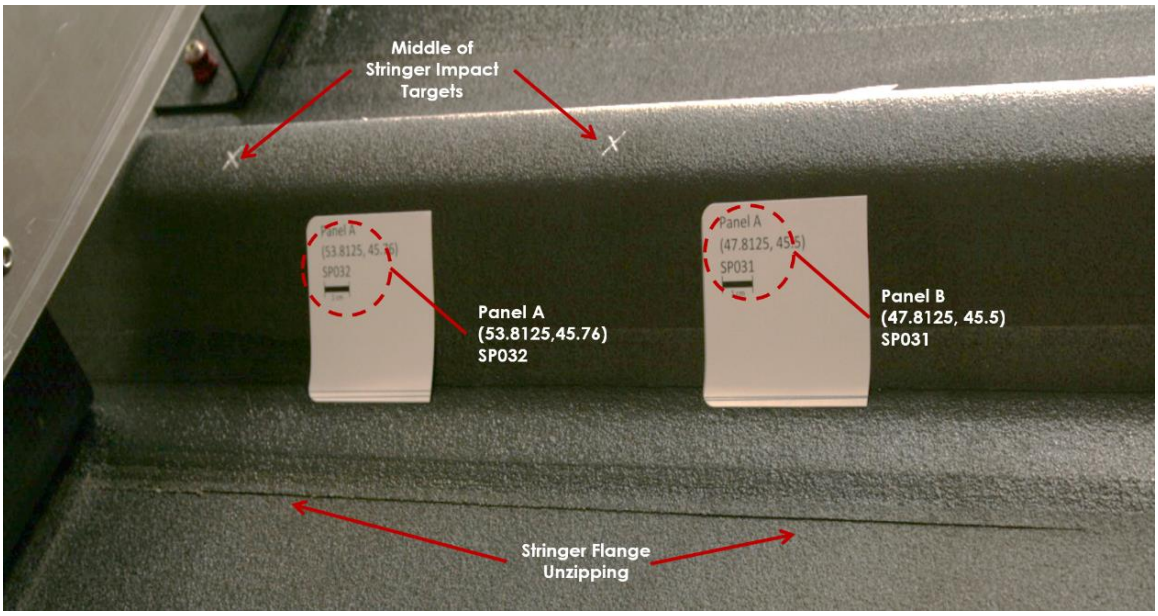

Figure 36. Unzipping of the Flange Due to Impacts Greater than the Established FTE Value (Type III).

Table 10. Damage Mode Progression for Middle of Stringer Impacts (Type III)

Mode	Description
1	No delamination at SOI; Delamination in the flanges directly adjacent to the SOI; Flange lip directly above or below the SOI
2	Delamination at the SOI; Delamination in the flanges directly adjacent to the SOI; Unzipping of the flange

3.6.2. Discussion

Due to A-scan system malfunctionings, delamination detection was not performed between tests SP027, SP031, and SP032. These tests resulted in delamination, which determined FTE was less than 395 J. Tests SP039 through SP041 were performed starting with a much lower projectile energy and incrementally increased the energy to determine the FTE value. The FTE of 357 J for impacts over the middle of the stringer was characterized by the disbonding between the stringer stiffener and the skin.

From the experimental results, the first mode of damage initiated by impacts at the middle of the stringer was established to be delamination in the flanges. This was due to the combination of tensile peel stresses and shear stresses developed at the skin-flange interface, as the skin bends out-of-plane from the projectile impact, as depicted in Figure 37. At energy levels greater than FTE, impacts caused delamination at SOI and flange unzipping. The delamination of the flanges were visually and tactilely detectable from the backside. Without insight from experimentally-measured data such as force time history or finite element analysis (FEA), it cannot be determined whether delamination at the SOI occurred at the same time, before, or after the flange delaminated. It can be hypothesized that as the stringer disbonded from the skin, the skin at the middle of the flanges behaved similarly to a short-span monolithic panel (see Figure 37). Thus, delamination at the SOI possibly occurred after delamination at the flange region.

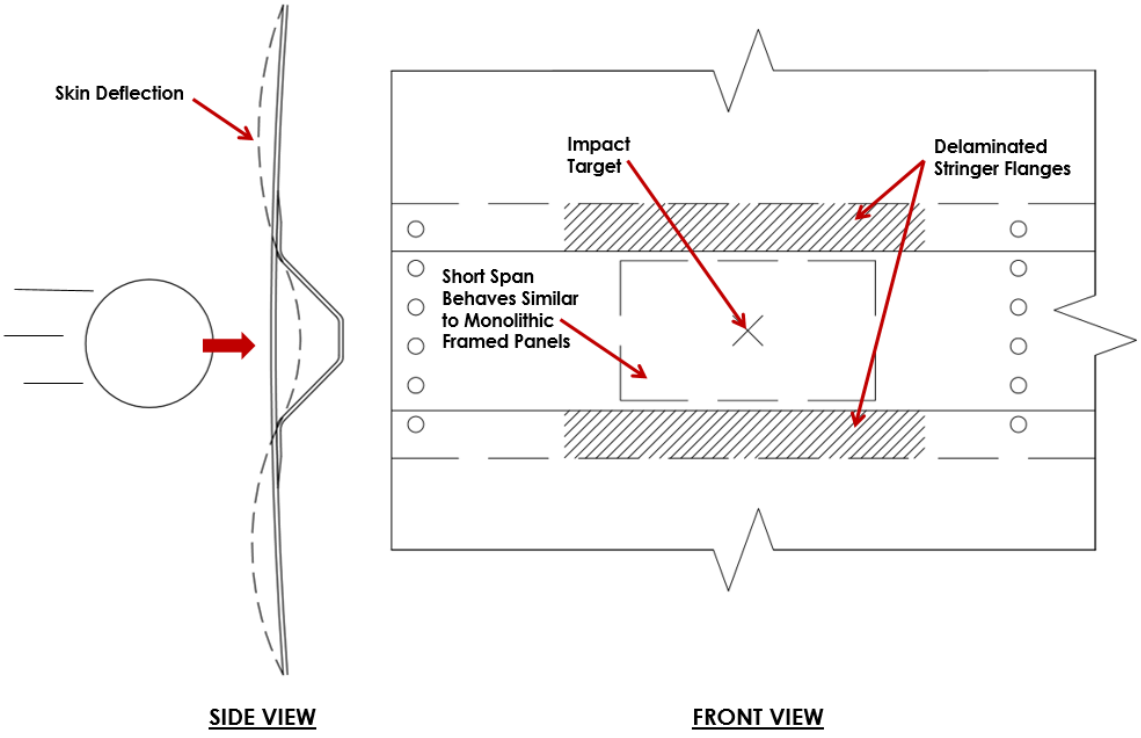

Figure 37. Type III Panel Response to SHI Impact.

3.7 SHEAR TIE IMPACTS (TYPE IV)

3.7.1. Experimental Results

Impacts directly over the shear tie caused the white aerospace grade paint to chip on the impact side, delamination in the shim and along stringer flanges, and backside fiber breakage at the curved section of the shear tie. Due to the complexity of the area where shear ties attach to shims, stringers, and skin, delaminations caused by impacts at the shear tie were difficult to assess via A-scan. Therefore, delamination areas were not mapped on the panel. In place of delamination area mapping, notes of visually and tactilely detectable damage

were recorded. The damage modes observed for Type IV are listed with their corresponding test numbers, and impact velocities and energies in Table 11.

Table 11. Impact Over the Shear Tie (Type IV) Detected Damage Summary

Test No.	SHI Mass [g]	Velocity [m/s]	Impact Energy [J]	Visual and Tactile Detection Notes
SP014-B	108.3	84.2	384.0	No damage
SP016-B	106.2	94.7	476.5	Paint chipped on front side; No damage detected
SP018*-B	108.0	111.4	669.6	Small shim delamination; Small fiber breakage along curved section of shear tie
SP015-B	107.2	116.5	728.0	Delamination along length of shim; Delamination in stringer extending into shear tie; Fiber breakage along length of shear tie curved section
SP017-B	107.1	117.4	738.1	Delamination along length of shim; Fiber breakage along length of shear tie curved section

*Denotes ice crushed prior to impacting target

A binomial logistic regression was applied to the data from Table 11, and established an FTE of 563 J for Type IV (see Figure 38). Per the visually and tactilely detectable damage notes, any damage was assigned the value of one (1). This resulted in a 1.15 scaling factor.

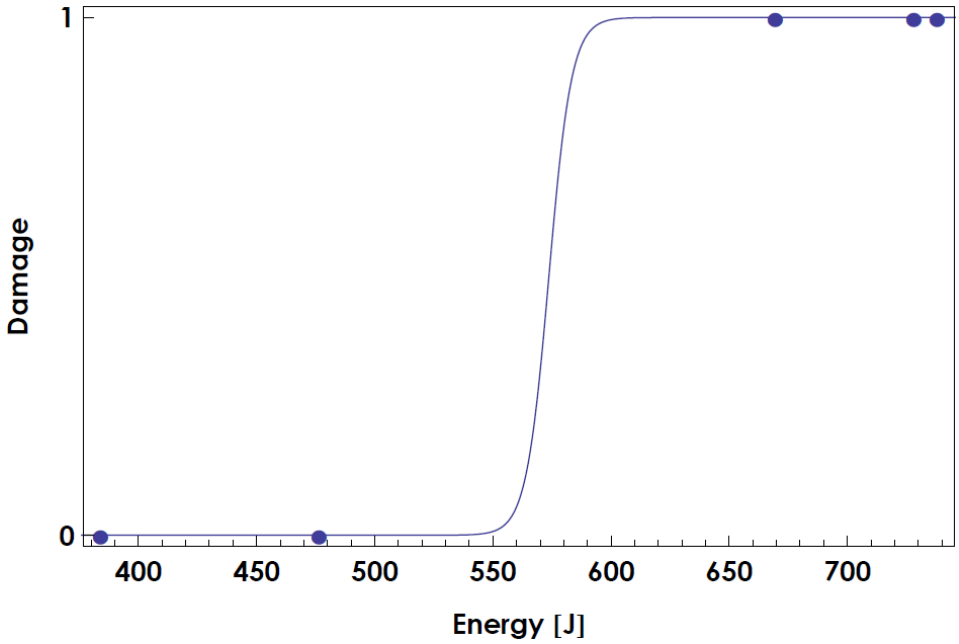

Figure 38. Type IV Binomial Logistical Regression Fit: FTE =563 J, Scaling Factor = 1.15.

Impacts at energies 476.5 J and less caused the aerospace paint to chip over countersunk rivets, but did not produce any detectable damage (see Figure 39). Figure 40 shows 50 to 60 mm of delamination of the shim and small fiber breakage in the curved section of the shear tie initiated by 669.6 J. As projectile impact energies increased from this value, delamination of the shim and fiber breakage in the curved section of the shear tie extended to the full length of the respective components (see Figure 41 and Figure 42). The damage modes observed are summarized in Table 12.

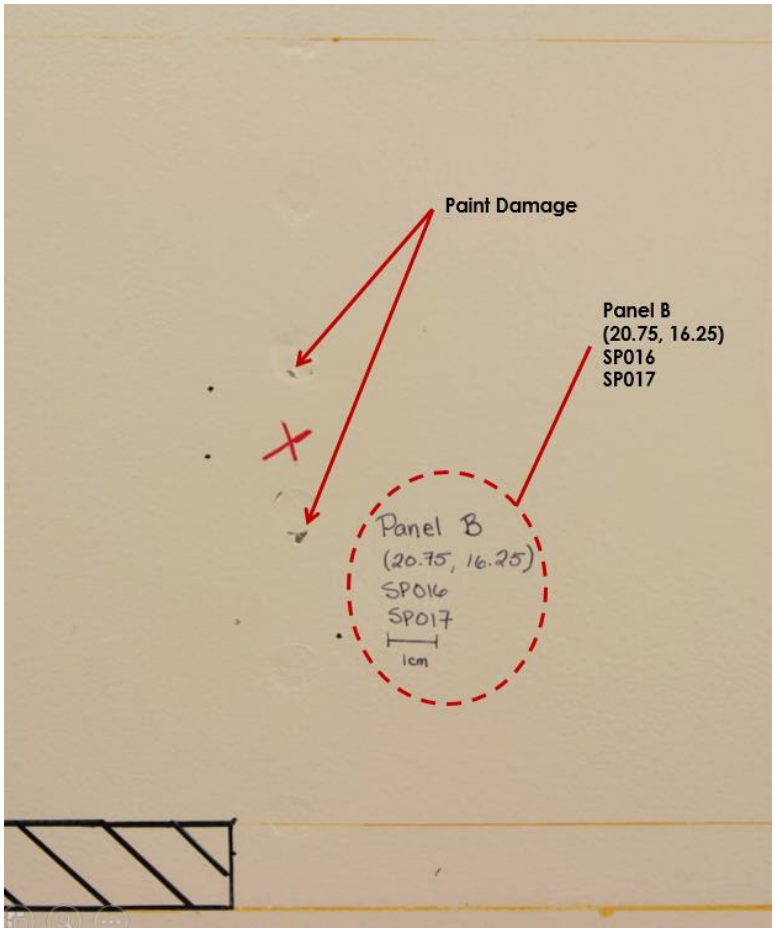

Figure 39. Visually Detectable Paint Damage Caused by 476.5 J (94.7 m/s) Impact.

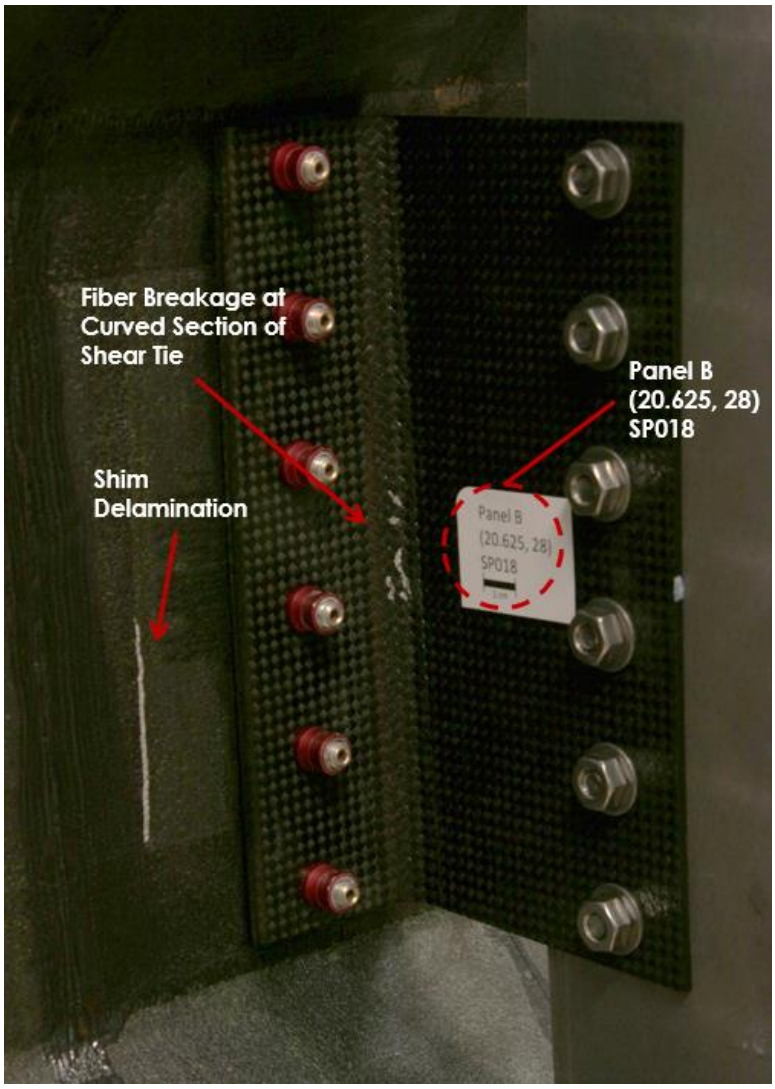

Figure 40. Minimal Backside Damage Due to 669.6 J (111.4 m/s) Impact.

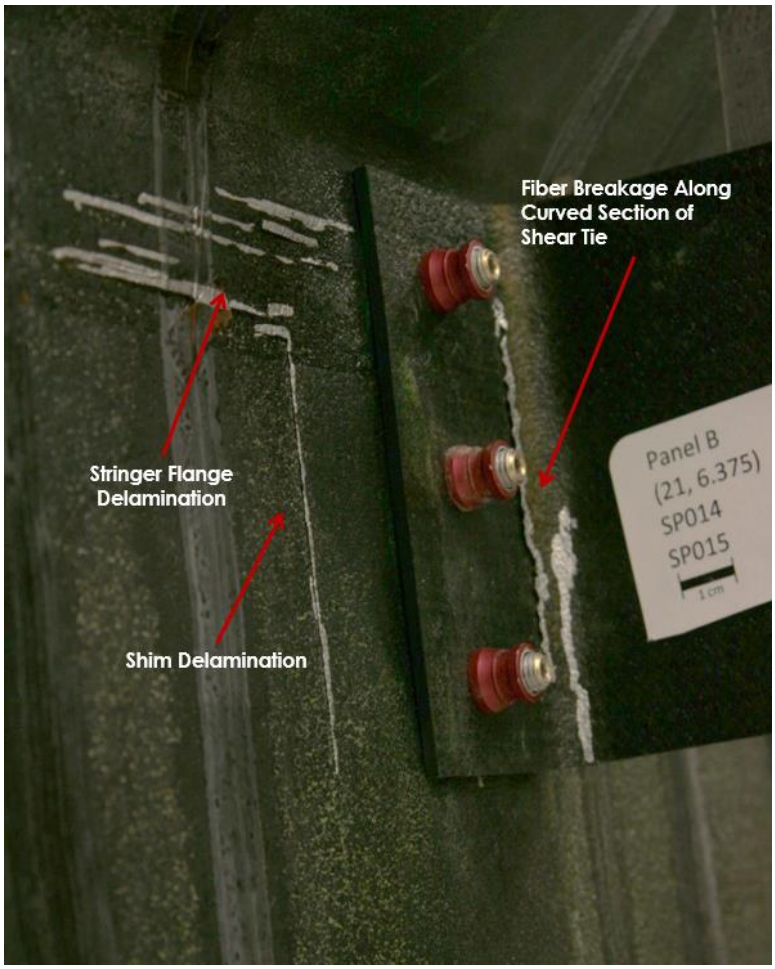

Figure 41. Tests SP014 and SP015 caused fiber breakage along corner of shear tie extending nearly the length of the shear tie as well as delamination of the shim and the stringer flange.

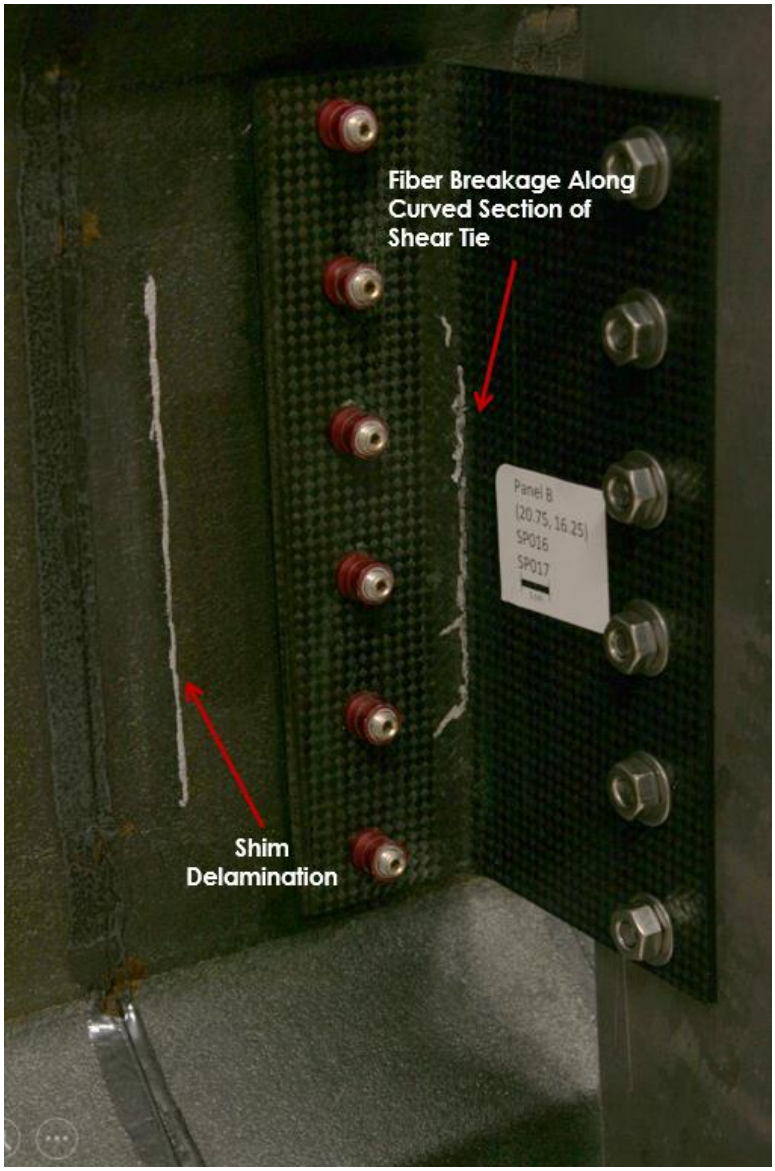

Figure 42. SP017 caused extensive fiber breakage in the corner of the shear tie and delamination of the shim, but did not cause delamination in the stringer flange.

Table 12. Damage Mode Progression of Over the Shear Tie Impacts (Type IV)

Mode	Description
1	No damage on shear tie or shim; Chipped paint over countersunk rivets
2	Minor tactile lip on shim; Fiber breakage in center curved section of shear tie
3	Tactile lip extending the length of shim; Tactile lip and delamination of stringer flange; Fiber breakage in curved section of shear tie extending two-thirds of shear tie

3.7.2. Discussion

With a direct load path and high bending stiffness discontinuity from the geometrical make-up of the skin, shim, and shear tie components, Type IV was expected to have a FTE in close range of the baseline FTE of 489 J. While the measured 563 J FTE was a bit higher than expected, the shim effectively doubled the thickness of the impacted skin (which would be associated with a higher baseline), and also the damage was not easy to detect. Because damage detection of Type IV was based on visual and tactile assessment, and delamination is often barely visible, any delamination of the affected components may have been over looked. As a result, the FTE of 563 J may be unconservative.

The chipped paint observed in Type IV impacts provided evidence of impacts occurring at this particular location, which may be helpful by indicating where impacts have occurred and need further assessment. It may also be misleading, however, since the presence of chipped paint does not directly imply structural damage.

As impact energies increased, the panel experienced more out-of-plane bending. While the skin deflected to comply to the curvature of the SHI, peel and shear stresses developed at the skin and shim interface, thus, causing the tactile lip and delaminations observed at the edge of the shim. The shear tie was also subjected to bending. Along the length, the shear tie behaved like a beam subject to a point load in response to the SHI impact. It displaced in the middle as shown in the side view of Figure 43. In the other direction, in order to comply with the SHI impact, the short leg of the shear tie bent inward. These responses caused

high flexural and shear stresses at the curved section of the shear tie, which resulted in local failure – fiber breakage. As impact energies increased, this damage became more extensive.

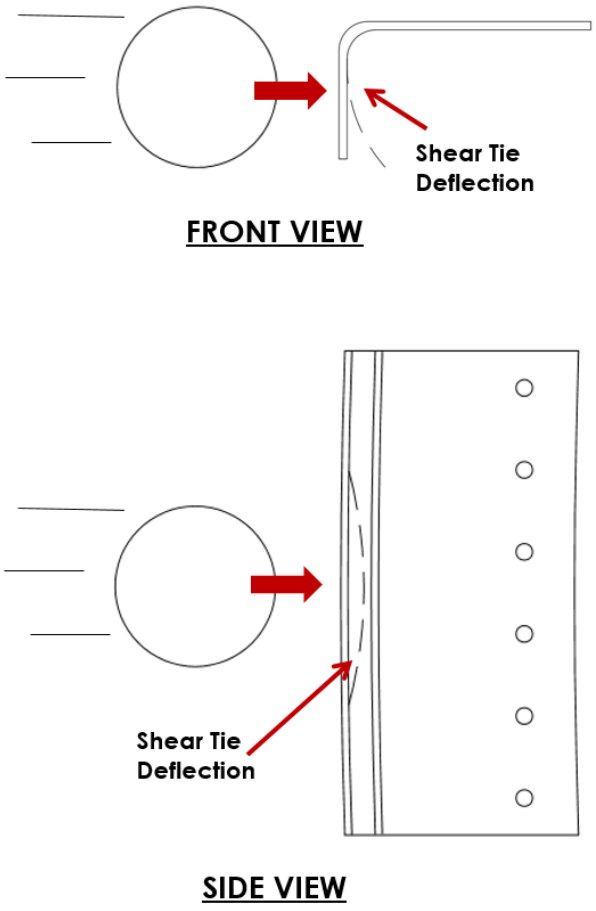

Figure 43. Shear Tie Deformation in Response to SHI Impact.

3.8 ALTERNATIVE NDE METHODS

Further impact damage and non-destructive investigation on the full-scale panels were performed by Stephen Neidigk of Sandia National Labs. He investigated the effectiveness of the various methods used for damage

assessment. Drop weight tool type impacts were applied to create additional damage in areas of the panel not impacted by SHI. Alternative methods included A-Scan, C-scan, and resonance testing, using an Omniscan Unit 5 MHZ and C-Scan using a Boeing MAUS V Pulse Echo Unit, to acquire accurate images of the impact damage.

Damaged detected using NDT Automation CBRZ5X2 A-scan was mapped on the panels using black ink. The resulting delaminated areas were presented in the previous sections of Chapter 3. Figure 44 shows additional delamination detected by the MAUS 5 pulse echo unit, marked in orange. The MAUS V pulse echo results found more delamination extending towards the nearest shear tie from test SP032, a middle of the stringer Type III impact. Although these findings would increase the delaminated area calculations presented previously, it would not significantly alter the FTEs identified nor the damage mode progressions identified for each impact type. The damage mode descriptions were inclusive of the additional delamination shown Figure 44.

Figure 44. Damage Mapping of Panel A using A-Scan. Black markings show damage detected using NDT Automation CBRZ5X2 SN:282 by UC San Diego. Additional damage detected using MAUS V pulse echo unit by Sandia National Labs is marked in orange. The red boxes emphasize areas impacted by SHI.

Figure 45 and Figure 46 present C-scans using resonance testing. In general, the delaminations shown in the C-Scans are in agreement with the areas mapped in Figure 44. The color variations give insight as to the depth range of the delamination. In some regions where delamination in the flange was not detected by NDT Automation CBRZ5X2, the C-scans show a very small area of delamination or only a slight color change. The slight color change signifies the signal was stronger at the specified location than at places with a drastic color change, implying those delaminations were less severe. The NDT Automation CBRZ5X2 A-Scan may not have detected the damage areas by the Omniscan

and the C-scan due to the small damage area and less severity. In addition, the A-Scans were reliant on the inspectors training and experience; lack of training and experience of the inspector using NDT Automation may also explain the difference in damage area assessment between the A-scans and C-scan results. It may have also been a result of the hand inspections being performed in close proximity to the impact site. For A-scan, the signal of a "good" reference area (i.e., not delaminated, flawless, etc.) is referenced in order to identify delamination. It is easiest to infer damage in an A-scan when there is a "good" area near the delaminated area, because it is easiest to identify while watching the signal transition as the transducer crosses from a "good" area over to a "bad" area. In order to detect the delaminated stringer flange (pointed out in Figure 45 andFigure 46), this manner, an inspector would need to inspect nearly 0.5 m (2 ft) away from the SOI to obtain a reference "good" signal.

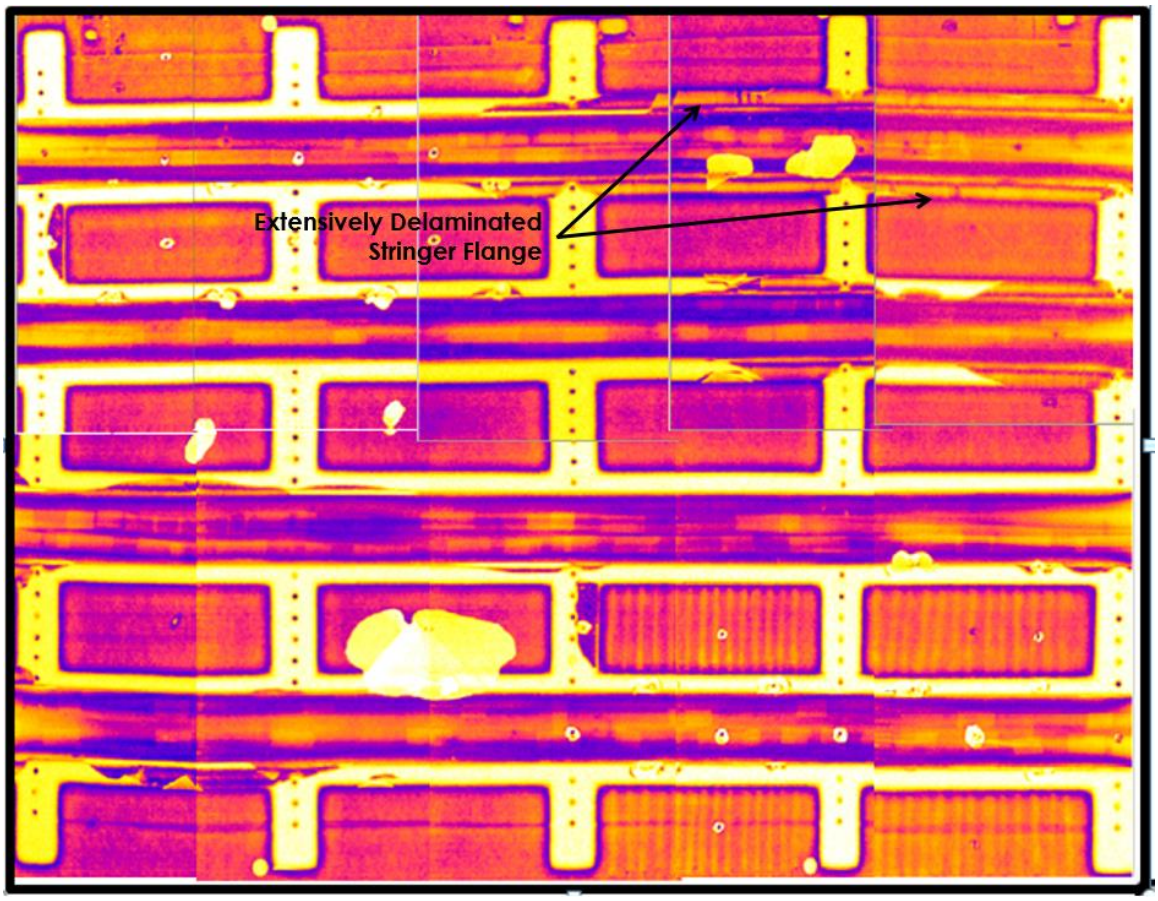

Figure 45. Resonance X-Plot Using Boeing MAUS V Pulse Echo Unit.

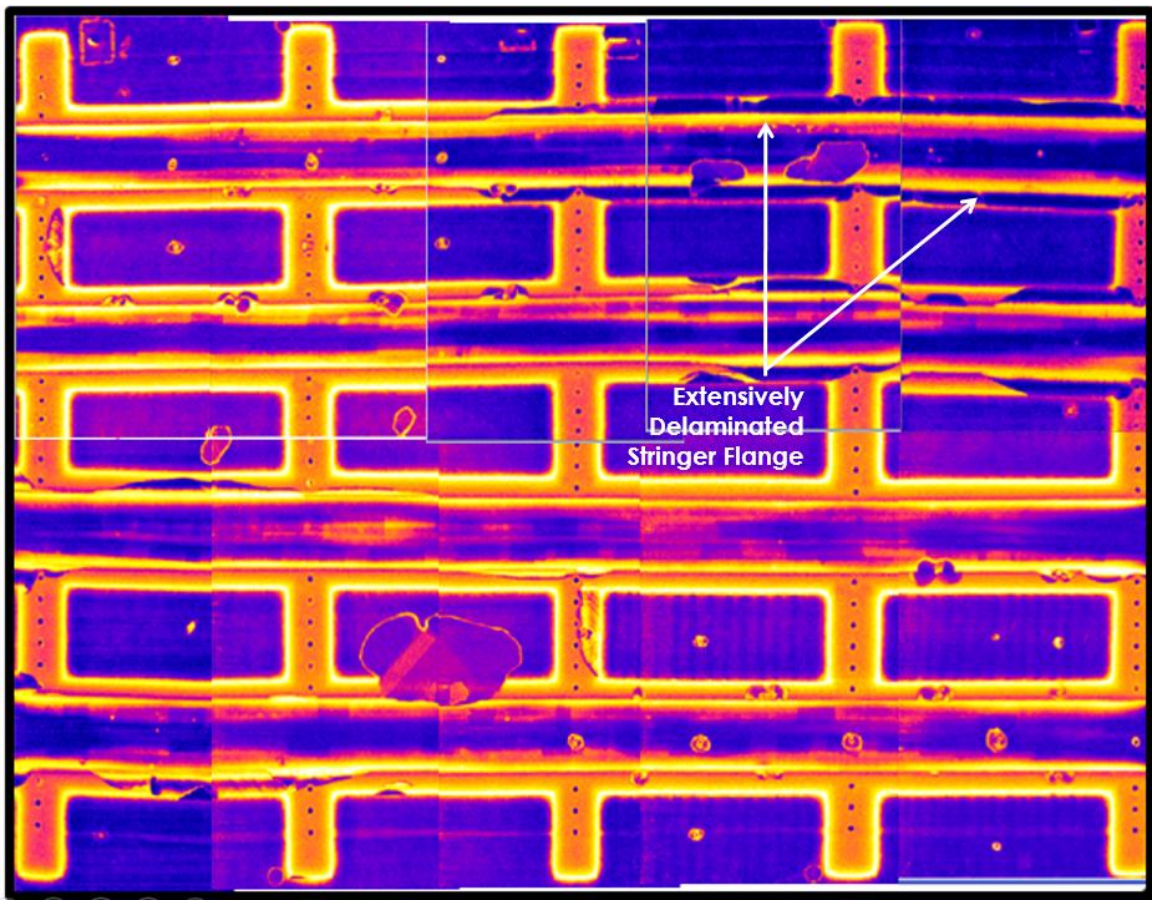

Figure 46. Resonance Y-Plot Using Boeing MAUS V Pulse Echo Unit.

4. DISCUSSION AND CONCLUSIONS

4.1 OVERALL DISCUSSION

Comparing the different impact locations, impacts at the stringer flange (Type II) were found to be the most critical and had the lowest resistance against transverse impact loads with scaling factors established to be as low as 0.09, as summarized in Table 13. The scaling factor associated with stringer flange edge (Type IIa) impacts drastically reduce the FTE relative to the baseline value of 489 J measured for impacts onto flat 305 x 305 mm panels supported in a picture frame fixture. Such impacts led to extensive damage such as delamination and unzipping of the stringer flange. Thus, stringer flange and skin joints are the most critical regions of an aircraft fuselage, and should be given detailed inspection to detect damage after a hail impact event.

Table 13. FTE and Scaling Factor Summary

Impact Location	FTE [J]	Scaling factor
I – Middle of bay	227 -567	0.46-1.16
IIa – End of stringer Flange	49– 147*	0.10-0.30*
IIb- Middle of stringer Flange	183	0.37
III – Middle of Stringer	357	0.73
IV – Directly over Shear Tie	563**	1.15**

* Denotes approximate values

** Values were established based on visual and tactile damage only

Although all impact locations developed visually and tactilely detectable damage from the back side of the panel (i.e., non-impacted side), few left any evidence of a damage-producing impact incident on the front side of the panel. Impact Types I through III showed no visual nor tactile detectability on the impact side of the panel. However, impacts over the shear tie (Type IV) caused paint over

the countersunk fasteners to chip (non- structural damage). This was the only location to indicate any occurrence of an impact. In spite of paint damage being apparent, structural damage at the location was difficult to ascertain due to the complexity of the geometry of the shear ties.

By observing the FTE of different impact locations and comparing the local "boundary conditions" around the SOI to each other, one can conclude there was a relationship between damage initiation, bending stiffness in the region of impact, and areas of stress concentration. Middle of the bay impacts (Type I) most resembled the previously tested [19] monolithic 305 x 305 mm flat panels held in a picture-frame fixture. In comparison to the flat panels, the mid-bay region had a lower bending stiffness, and showed FTE values ranging from 0.46 to 1.16 times the baseline. This range was most likely due to the varying proximity of the impact to the nearest stringer flange and/or shear tie. As mentioned previously, impacts on the stringer flange (Type II) were the most critical. The stringer flanges were thick which increases stiffness, but were surrounded by numerous areas of stress concentration (i.e., corners of the stringer, and skin and stringer joints). The corners where the stringer bends to conform with and attach to the skin were particular areas of high stress. Furthermore, high peel stresses developed in the stringer flanges due to the direct transverse loading applied to the skin.

Impacts on the middle of the stringer (Type III) had the next highest scaling factor of 0.73. The middle of the stringer location had a high bending stiffness due to the short span created by the stringer walls. This produced higher contact forces during the SHI interaction with the panel face. Impacts directly on the shear

tie (Type IV) also had a high bending stiffness due to the geometry of the shear tie, but developed high stresses at the curved section of the angle shape resulting in bending-induced fiber failure. Type IV impact had a high scaling factor of 1.15, but was established based on visually and tactilely detectable damage only. These observations implied that although high velocity impacts with small mass were known to be independent of global boundary conditions, they were also dependent on the impact site's peripheral boundary conditions affecting local bending stiffness, such as where the skin and hat stringer stiffeners met.

Comparing results of various NDI methods showed a variance in damage areas. Most notable was the level of error between the different A-scans. This enforced the need for a damage tolerance program to ensure the safety of an aircraft's structure.

4.2 CONCLUSIONS

The following conclusions can be drawing from this research:

- SHI impact directly onto stringer flanges had the lowest FTE relative to impacts onto the skin, and led to extensive delamination such as unzipping of the stringer flange. Thus, for transverse impact, stringer flanges are critical regions of an aircraft fuselage, and detailed inspections should be directed to these locations to find any damage after a hail impact event (and sever impact events, in general).
- Impacts directly over the shear tie were the only location that consistently indicated any occurrence that an impact has occurred due to the resulting paint damage around the fasteners. In spite of the

paint damage being apparent, structural damage at the location was not definite (i.e., not always present).

- The damage progressions provide insight to possible damage modes as a function of increasing impact severity and location of impact. Those damage modes are key to defining the critical impact locations relative to the stiffeners. Knowledge of the damage modes and extent of damage is fundamental to the selection of suitable NDE methods and for conducting damage tolerance evaluation of the structure.
- Although composite panel skin impacts involving high velocity with small mass projectiles were known to often be independent of the panel's overall global boundary conditions, the resulting damage formation in stringer-stiffened panels was found to be highly dependent on local peripheral boundary conditions surrounding the immediate impact site. These peripheral boundary conditions, formed by the stiffening elements such as the stringers and shear ties, directly affect local bending stiffness, and can produce bending stress concentrations at locations such as where the skin and hat stringer stiffeners meet.
- Comparing results of various NDI methods showed a variance in the detected damage areas. Most notable was the level of error between the different A-scans. This enforces the need for a damage tolerance program to be conservative (i.e., assumes larger worst-case damage size) to ensure the safety of an aircraft structure's safe operation even in the presence of undetected damage.

- The scaling factors, defined for each location of impact relative to the stringers, enables FTE and impact data of monolithic flat panel specimens to be applicable to predicting damage onset in stiffened-skin panel structural configurations.

REFERENCES

[1] Roeseler WG, Sarh B, Kismarton MU. Composite Structures: The First 100 Years. Proceedings of the 16th International Conference on Composite Materials, Kyoto, Japan: 2007, p. 1–10.

[2] Shocron A. Picture of the Lockheed L-1011-385-1-14 TriStar 150 Aircraft. The Wings of the Web 2001. Accessed 11 May 2013. http://www.airliners.net/photo/Air-Transat/Lockheed-L-1011-385-1-14-TriStar/0186981/L/

[3] Saul M, Lunford L. Damage From Hail Grounds Nearly 100 D/FW Planes Passengers Scramble as Scores of Flights Cancelled. Dallas Morning News. 1 May 1995

[4] Frontier Airlines Releases Photos of Hail Damage To Planes. CBS4 Denver 2011. 14 July 2011. Accessed 11 May 2013. denver.cbslocal.com/2011/07/14/frontier-airlines-releases-photos-of-hail-damage-to-planes

[5] Federal Aviation Administration. Advisory Circular 20-107A, Composite Aircraft Structure. 25 April 1985.

[6] Halpin J, Kim H. Managing Damage Threats for Composite Structures : Unifying Durability and Damage Tolerance Perspective. Proceedings of the FAA/EASA Meeting., Tokyo: 2009.

[7] Jackson, W.C. and Poe Jr., C.C. The Use of Impact Force as a Scale Parameter for the Impact Response of Composite Laminates. NASA Technical Memorandum 104189, US Army Aviation Systems Command (AVSCOM) Technical Report 92-B-001. January 1992

[8] Morton WJC. Comparison of the Low and High Velocity Impact Response of CFRP. Composites 1989;20:545–51.

[9] Naik NK, Shrirao P. Composite Structures Under Ballistic Impact. Composite Structures 2004;66:579–90.

[10] Davies GAO, Zhang X. Impact Damage Prediction in Carbon Composite Structures. International Journal of Impact Engineering 1995;16:149–70.

[11] Davies GAO, Zhang X, Zhou G, Watson S. Numerical Modelling of Impact Damage. Composites 2000;25:342–50.

[12] Schoeppner G a., Abrate S. Delamination Threshold Loads for Low Velocity Impact on Composite Laminates. Composites Part A: Applied Science and Manufacturing 2000;31:903–15.

[13] Abrate S. Modeling of Impacts on Composite Structures. Composite Structures 2001;51:129–38.

[14] Hou JP, Ruiz C. Soft Body Impact on Laminated Composite Materials. Composites Part A: Applied Science and Manufacturing 2007;38:505–15.

[15] Johnson AF, Holzapfel M. Modelling Soft Body Impact on Composite Structures. Composite Structures 2003;61:103–13.

[16] Ivančević D, Smojver I. Hybrid Approach in Bird Strike Damage Prediction on Aeronautical Composite Structures. Composite Structures 2011;94:15–23.

[17] Georgiadis S, Gunnion AJ, Thomson RS, Cartwright BK. Bird-strike Simulation for Certification of the Boeing 787 Composite Moveable Trailing Edge. Composite Structures 2008;86:258–68.

[18] Kim H, Welch DA, Kedward KT. Experimental Investigation of High Velocity Ice Impacts on Woven Carbon/Epoxy Composite Panels. Composites Part A: Applied Science and Manufacturing 2003;34:25–41.

[19] Rhymer J, Kim H, Roach D. The Damage Resistance of Quasi-Isotropic Carbon/Epoxy Composite Tape Laminates Impacted by High Velocity Ece. Composites Part A: Applied Science and Manufacturing 2012;43:1134–44.

[20] Park H, Kim H. Damage Resistance of Single Lap Adhesive Composite Joints by Transverse Ice Impact. International Journal of Impact Engineering 2010;37:177–84.

[21] Park H. Resistance of Adhesively Bonded Composite Lap Joints to Damage by Transverse Ice Impact. Purdue University, 2006.

[22] Kairouz KC, Matthews FL. Strength and Failure Modes of Bonded Single Lap Joints Between Cross-Ply Adherends. Composites 1993;24:475–84.

[23] Kim H, Kayir T, Mousseau S. Mechanisms of Damage Formation in Transversely Impacted Glass-Epoxy Bonded Lap Joints. Journal of Composite Materials 2005;39:2039–52.

[24] Greenhalgh E, Meeks C, Clarke A, Thatcher J. The effect of defects on the performance of post-buckled CFRP stringer-stiffened panels. Composites Part A: Applied Science and Manufacturing 2003;34:623–33.

[25] Wiggenraad JEM, Aoki R, Gadke M, Greenhalgh E, Hachenberg D, Wolf K, et al. Damage propagation in composite structural elements - analysis and experiments on structures. Composite Structures 1997;36:173–86.

[26] Faggiani A, Falzon BG. Predicting low-velocity impact damage on a stiffened composite panel. Composites Part A: Applied Science and Manufacturing 2010;41:737–49.

[27] Suh SS, Han NL, Yang JM, Hahn HT. Compression Behavior of Stitched Stiffened Panel with a Clearly Visible Stiffener Impact Damage. Composite Structures 2003;62:213–21.

[28] Ice Drop. How to make clear ice. 28 February 2011. Victoria, BC, Canada. Accessed 11 May 2013. http://www.icedropmaker.com/2011/02/how-to-make-clear-ice-that-actually-works/

[29] Graham, J, Johnston, WA, Nicholson, FJ. Ice in Fisheries. FAO Fisheries Technical Paper No. 331. Rome, FAO. 1992. 75p.

[30] Ask the Van (Department of Physics, University of Illinois at Urbana-Champaign). What is deionized water? 2007. Accessed 11 May 2013. http://van.physics.illinois.edu/qa/listing.php?id=22654

[31] Funai S. Hail Ice Impact on Composite Structures at Glancing Angles. University of California, San Diego, 2012.

[32] Kim H. 5 Step-lap Joint Model. SE 171 Lecture Notes. University of California, San Diego. La Jolla, CA. Lecture.

APPENDIX A: SIMULATED HAIL ICE MANUFACTURING

A.1 MODIFIED SHI MANUFACTURING PROCEDURE

This appendix documents the improved procedure for making and demolding ice spheres such that they contain reduced amount of flaws.

Making 61.0 m SHI

1. Run aluminum and steel ice molds under warm water until all pieces are warm.
2. Use a paper towel to dry the interior of the molds.
3. Cover interior of molds with Smooth-On mold release.
4. Place a thin film/layer of petroleum jelly onto the edge of the lower mold. Remove any excess on the interior of the mold so as not to affect the resulting ice sphere.
5. Fill lower mold with previously boiled chilled distilled water.
6. Cover lower mold with upper mold and hammer tap the edges of the aluminum mold.
7. Place aluminum mold into C-clamps and tighten.
8. Using the large syringe, fill the mold with water using the top fill hole. Fill until water overfills and most air bubbles have exited the mold.
9. Using the small syringe, remove all excess water sitting on top of the aluminum mold.
10. Using the small syringe, remove 7 mL from inside the aluminum mold and fill hole. Dispose this water.

11. Set ice molds in freezer set at -5 °C (23 °F) to -12 °C (10.4 °F).

Removing Ice From Molds

1. Run bottom steel clamping piece (pipe flange) under room temperature water.
2. Run top steel clamping piece under room temperature water. Run nuts and bolts under water. Be careful. Evenly wet the mold all around its outer surface. Warming up the mold unevenly will produce uneven pressure/forces being applied onto the ice and may fracture the ice. In addition, be careful not to get water in the water injection whole or anywhere the water can make direct contact with the SHI. This can cause cracking of ice sphere.

A.2 PREVIOUS SHI MANUFACTURING PROCEDURE

Making 61.0 Ice

1. Use a paper towel to dry the interior of the molds.
2. Cover interior of molds with Smooth-On mold release.
3. Fill lower mold with chilled deionized water.
4. Cover lower mold with upper mold half.
5. Place the closed mold into C-clamps and tighten.
6. Using a large syringe, fill the mold with water using the top fill hole. Fill until water overfills and have exited the mold.
7. Using the small syringe, remove all excess water on top of the aluminum mold.

8. Using the small syringe, remove 7 mL from inside the aluminum mold and dispose this water.

Removing Ice From Molds

1. Remove ice molds from the freezer and dunk into a container filled with room temperature water. The water should only reach the middle of the mold.
2. Run the nuts and bolts under water.
3. Loosen the nuts and bolts and slowly remove the top side of the mold. Once the mold pieces are separated, remove the SHI.

APPENDIX B: BINOMIAL LOGISTIC REGRESSION

Mathematica was used for binomial logistic regression to determine FTE in various cases. Series of data were input as matrix *data1638*. The x-coordinate was set to impact energy, and the y-coordinate was set to zero (0) for no damage and one (1) for damage. This program produced a plot, the FTE based on the input data. A sample of the input code and output code is provided in this appendix.

Input Code:

```
data1638={(*{313.3, NA}*)
  {161.2,0},
  (*{227,1},
  {295.4,1}, *)
  {307.2,0},
  {430.7,0},
  {432.9,0},
  {445,0},
  {460.3,0},
  {540,0},
  {546.8,0},
  {562.3,1},
  {566.5,0},
  {665.5,1},
  {720.5,1},
  {734.8,1},
  {745.6,1}}
logit1638=LogitModelFit[data1638,x,x];
Normal[logit1638]
logit1638["LikelihoodRatioStatistic"];
param1638=logit1638["BestFitParameters"];
logit1638["PredictedResponse"];
(** fitted values for the data **)
Show[ListPlot[data1638,PlotMarkers-
>{Automatic,8}],Plot[logit1638[x],{x,0,800}],
 (*PlotRange-> {{0,800},{0,1}}, *)
 Frame->True, FrameTicks->{{{0,1},None},{All,None}},
 FrameLabel->{{"Damage"," "}, {"Energy [J]"," "}},
 BaseStyle->{FontFamily->"Century Gothic",FontSize->10,
FontWeight->"Bold"}]
(*Show[ListPlot[data1638],Plot[logit1638[x],{x,1,800}]]*)
ten1638=Solve[logit1638[x]==.1,x]
```

```
mean1638 = -param1638[[1]]/param1638[[2]]
```

Output Code:

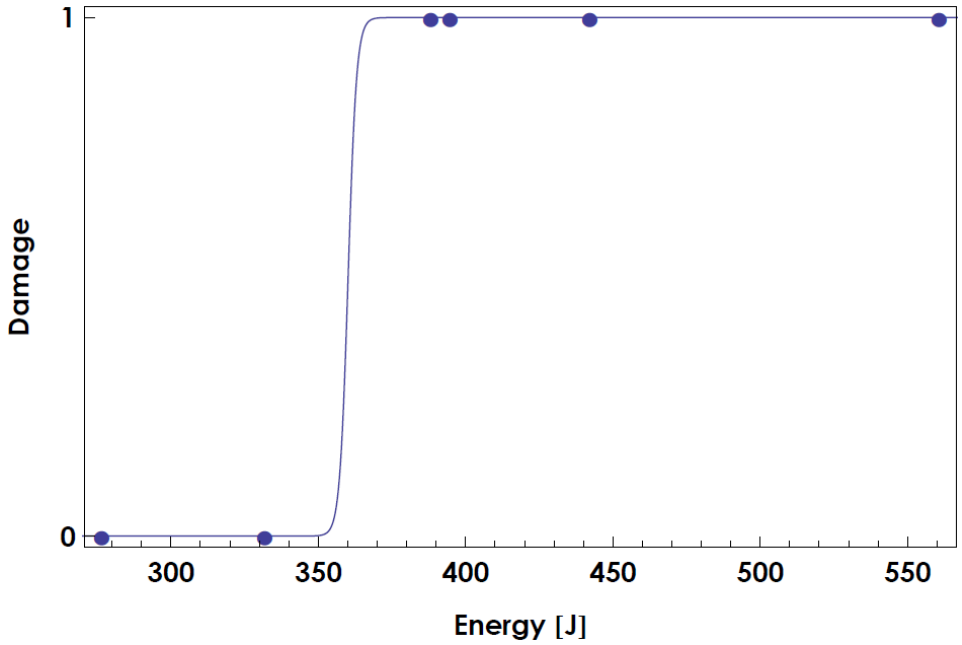


```
{{x -> 548.528}}
```

APPENDIX C: IMPACT LOCATION NOMENCLATURE

Nomenclature was developed to identify the locations of impacts on each panel. A bay was defined to be the space between two columns of shear ties. The skin was defined as the skin between the stringers.

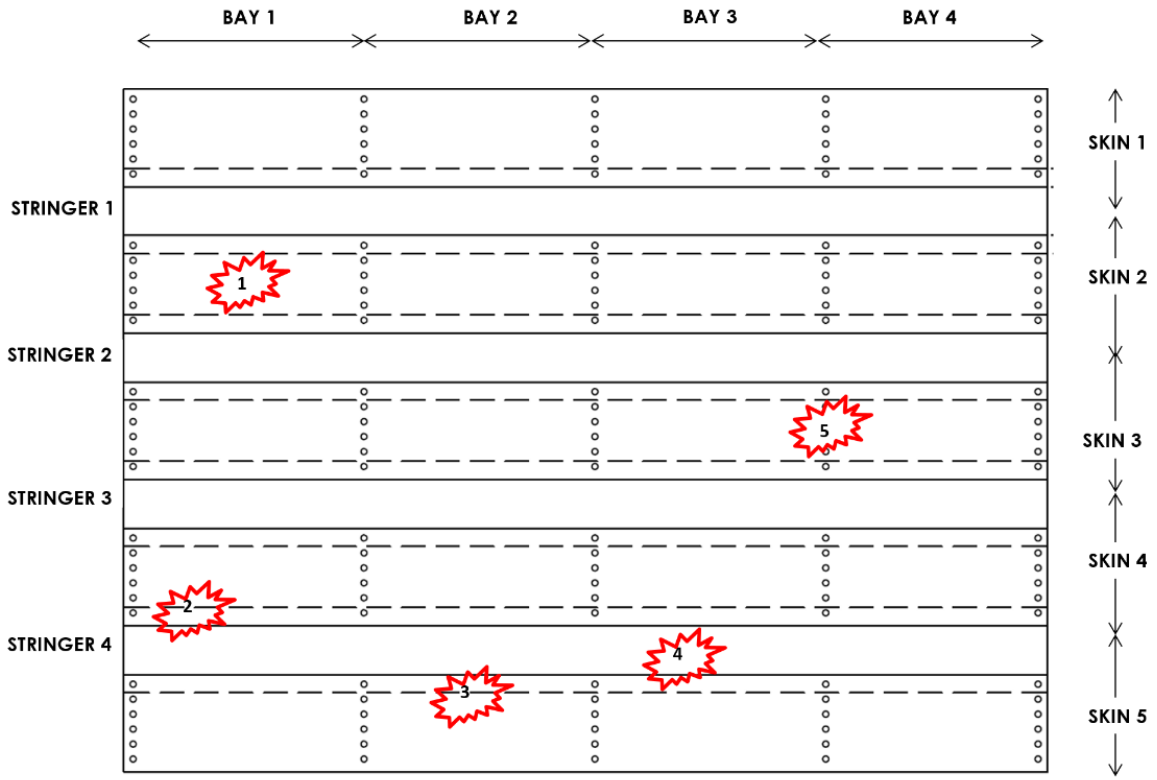

Figure 47: Examples of Location Nomenclature

BAY#.SKIN#.STRINGER# - Impact Type

- Refer to bay closest to the left (see example impact 5)
- Refer to skin closest to the top (see example impact 4)
- Refer to shear ties like matrix indexes – (row, column) (see example impact 5)

EXAMPLES:

Impact 1: B1.SK2-I1
Impact 2: B1.SK4.ST4-I2a
Impact 3: B2.SK5.ST4-I2a
Impact 4: B3.ST4-I3
Impact 5: B3.SK3-I4.34 (Bay-always refer to bay on left; 34 indicates shear tie row 3, column 4)

APPENDIX D: TEST DATA TABLES

Table D1. Test Data Summary Table Ordered by Test Number

Test #	Date	Panel-BAY#.SKIN#. STRINGER#-ImpactType	Impact Coordinates (X [in], Y [in])	SHI Mass [g]	Time [µs]	Pressure [psi]	Velocity [m/s]	Energy [J]	Knock-down Factor	SOI Damage [mm^2]	Further Damage [mm^2]	Damage?	Notes
SP001	2/27/12	A-B1.SK4-I1	(13.75, 16.125)	107.0	N/A	167	N/A	N/A	N/A	--	--	--	Bad SHI. SHI broke after sabot stop. No damage visible on impact side.
SP002	2/27/12	A-B1.SK4-I1	(13.75, 16.125)	104.9	1666	169	76.5	307.2	0.63	25,108	30,720	0	No damage SOI. Seeking damage at SOI. Damage in stringers unknown.
SP003	2/27/12	A-B1.SK4-I1	(13.75, 16.125)	107.3	1423	221	89.6	430.7	0.88	29,396	43,071	0	No damage SOI; Damage in stringers unknown.
SP004	2/27/12	A-B1.SK4-I1	(13.75, 16.125)	109.1	1388	232	91.9	460.3	0.94	30,137	46,029	0	No damage SOI; Damage in stringers unknown.
SP005	2/27/12	A-B1.SK4-I1	(13.75, 16.125)	108.0	1267	298	100.6	546.8	1.12	33,016	54,684	1	No damage at POI. Delam in flanges at top left and bottom right SOI. On backside, only top left is detectable.
SP006	2/27/12	A-B1.SK5.ST4-I2a	(13.75, 7.25)	104.8	1423	221	89.6	420.7	0.86	29,396	42,067	1	Damage at SOI. Unzipped 75% of flange. On backside, damage is very visible.
SP007	2/27/12	A-B2.SK5.ST4-I2a	(26.5, 7.375)	106.8	1770	157	72.0	277.1	0.57	0	27,709	1	No damage at SOI; delam in flanges several inches away from SOI all the way to the end of the bay. On backside, no visible damage.
SP008	2/28/12	A-B2.SK4-I1	(29, 16)	108.9	1250	360	102.0	566.5	1.16	0	0	1	Damage was not mapped after this 1st impact, but damage was detected prior to 2nd impact (SP009).
SP009	2/28/12	A-B2.SK4-I1	(29, 16)	105.9	1093	446	116.7	720.5	1.47	38,271	72,052	1	Damage at SOI extends to bottom flange. Bottom flange is delaminated from end to end. On the backside, very little damage is visible; only thing visible is at the top right.
SP010	2/29/12	B-B1.SK4-I1	(13.75, 16.125)	108.1	1250	311	102.0	562.3	1.15	33,465	56,234	1	Small delam. Non-visible damage at SOI and along one stringer. Non-visible on backside.
SP011	2/29/12	B-B2.SK4-I1	(29.25, 16)	106.2	1076	451	118.5	745.6	1.52	38,876	74,557	1	Large, delam at SOI. Small delam along lower stringer. Damage not visible on backside.
SP012	2/29/12	B-B2.SK5.ST4-I2a	(26.375, 7.125)	105.5	1736	156	73.4	284.5	0.58	24,096	28,454	1	Flange unzipped from shear tie to shear tie. Delam of tapered flange was tactile. Impact directly underneath fiber optics, broke fiber.
SP013	2/29/12	B-B1.SK5.ST4-I2a	(14.75, 7.25)	108.2	1775	216	71.8	279.1	0.57	23,567	27,914	1	Delam on lap joint. Nothing visible on paint side. Flange unzipped from shear tie to shear tie. Delam of tapered flange could be felt. impact between two fiber optics, broke fiber optics.
SP014	3/14/12	B-B1.SK5-I4.52	(21, 6.375)	108.3	1514	230	84.2	384.0	0.79	--	--	0	No Damage.

Table D1. Test Data Summary Table Ordered by Test Number (Continued)

Test #	Date	Panel-BAY#.SKIN#. STRINGER#-ImpactType	Impact Coordinates (X [in], Y [in])	SHI Mass [g]	Time [µs]	Pressure [psi]	Velocity [m/s]	Energy [J]	Knock-down Factor	SOI Damage [mm^2]	Further Damage [mm^2]	Damage?	Notes
SP015	3/14/12	B-B1.SK5-I4.52	(21, 6.375)	107.2	1094	430	116.5	728.0	1.49	--	--	1	Damage along back of sheartie. Delam underneath shear tie.
SP016	3/14/12	B-B1.SK4-I4.42	(20.75, 16.25)	106.2	1346	260	94.7	476.5	0.97	--	--	0	Chipped paint, but no stringer damage.
SP017	3/14/12	B-B1.SK4-I4.42	(20.75, 16.25)	107.1	1086	404	117.4	738.1	1.51	--	--	1	Damage
SP018	3/14/12	B-B1.SK3-I4.32	(20.625, 28)	108.0	1145	362	111.4	N/A	N/A	--	--		Bad SHI. Damage.
SP019	3/14/12	B-B1.SK3.ST3-I2b	(13.75, 25)	107.7	N/A	103	61.1	201.3	0.41	20,059	20,130	1	Damage. BARELY tactilely detectable delam of flange
SP020	3/14/12	B-B2.SK3.ST3-I2a	(28.75, 25.75)	107.9	2256	110	56.5	172.3	0.35	18,542	17,232	1	Damage
SP021	3/15/12	B-B4.SK2-I1	(62.625, 40.25)	106.7	1396	231	91.3	445.0	0.91	29,965	44,502	0	No damage
SP022	3/15/12	B-B4.SK2-I1	(62.625, 40.25)	105.8	1262	306	101.0	540.0	1.10	33,146	53,995	0	No damage
SP023	3/15/12	B-B4.SK2-I1	(62.625, 40.25)	108.1	1149	386	111.0	665.5	1.36	36,406	66,554	1	Damage
SP024	3/15/12	B-B4.SK1-I1	(61.375, 52.25)	108.3	1426	231	89.4	432.9	0.89	29,334	43,289	0	No damage
SP025	3/15/12	B-B4.SK1-I1	(61.375, 52.25)	108.5	1266	319	100.7	550.2	1.13	--	--	--	Bad SHI.
SP026	3/15/12	B-B4.SK1-I1	(61.375, 52.25)	107.4	1090	406	117.0	734.8	1.50	38,377	73,475	1	Damage at SOI and in stringer. Last impact after SP024, SP025.
SP027	3/15/12	A-B1.ST4-I3	(61.75, 46.25)	106.8	1401	230	91.0	442.3	0.90	29,858	44,227		A-scan broke, cannot detect damage.
SP028	3/26/12	B-B3.SK1.ST1-I2b	(51, 48.5)	102.2	1472	223	86.6	383.4	0.78	28,418	38,338	1	Bad SHI
SP029	3/26/12	B-B3.SK2.ST1-I2a	(50.875, 42.25)	107.1	1434	220	88.9	423.3	0.87	29,171	42,333	1	delam stringer. Tactile. Partially unzipped
SP030	3/26/12	B-B3.SK2.ST2-I2b	(51, 36.5)	103.2	1434	224	88.9	407.9	0.83	29,171	40,792	1	Delam stringer. Tactilely detectable. Partially unzipped.
SP031	3/28/12	A-B3.ST1-I3	(47.8125, 45.5)	103.4	1459	230	87.4	394.8	0.81	28,671	39,482	1	A-Scan detected damage in stringer.
SP032	3/28/12	A-B3/4.ST1-I3	(53.8125, 45.76)	107.8	1250	302	102.0	560.8	1.15	33,465	56,078	1	A-Scan detected damage in stringer.
SP033	5/3/12	A-B4.SK2.ST2-I2b	(47.6875, 36.75)	103.2	2266	81	56.3	163.4	0.33	18,460	16,336	0	No Damage
SP034	5/3/12	A-B4.SK2.ST2-I2b	(47.6875, 36.75)	104.7	2167	109	58.8	181.2	0.37	19,304	18,123	0	No Damage
SP035	5/3/12	A-B4.SK2.ST2-I2b	(47.6875, 36.75)	104.4	1936	138	65.9	226.4	0.46	21,607	22,640	0	Small lip on back, barely feel it; nothing on A-scan. Tactical detectable damage, but not detectable with A-scan. Can feel the lip/lift of one of the plies. Probably due to high peel stresses.
SP036	5/3/12	A-B4.SK2.ST2-I2b	(47.6875, 36.75)	106.1	1768	149	72.1	275.9	0.56	23,660	27,589	1	Damage. Very small.
SP037	5/11/12	A-B3.SK2.ST2-I2b	(47.625, 31.25)	102.4	1858	139	68.6	241.1	0.49	0	0	0	No Damage
SP038	5/11/12	A-B3.SK2.ST2-I2b	(47.625, 31.25)	107.4	1816	148	70.2	264.7	0.54	23,035	26,471	1	Damage. Small, not visible damage, but A-Scan detectable.
SP039	5/11/12	A-B4.ST2-I3	(62.0625, 34.1875)	105.5	1761	153	72.4	276.5	0.57	23,754	27,652	0	No Damage
SP040	5/11/12	A-B4.ST2-I3	(62.0625, 34.1875)	104.2	1598	178	79.8	331.7	0.68	26,177	33,167	0	No Damage
SP041	5/11/12	A-B4.ST2-I3	(62.0625, 34.1875)	103.5	1472	213	86.6	388.3	0.79	28,418	38,825	1	Damage. Small. Not visible damage, but A-scan detectable.
SP042	6/1/12	A-B2.SK3.I1	(28, 28)	106.9	1715	161	74.3	295.4	0.60	24,391	29,542	1	Damage behind impacted location.
SP043	6/1/12	A-B1.SK3.I1	(14.5, 28)	107.0	2323	100	54.9	161.2	0.33	18,007	16,117	0	No Damage
SP044	6/1/12	A-B1.SK3.I1	(14.5, 28)	100.3	1895	134	67.3	227.0	0.46	22,074	22,702	1	Delam at SOI; No Damage to stringer.
SP045	6/1/12	A-B1.SK3.I1	(18.5, 28)	99.8		210	83.4	347.1	0.71	27,362	34,708	1	Delam along stringer.

NOTES: Grey fields denote SHI broke prior to impacting target.

Table D2. Test Data Summary Table Ordered by Impact Location and Energy

Test #	Date	Panel-BAY#.SKIN#. STRINGER#-ImpactType	Impact Coordinates (X [in], Y [in])	SHI Mass [g]	Time [µs]	Pressure [psi]	Velocity [m/s]	Energy [J]	Knock-down Factor	SOI Damage [mm^2]	Further Damage [mm^2]	Damage?	Notes
IMPACT TYPE I													
SP001	2/27/12	A-B1.SK4-I1	(13.75, 16.125)	107.0	N/A	167	N/A	N/A	N/A	--	--	--	Bad SHI. SHI broke after sabot stop. No damage visible on impact side.
SP025	3/15/12	B-B4.SK1-I1	(61.375, 52.25)	108.5	1266	319	100.7	N/A	N/A	--	--	--	Bad SHI.
SP043	6/1/12	A-B1.SK3.I1	(14.5, 28)	107.0	2323	100	54.9	161.2	0.33	18,007	16,117	0	No Damage
SP044	6/1/12	A-B1.SK3.I1	(14.5, 28)	100.3	1895	134	67.3	227.0	0.46	22,074	22,702	1	Delam at SOI; No Damage to stringer.
SP042	6/1/12	A-B2.SK3.I1	(28, 28)	106.9	1715	161	74.3	295.4	0.60	24,391	29,542	1	Damage behind impacted location.
SP002	2/27/12	A-B1.SK4-I1	(13.75, 16.125)	104.9	1666	169	76.5	307.2	0.63	25,108	30,720	0	No damage SOI. Seeking damage at SOI. Damage in stringers unknown.
SP045	6/1/12	A-B1.SK3.I1	(18.5, 28)	99.8		210	83.4	347.1	0.71	27,362	34,708	1	Delam along stringer.
SP003	2/27/12	A-B1.SK4-I1	(13.75, 16.125)	107.3	1423	221	89.6	430.7	0.88	29,396	43,071	0	No damage SOI; Damage in stringers unknown.
SP024	3/15/12	B-B4.SK1-I1	(61.375, 52.25)	108.3	1426	231	89.4	432.9	0.89	29,334	43,289	0	No damage
SP021	3/15/12	B-B4.SK2-I1	(62.625, 40.25)	106.7	1396	231	91.3	445.0	0.91	29,965	44,502	0	No damage
SP004	2/27/12	A-B1.SK4-I1	(13.75, 16.125)	109.1	1388	232	91.9	460.3	0.94	30,137	46,029	0	No damage SOI; Damage in stringers unknown.
SP022	3/15/12	B-B4.SK2-I1	(62.625, 40.25)	105.8	1262	306	101.0	540.0	1.10	33,146	53,995	0	No damage
SP005	2/27/12	A-B1.SK4-I1	(13.75, 16.125)	108.0	1267	298	100.6	546.8	1.12	33,016	54,684	1	No damage at POI. Delam in flanges at top left and bottom right SOI. On backside, only top left is detectable.
SP010	2/29/12	B-B1.SK4-I1	(13.75, 16.125)	108.1	1250	311	102.0	562.3	1.15	33,465	56,234	1	Small delam. Non-visible damage at SOI and along one stringer. Non-visible on backside.
SP008	2/28/12	A-B2.SK4-I1	(29, 16)	108.9	1250	360	102.0	566.5	1.16	0	0	1	Damage was not mapped after this 1st impact, but damage was detected prior to 2nd impact (SP009).
SP023	3/15/12	B-B4.SK2-I1	(62.625, 40.25)	108.1	1149	386	111.0	665.5	1.36	36,406	66,554	1	Damage
SP009	2/28/12	A-B2.SK4-I1	(29, 16)	105.9	1093	446	116.7	720.5	1.47	38,271	72,052	1	Damage at SOI extends to bottom flange. Bottom flange is delaminated from end to end. On the backside, very little damage is visible; only thing visible is at the top right.
SP026	3/15/12	B-B4.SK1-I1	(61.375, 52.25)	107.4	1090	406	117.0	734.8	1.50	38,377	73,475	1	Damage at SOI and in stringer. Last impact after SP024, SP025.
SP011	2/29/12	B-B2.SK4-I1	(29.25, 16)	106.2	1076	451	118.5	745.6	1.52	38,876	74,557	1	Large, delam at SOI. Small delam along lower stringer. Damage not visible on backside.

Table D2. Test Data Summary Table Ordered by Impact Location and Energy (Continued)

Test #	Date	Panel-BAY#.SKIN#. STRINGER#-ImpactType	Impact Coordinates (X [in], Y [in])	SHI Mass [g]	Time [µs]	Pressure [psi]	Velocity [m/s]	Energy [J]	Knock-down Factor	SOI Damage [mm^2]	Further Damage [mm^2]	Damage?	Notes
IMPACT TYPE II													
SP020	3/14/12	B-B2.SK3.ST3-I2a	(28.75, 25.75)	107.9	2256	110	56.5	172.3	0.35	18,542	17,232	1	Damage
SP029	3/26/12	B-B3.SK2.ST1-I2a	(50.875, 42.25)	107.1	1434	220	88.9	423.3	0.87	29,171	42,333	1	delam stringer. Tactile. Partially unzipped
SP033	5/3/12	A-B4.SK2.ST2-I2b	(47.6875, 36.75)	103.2	2266	81	56.3	163.4	0.33	18,460	16,336	0	No Damage
SP034	5/3/12	A-B4.SK2.ST2-I2b	(47.6875, 36.75)	104.7	2167	109	58.8	181.2	0.37	19,304	18,123	0	No Damage
SP019	3/14/12	B-B1.SK3.ST3-I2b	(13.75, 25)	107.7	N/A	103	61.1	201.3	0.41	20,059	20,130	1	Damage. BARELY tactilely detectable delam of flange
SP035	5/3/12	A-B4.SK2.ST2-I2b	(47.6875, 36.75)	104.4	1936	138	65.9	226.4	0.46	21,607	22,640	0	Small lip on back, barely feel it; nothing on A-scan. Tactical detectable damage, but not detectable with A-scan. Can feel the lip/lift of one of the plies. Probably due to high peel stresses.
SP037	5/11/12	A-B3.SK2.ST2-I2b	(47.625, 31.25)	102.4	1858	139	68.6	241.1	0.49	0	0	0	No Damage
SP038	5/11/12	A-B3.SK2.ST2-I2b	(47.625, 31.25)	107.4	1816	148	70.2	264.7	0.54	23,035	26,471	1	Damage. Small, not visible damage, but A-Scan detectable.
SP036	5/3/12	A-B4.SK2.ST2-I2b	(47.6875, 36.75)	106.1	1768	149	72.1	275.9	0.56	23,660	27,589	1	Damage. Very small.
SP007	2/27/12	A-B2.SK5.ST4-I2a	(26.5, 7.375)	106.8	1770	157	72.0	277.1	0.57	0	27,709	1	No damage at SOI; delam in flanges several inches away from SOI all the way to the end of the bay. On backside, no visible damage.
SP013	2/29/12	B-B1.SK5.ST4-I2a	(14.75, 7.25)	108.2	1775	216	71.8	279.1	0.57	23,567	27,914	1	Delam on lap joint. Nothing visible on paint side. Flange unzipped from shear tie to shear tie. Delam of tapered flange could be felt. impact between two fiber optics, broke fiber optics.
SP012	2/29/12	B-B2.SK5.ST4-I2a	(26.375, 7.125)	105.5	1736	156	73.4	284.5	0.58	24,096	28,454	1	Flange unzipped from shear tie to shear tie. Delam of tapered flange was tactile. Impact directly underneath fiber optics, broke fiber.
SP028	3/26/12	B-B3.SK1.ST1-I2b	(51, 48.5)	102.2	1472	223	86.6	383.4	0.78	28,418	38,338	1	Bad SHI
SP030	3/26/12	B-B3.SK2.ST2-I2b	(51, 36.5)	103.2	1434	224	88.9	407.9	0.83	29,171	40,792	1	Delam stringer. Tactilely detectable. Partially unzipped.
SP006	2/27/12	A-B1.SK5.ST4-I2a	(13.75, 7.25)	104.8	1423	221	89.6	420.7	0.86	29,396	42,067	1	Damage at SOI. Unzipped 75% of flange. On backside, damage is very visible.

Table D2. Test Data Summary Table Ordered by Impact Location and Energy (Continued)

Test #	Date	Panel-BAY#.SKIN#. STRINGER#-ImpactType	Impact Coordinates (X [in], Y [in])	SHI Mass [g]	Time [µs]	Pressure [psi]	Velocity [m/s]	Energy [J]	Knock-down Factor	SOI Damage [mm^2]	Further Damage [mm^2]	Damage?	Notes
IMPACT TYPE III													
SP039	5/11/12	A-B4.ST2-I3	(62.0625, 34.1875)	105.5	1761	153	72.4	276.5	0.57	23,754	27,652	0	No Damage
SP040	5/11/12	A-B4.ST2-I3	(62.0625, 34.1875)	104.2	1598	178	79.8	331.7	0.68	26,177	33,167	0	No Damage
SP041	5/11/12	A-B4.ST2-I3	(62.0625, 34.1875)	103.5	1472	213	86.6	388.3	0.79	28,418	38,825	1	Damage. Small. Not visible damage, but A-scan detectable.
SP031	3/28/12	A-B3.ST1-I3	(47.8125, 45.5)	103.4	1459	230	87.4	394.8	0.81	28,671	39,482	1	A-Scan detected damage in stringer.
SP027	3/15/12	A-B1.ST4-I3	(61.75, 46.25)	106.8	1401	230	91.0	442.3	0.90	29,858	44,227		A-scan broke, cannot detect damage.
SP032	3/28/12	A-B3/4.ST1-I3	(53.8125, 45.76)	107.8	1250	302	102.0	560.8	1.15	33,465	56,078	1	A-Scan detected damage in stringer.
IMPACT TYPE IV													
SP014	3/14/12	B-B1.SK5-I4.52	(21, 6.375)	108.3	1514	230	84.2	384.0	0.79	--	--	0	No Damage.
SP016	3/14/12	B-B1.SK4-I4.42	(20.75, 16.25)	106.2	1346	260	94.7	476.5	0.97	--	--	0	Chipped paint, but no stringer damage.
SP015	3/14/12	B-B1.SK5-I4.52	(21, 6.375)	107.2	1094	430	116.5	728.0	1.49	--	--	1	Damage along back of shear tie. Delam underneath shear tie.
SP017	3/14/12	B-B1.SK4-I4.42	(20.75, 16.25)	107.1	1086	404	117.4	738.1	1.51	--	--	1	Damage
SP018	3/14/12	B-B1.SK3-I4.32	(20.625, 28)	108.0	1145	362	111.4	669.6	1.37	--	--		Bad SHI. Damage.

NOTES: Grey fields denote SHI broke prior to impacting target.

Table D3 Raw Test Data Table

Test #	Date	Panel-BAY#.SKIN#. STRINGER#-ImpactType	Impact Coordinates (X [in], Y [in])	Mass: Sabot [g]	Mass: sabot+proj. [g]	SHI Mass [g]	Time [µs]	Pressure [psi]	Video?	Target % FTE	Velocity [m/s]	Energy [J]	Notes (test)
IMPACT TYPE I													
SP001	2/27/12	A-B1.SK4-I1	(13.75, 16.125)	104.9	211.9	107.0	N/A	167	Y	50	N/A	N/A	Ice broke after sabot stop and before target, nothing visible on paint side
SP025	3/15/12	B-B4.SK1-I1	(61.375, 52.25)	126.1	234.6	108.5	1266	319	Y	120	100.7	N/A	Broken ice; Bad ice
SP043	6/1/12	A-B1.SK3.I1	(14.5, 28)	104.9	211.9	107.0	2323	100	N	30	54.9	161.2	No Damage behind impact location, No Damage on stringer
SP044	6/1/12	A-B1.SK3.I1	(14.5, 28)	104	204.3	100.3	1895	134	Y	45	67.3	227.0	--
SP042	6/1/12	A-B2.SK3.I1	(28, 28)	111.1	218	106.9	1715	161	N	50	74.3	295.4	Damage behind impacted location
SP002	2/27/12	A-B1.SK4-I1	(13.75, 16.125)	99.7	204.6	104.9	1666	169	Y	50	76.5	307.2	No Damage
SP045	6/1/12	A-B1.SK3.I1	(18.5, 28)	108.2	208	99.8		210	Y	75	83.4	347.1	--
SP003	2/27/12	A-B1.SK4-I1	(13.75, 16.125)	104.9	212.2	107.3	1423	221	Y	75	89.6	430.7	No Damage
SP024	3/15/12	B-B4.SK1-I1	(61.375, 52.25)	113.3	221.6	108.3	1426	231	Y	100	89.4	432.9	No Damage
SP021	3/15/12	B-B4.SK2-I1	(62.625, 40.25)	97.3	204	106.7	1396	231	Y	100	91.3	445.0	No Damage
SP004	2/27/12	A-B1.SK4-I1	(13.75, 16.125)	103.1	212.2	109.1	1388	232	Y	100	91.9	460.3	No Damage
SP022	3/15/12	B-B4.SK2-I1	(62.625, 40.25)	100.1	205.9	105.8	1262	306	Y	120	101.0	540.0	No Damage
SP005	2/27/12	A-B1.SK4-I1	(13.75, 16.125)	104.2	212.2	108.0	1267	298	Y	120	100.6	546.8	Damage; Delam ~1.5" away, nothing visible on paint side.
SP010	2/29/12	B-B1.SK4-I1	(13.75, 16.125)	120.8	228.9	108.1	1250	311	Y	120	102.0	562.3	Damage; Delam, nothing visible on paint side
SP008	2/28/12	A-B2.SK4-I1	(29, 16)	107.9	216.8	108.9	1250	360	Y	120	102.0	566.5	Damage; Delam, nothing visible on paint side
SP023	3/15/12	B-B4.SK2-I1	(62.625, 40.25)	118.9	227	108.1	1149	386	Y	145	111.0	665.5	Damage
SP009	2/28/12	A-B2.SK4-I1	(29, 16)	100.7	206.6	105.9	1093	446	Y	75	116.7	720.5	Goal was to achieve more extensive damage with second impact. Second impact showed damage; delam, nothing visible on paint side
SP026	3/15/12	B-B4.SK1-I1	(61.375, 52.25)	96.3	203.7	107.4	1090	406	Y	150	117.0	734.8	damage; broke off fiber optic ends, no splicer available
SP011	2/29/12	B-B2.SK4-I1	(29.25, 16)	116.6	222.8	106.2	1076	451	Y	175	118.5	745.6	Damage; More extensive than delam, nothing visible on paint side

Table D3 Raw Data Table (Continued)

Test #	Date	Panel-BAY#.SKIN#. STRINGER#-ImpactType	Impact Coordinates (X [in], Y [in])	Mass: Sabot [g]	Mass: sabot+proj. [g]	SHI Mass [g]	Time [µs]	Pressure [psi]	Video?	Target % FTE	Velocity [m/s]	Energy [J]	Notes (test)
IMPACT TYPE II													
SP020	3/14/12	B-B2.SK3.ST3-I2a	(28.75, 25.75)	106.8	214.7	107.9	2256	110	Y	30	56.5	172.3	Damage
SP029	3/26/12	B-B3.SK2.ST1-I2a	(50.875, 42.25)	97.5	204.6	107.1	1434	220	Y	100	88.9	423.3	Delam stringer. Tactile. Partially unzipped
SP033	5/3/12	A-B4.SK2.ST2-I2b	(47.6875, 36.75)	105.6	208.8	103.2	2266	81	Y	20	56.3	163.4	No Damage
SP034	5/3/12	A-B4.SK2.ST2-I2b	(47.6875, 36.75)	104.4	209.1	104.7	2167	109	N	30	58.8	181.2	No Damage
SP019	3/14/12	B-B1.SK3.ST3-I2b	(13.75, 25)	123	230.7	107.7	N/A	103	Y	30	61.1	201.3	Damage; Can BARELY feel delam of flange
SP035	5/3/12	A-B4.SK2.ST2-I2b	(47.6875, 36.75)	110.6	215	104.4	1936	138	N	45	65.9	226.4	Small lip on back, barely feel it; nothing on Ascan. **Tactical** detectable damage, but not detectable with A-scan. Can feel the lip/lift of one of the plies. Probably due to high **peel stresses.**
SP037	5/11/12	A-B3.SK2.ST2-I2b	(47.625, 31.25)	107.8	210.2	102.4	1858	139	Y	45	68.6	241.1	No Damage
SP038	5/11/12	A-B3.SK2.ST2-I2b	(47.625, 31.25)	107.4	214.8	107.4	1816	148	Y	50	70.2	264.7	Damage; Small, not visible damage, but A-Scan detectable
SP036	5/3/12	A-B4.SK2.ST2-I2b	(47.6875, 36.75)	96	202.1	106.1	1768	149	Y	50	72.1	275.9	Damage! Very small
SP007	2/27/12	A-B2.SK5.ST4-I2a	(26.5, 7.375)	109.8	216.6	106.8	1770	157	Y	50	72.0	277.1	--
SP013	2/29/12	B-B1.SK5.ST4-I2a	(14.75, 7.25)	102.4	210.6	108.2	1775	216	Y	75	71.8	279.1	Impact on midstringer flange; Delam on lap joint, Nothing visible on paint side; Flange unzipped from shear tie to shear tie; Delamination of tapered flange could be felt; Impact between two fiber optics, broke fiber
SP012	2/29/12	B-B2.SK5.ST4-I2a	(26.375, 7.125)	111.4	216.9	105.5	1736	156	Y	50	73.4	284.5	Flange unzipped from shear tie to shear tie; delamination of tapered flange could be felt; impact directly underneath fiber optics, broke fiber
SP028	3/26/12	B-B3.SK1.ST1-I2b	(51, 48.5)	102.1	204.3	102.2	1472	223	Y	100	86.6	383.4	Bad ice
SP030	3/26/12	B-B3.SK2.ST2-I2b	(51, 36.5)	100.2	203.4	103.2	1434	224	Y	100	88.9	407.9	Delam stringer. Tactile. Partially unzipped
SP006	2/27/12	A-B1.SK5.ST4-I2a	(13.75, 7.25)	99.7	204.5	104.8	1423	221	Y	75	89.6	420.7	Impact on mid stringer flange; Damage - zippered delam on stringer, nothing visible on paint side; cracked through tapered flange point of impact; Flange unzipped from shear tie to shear tie; Damage very visible on back side

Table D3. Raw Data Table (Continued)

Test #	Date	Panel-BAY#.SKIN#. STRINGER#-ImpactType	Impact Coordinates (X [in], Y [in])	Mass: Sabot [g]	Mass: sabot+proj. [g]	SHI Mass [g]	Time [µs]	Pressure [psi]	Video?	Target % FTE	Velocity [m/s]	Energy [J]	Notes (test)
IMPACT TYPE III													
SP039	5/11/12	A-B4.ST2-I3	(62.0625, 34.1875)	108.1	213.6	105.5	1761	153	N	50	72.4	276.5	No Damage
SP040	5/11/12	A-B4.ST2-I3	(62.0625, 34.1875)	102.4	206.6	104.2	1598	178	N	65	79.8	331.7	No Damage
SP041	5/11/12	A-B4.ST2-I3	(62.0625, 34.1875)	105	208.5	103.5	1472	213	N	75	86.6	388.3	Damage! Small. Not visible damage, but A-scan detectable
SP031	3/28/12	A-B3.ST1-I3	(47.8125, 45.5)	99.3	202.7	103.4	1459	230	Y	100	87.4	394.8	A-Scan detected damage in stringer
SP027	3/15/12	A-B1.ST4-I3	(61.75, 46.25)	97	203.8	106.8	1401	230	Y	75	91.0	442.3	A-scan broke, cannot detect damage
SP032	3/28/12	A-B3/4.ST1-I3	(53.8125, 45.76)	96	203.8	107.8	1250	302	Y	120	102.0	560.8	A-Scan detected damage in stringer
IMPACT TYPE IV													
SP014	3/14/12	B-B1.SK5-I4.52	(21, 6.375)	127.9	236.2	108.3	1514	230	Y	100	84.2	384.0	No Damage;
SP016	3/14/12	B-B1.SK4-I4.42	(20.75, 16.25)	104	210.2	106.2	1346	260	Y	115	94.7	476.5	Paint chip, but no stringer damage
SP015	3/14/12	B-B1.SK5-I4.52	(21, 6.375)	113.9	221.1	107.2	1094	430	Y	150	116.5	728.0	Damage along back of sheartie; Delam underneath sheartie
SP017	3/14/12	B-B1.SK4-I4.42	(20.75, 16.25)	103.2	210.3	107.1	1086	404	Y	150	117.4	738.1	Damage!
SP018	3/14/12	B-B1.SK3-I4.32	(20.625, 28)	109.9	217.9	108.0	1145	362	Y	135	111.4	669.6	Damage! Bad ice (10th chipped from back)

NOTES: Grey fields denote SHI broke prior to impacting target.

APPENDIX E: PHOTOGRAPHS OF DAMAGE AREAS

This appendix presents photographs of the front side and the back side of SOIs and the regions around them. The photographs are organized by test number.

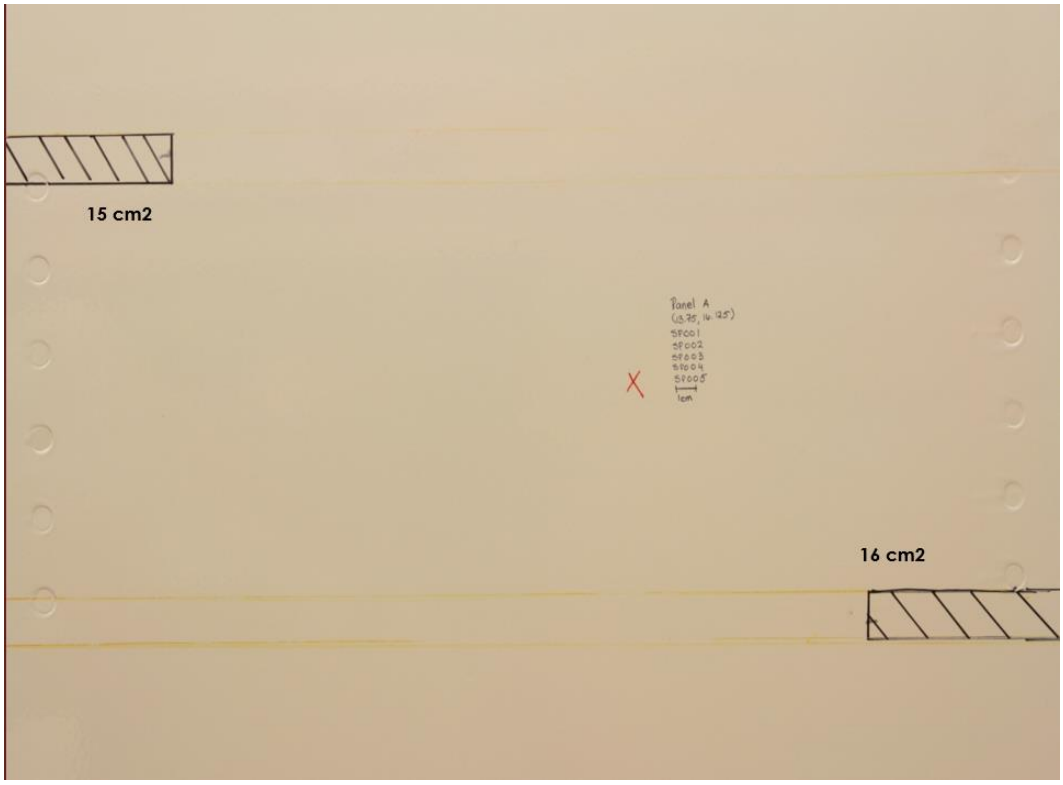

Figure 48. Type I: Front of SP001 (N/A), SP002 (307.2 J), SP003 (430.7 J), SP004 (460.3 J), and SP005 (546.8 J).

Figure 49. Type I: Back of SP001 (N/A), SP002 (307.2 J), SP003 (430.7 J), SP004 (460.3 J), and SP005 (546.8 J).

Figure 50. Type I: Bottom of back of SP001 (N/A), SP002 (307.2 J), SP003 (430.7 J), SP004 (460.3 J), and SP005 (546.8 J).

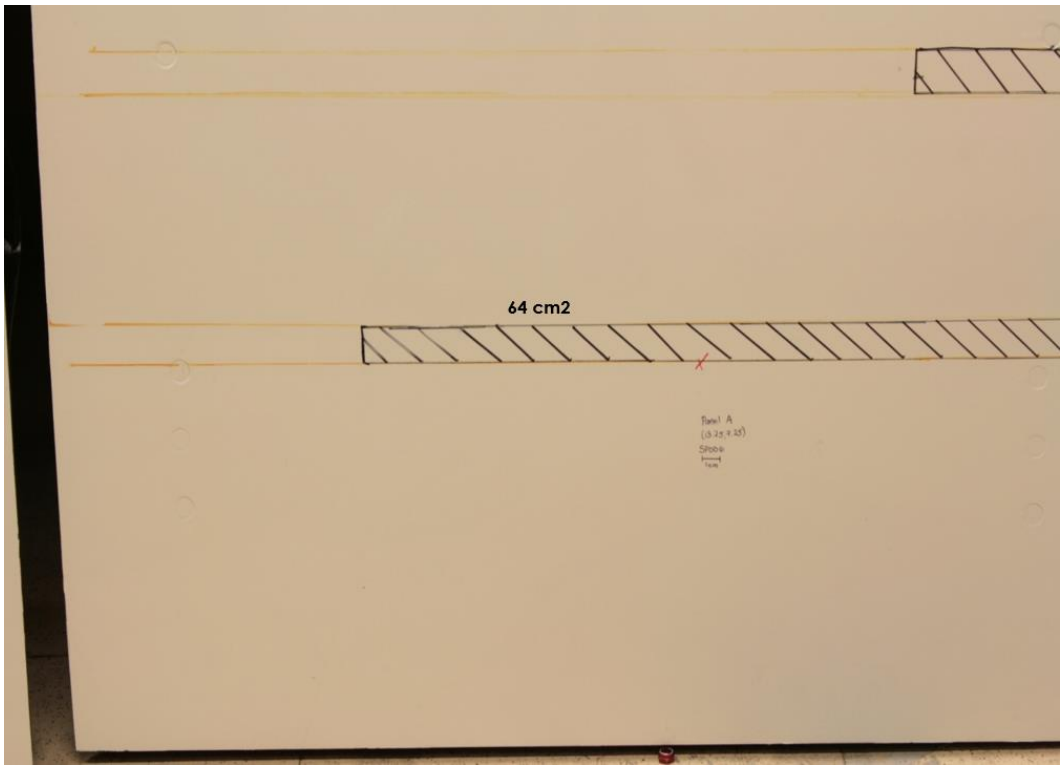

Figure 51. Type IIb: Front of SP006 (420.7 J).

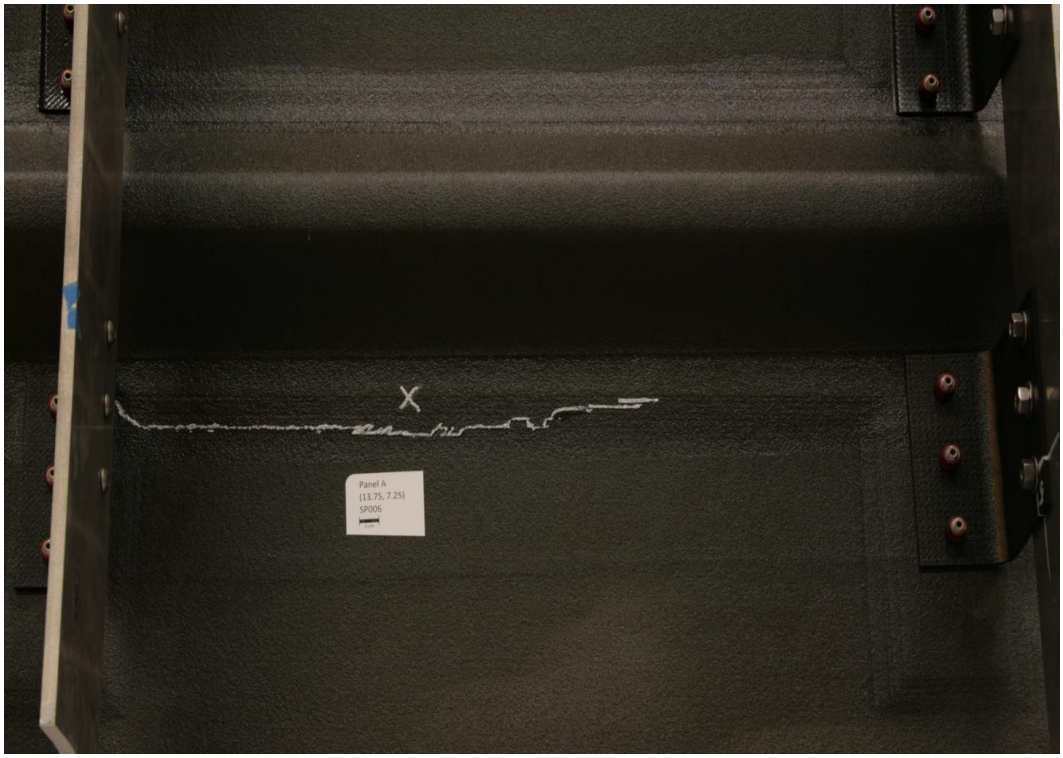

Figure 52. Type IIb: Back of SP006 (420.7 J).

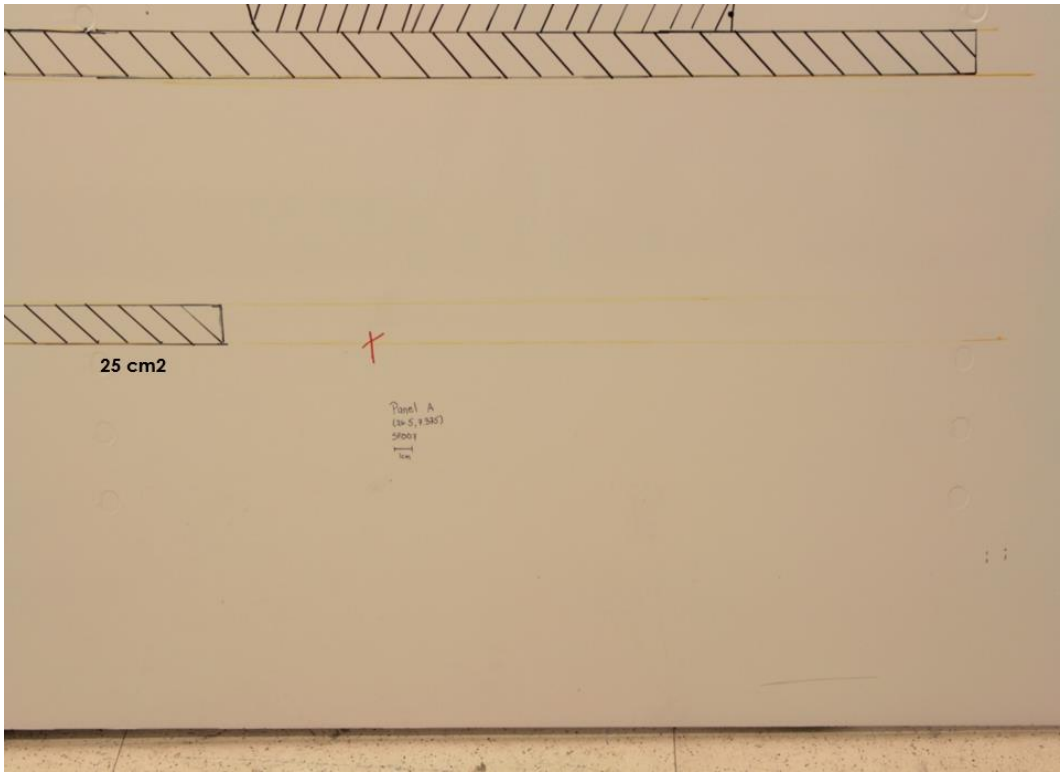

Figure 53. Type IIb: Front of SP007 (277.1 J).

Figure 54. Type IIb: Back of SP007 (277.1 J).

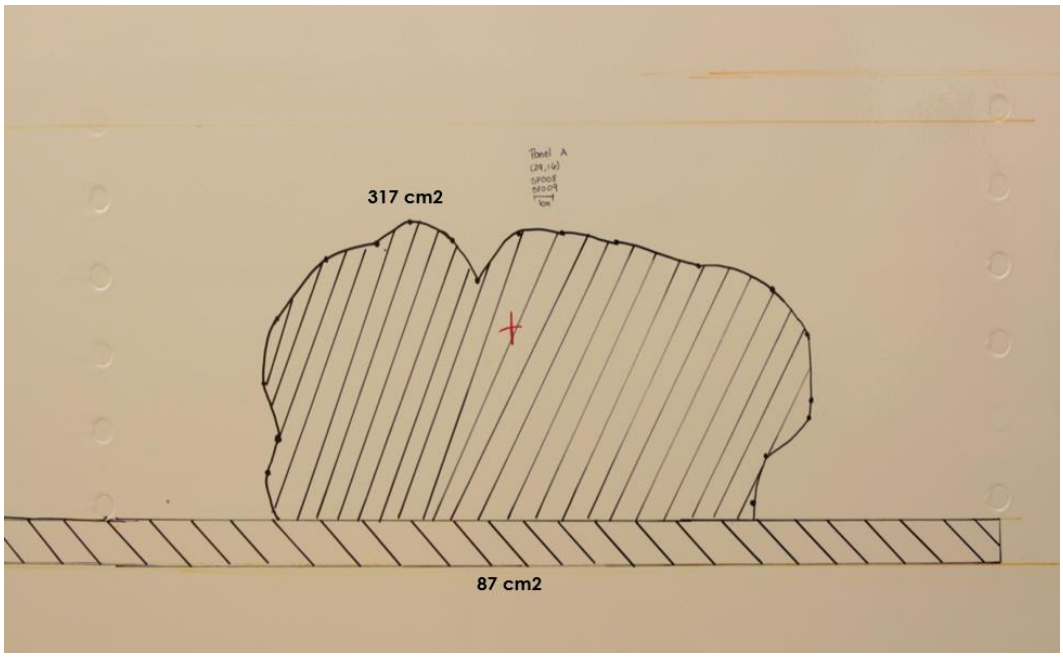

Figure 55. Type I: Front of SP008 (566.5 J) and SP009 (720.5J).

Figure 56. Type I: Back of SP008 (566.5 J) and SP009 (720.5 J).

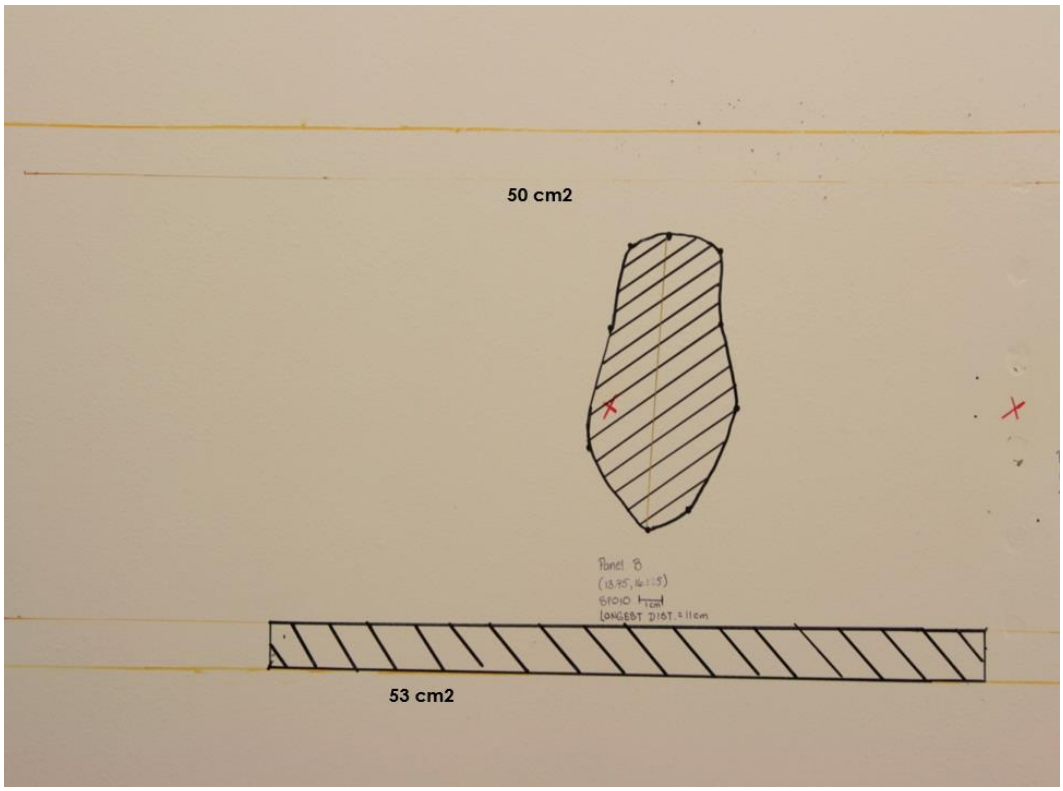

Figure 57. Type I: Front of SP010 (562.3 J).

Figure 58. Type I: Back of SP010 (562.3 J).

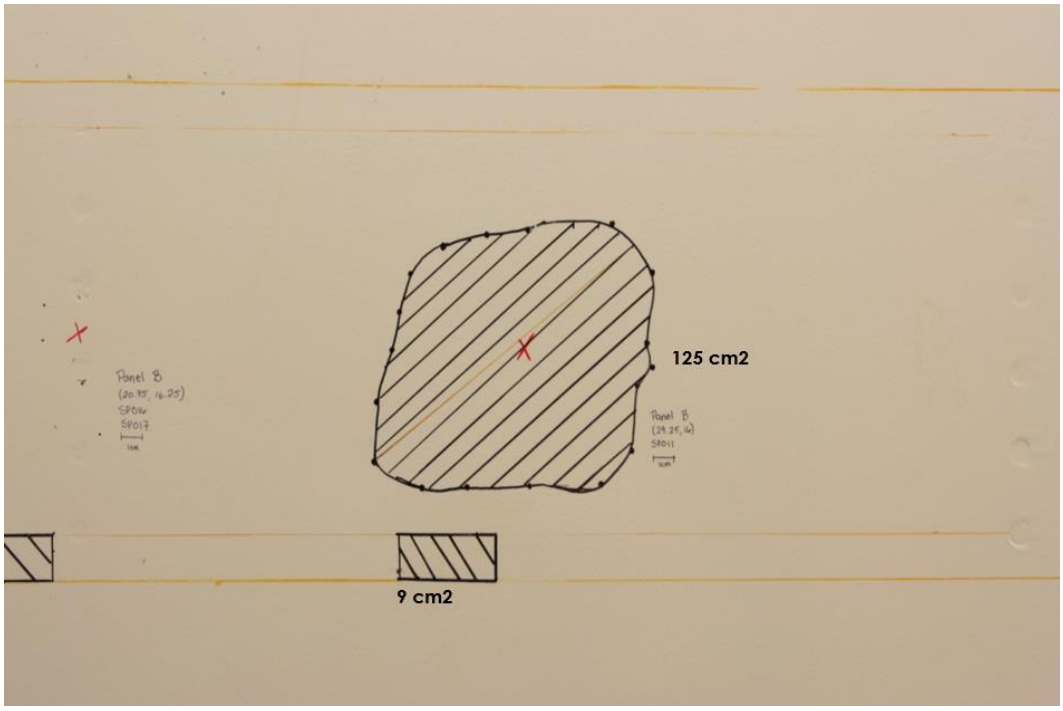

Figure 59. Type I: Front of SP011 (745.6 J).

Figure 60. Type I: Back of SP011 (745.6 J).

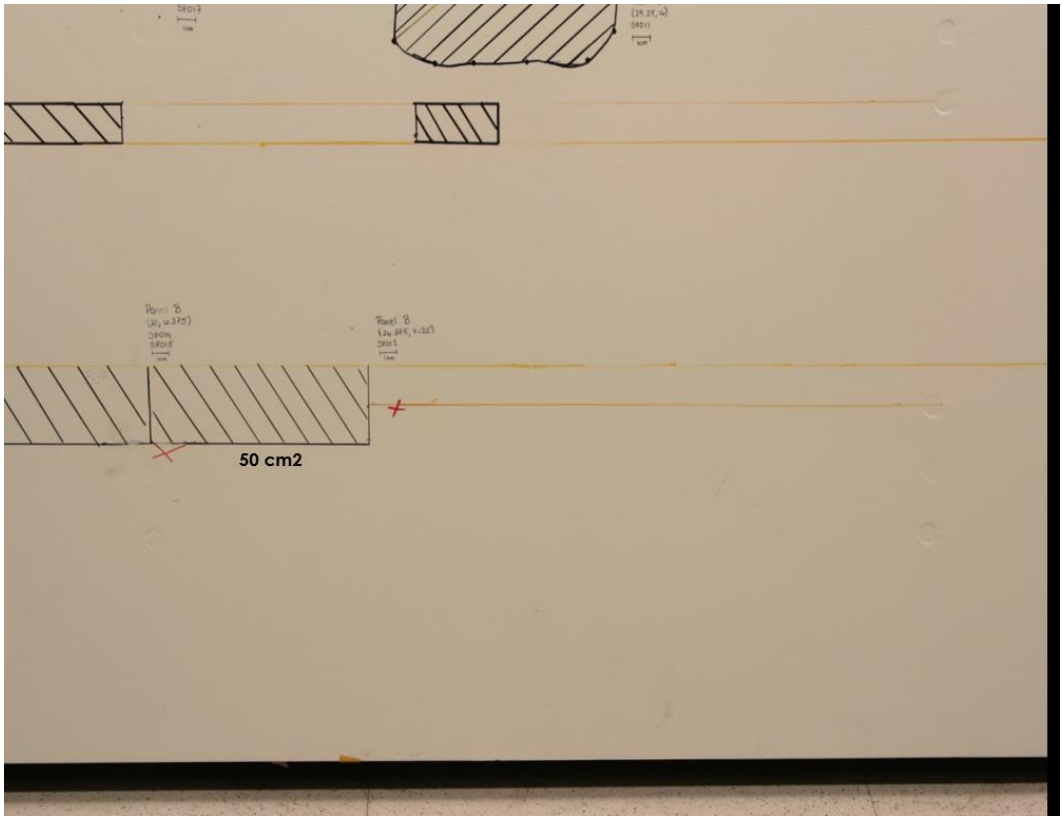

Figure 61. Type IIb: Front of SP012 (284.5 J).

Figure 62. Type IIb: Back of SP012 (284.5 J).

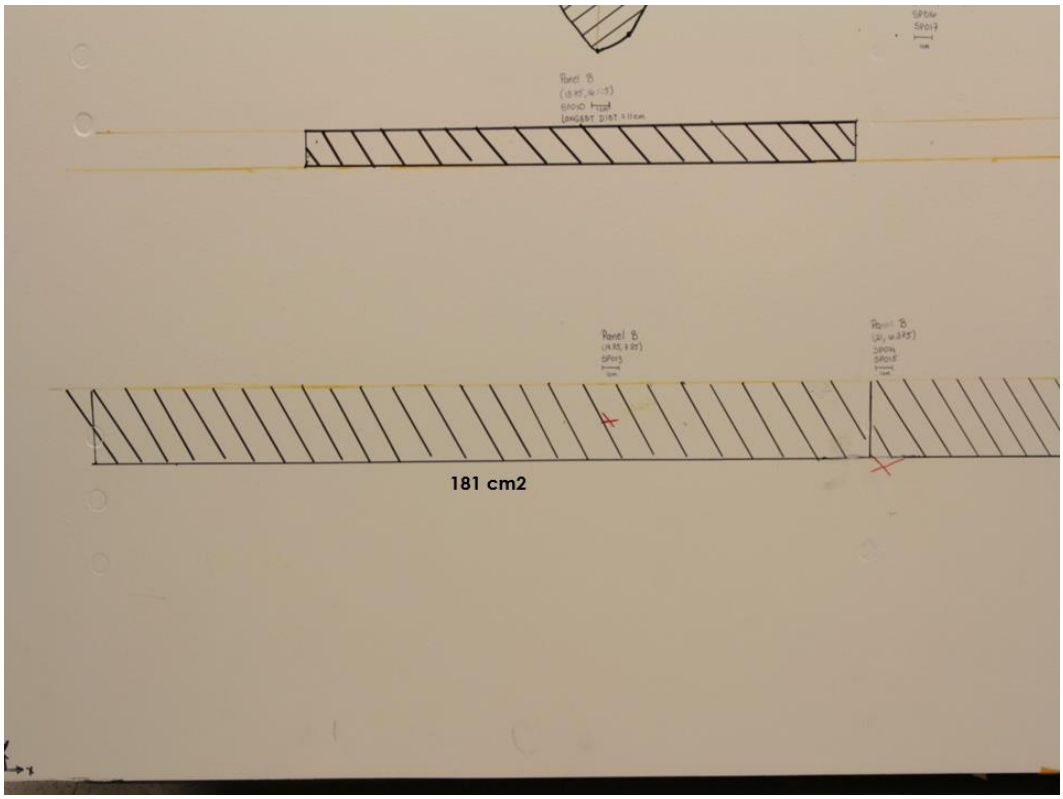

Figure 63. Type IIb: Front of SP013 (279.1 J).

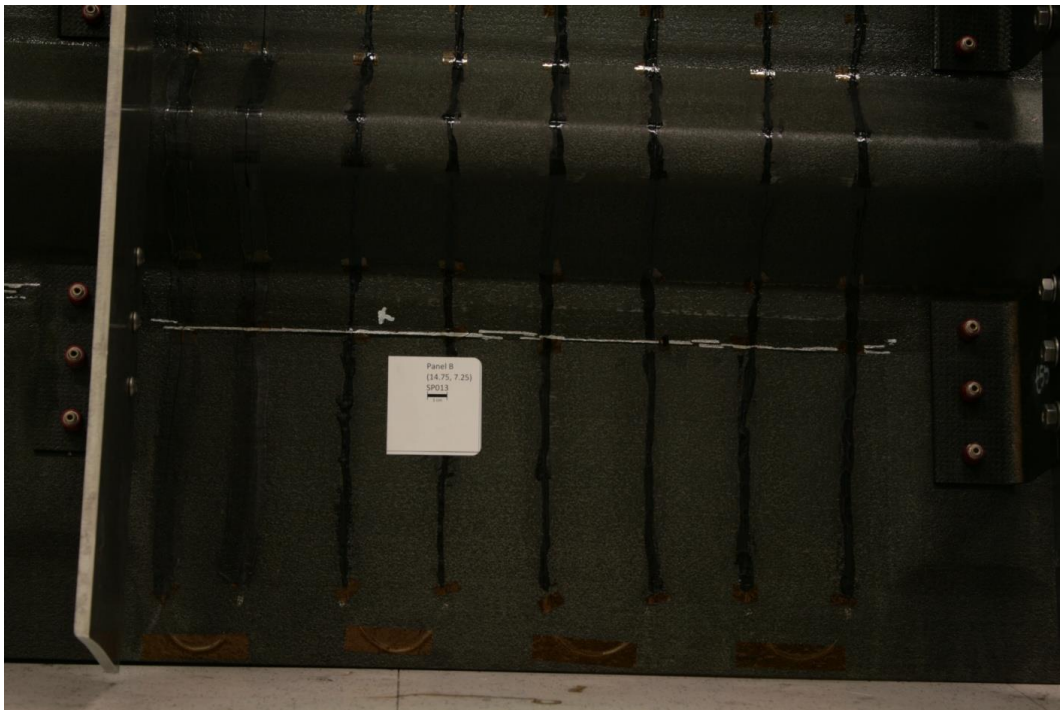

Figure 64. Type IIb: Back of SP013 (279.1 J).

Figure 65. Type IV: Front of SP014 (348.0 J) and SP015 (728.0J).

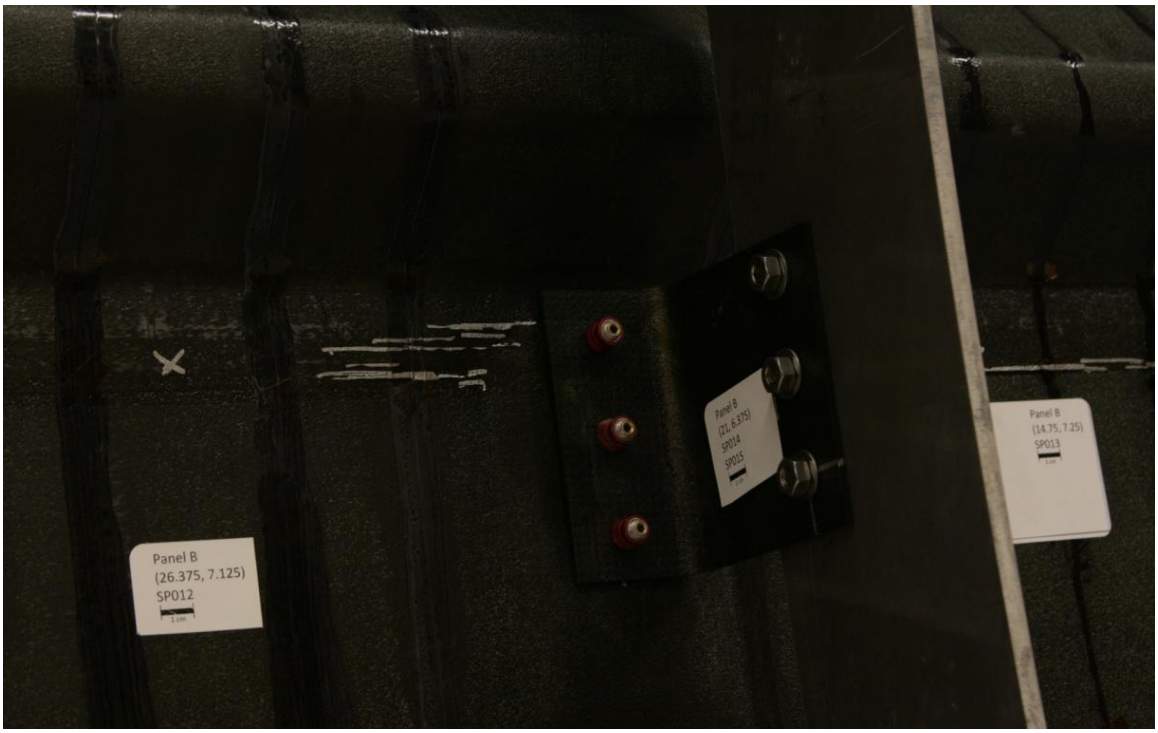

Figure 66. Type IV: Back of SP014 (348.0 J) and SP015 (728.0J).

Figure 67. Type IV: Front of SP016 (476.5J) and SP017 (738.1J).

Figure 68. Type IV: Back of SP016 (476.5J) and SP017 (738.1J).

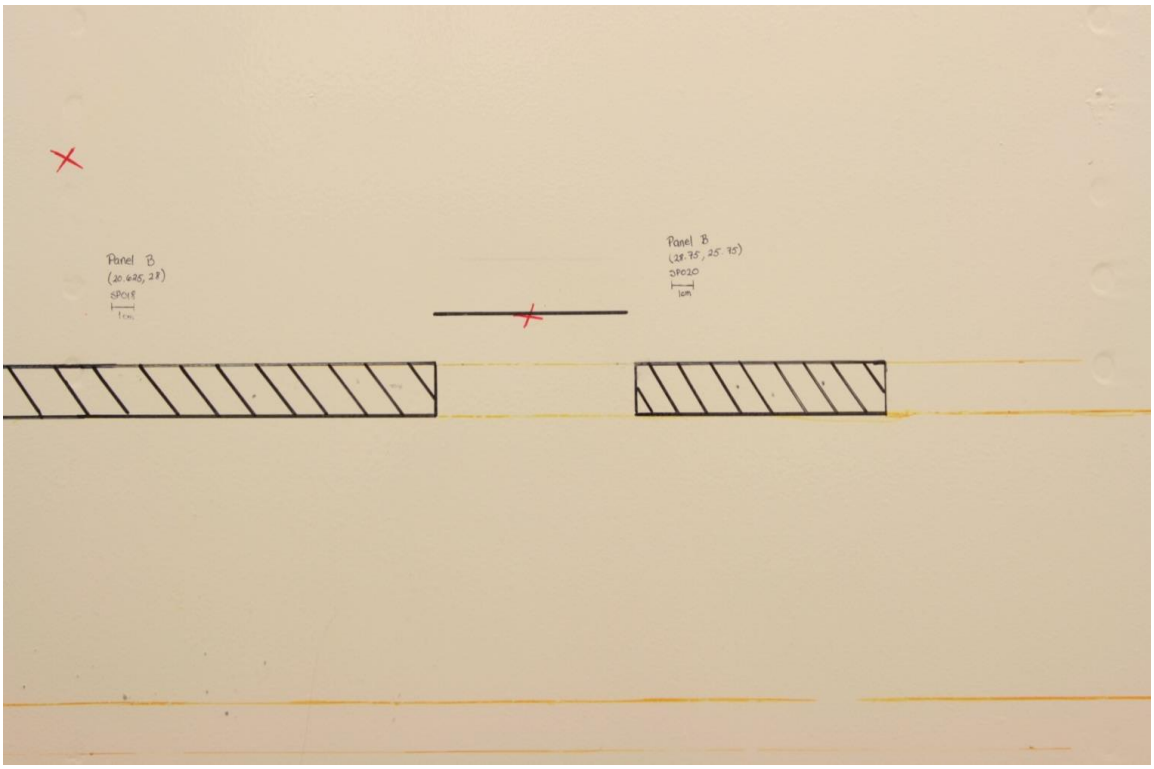

Figure 69. Type IV: Front of SP018 (669.6 J).

Figure 70. Type IV: Back of SP018 (669.6 J).

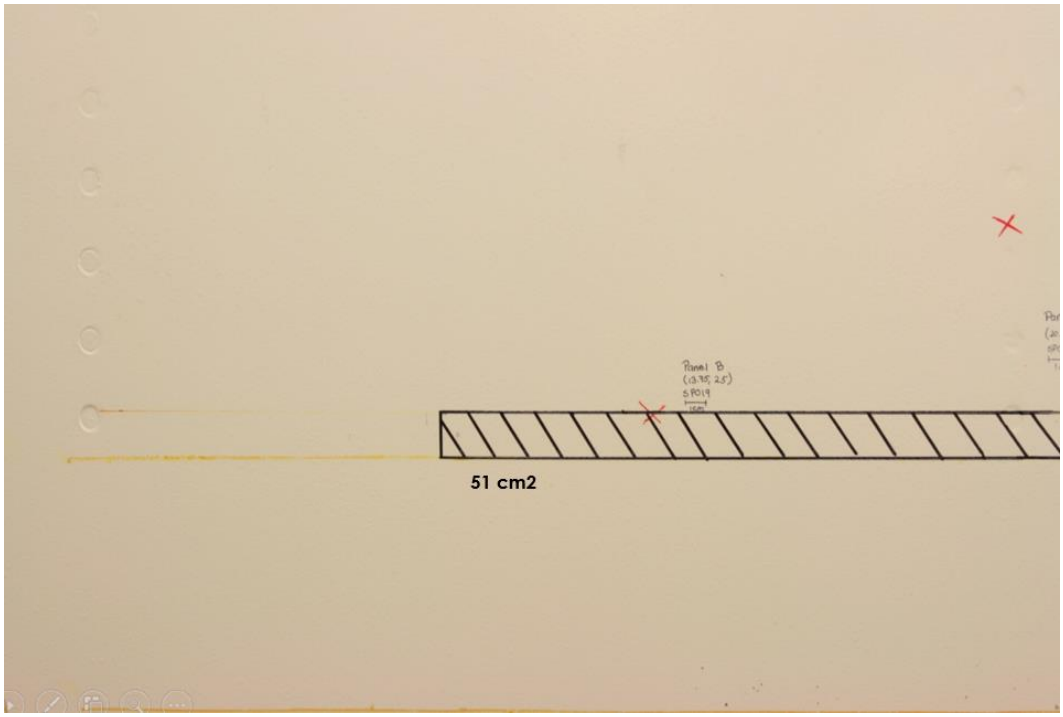

Figure 71. Type IIb: Front of SP019 (201.3 J).

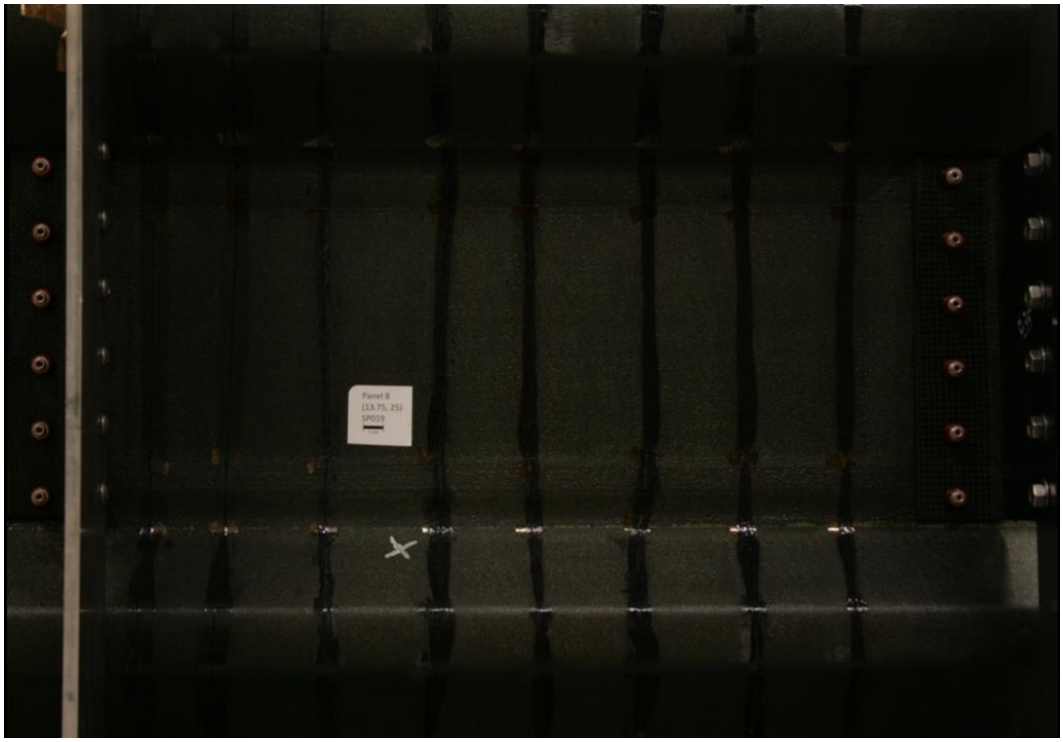

Figure 72. Type IIb: Back of SP019 (201.3 J).

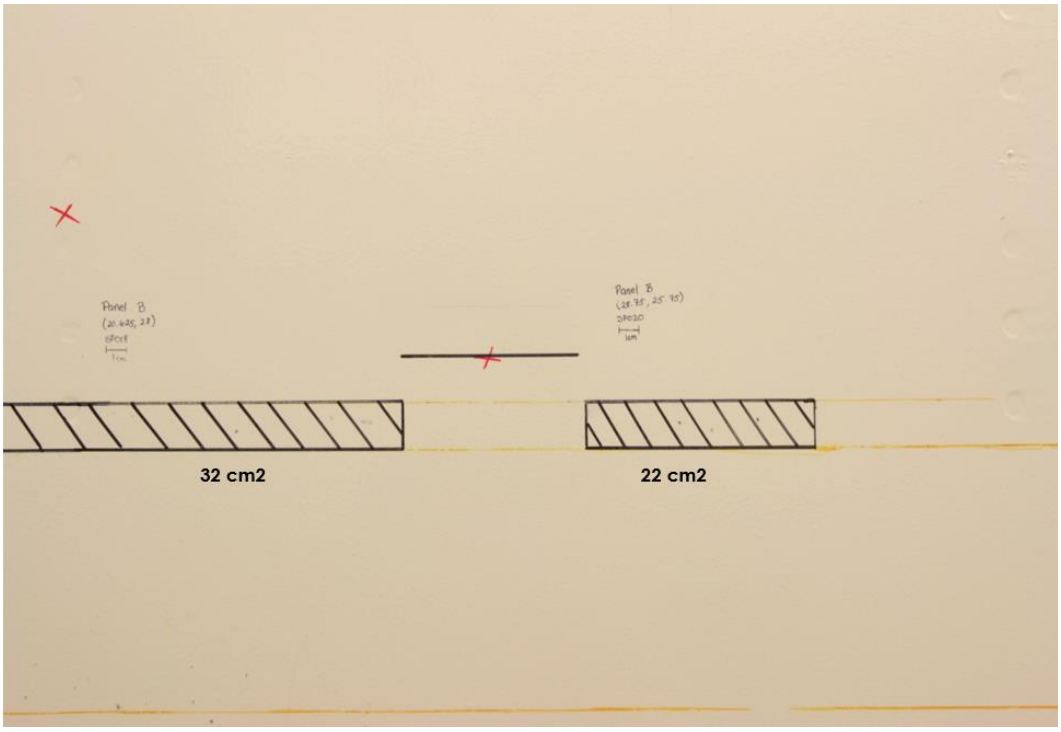

Figure 73. Type IIa: Front of SP020 (172.3 J).

Figure 74. Type IIa: Back of SP020 (172.3 J).

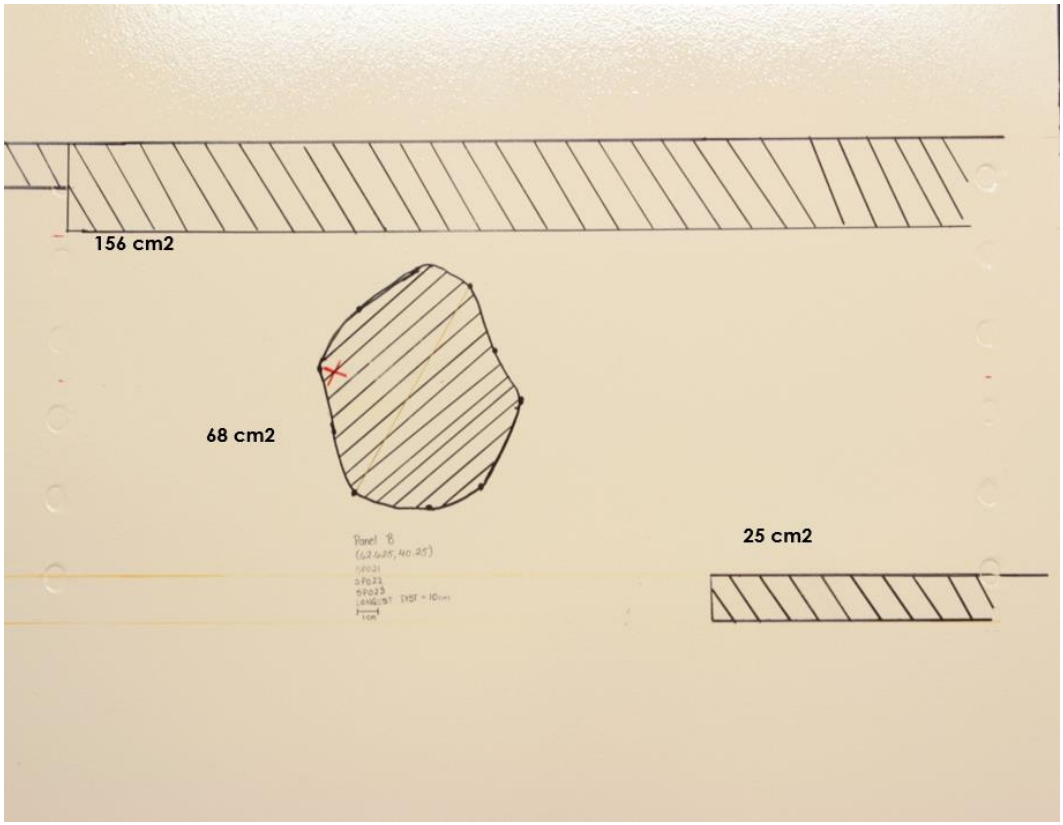

Figure 75. Type I: Front of SP021 (445.0 J), SP022 (540.0 J), and SP023 (665.5 J).

Figure 76. Type I: Back of SP021 (445.0 J), SP022 (540.0 J), and SP023 (665.5 J).

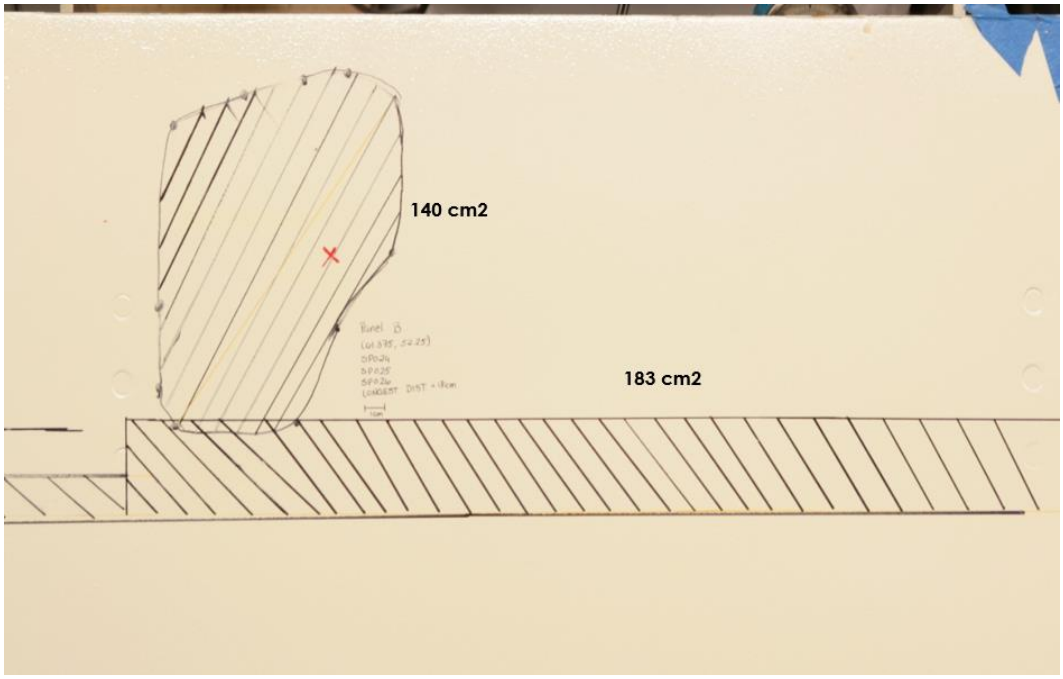

Figure 77. Type I: Front of SP024 (432.9 J), SP025 (550.2 J), and SP026 (734.8 J).

Figure 78. Type I: Back of SP024 (432.9 J), SP025 (550.2 J), and SP026 (734.8 J).

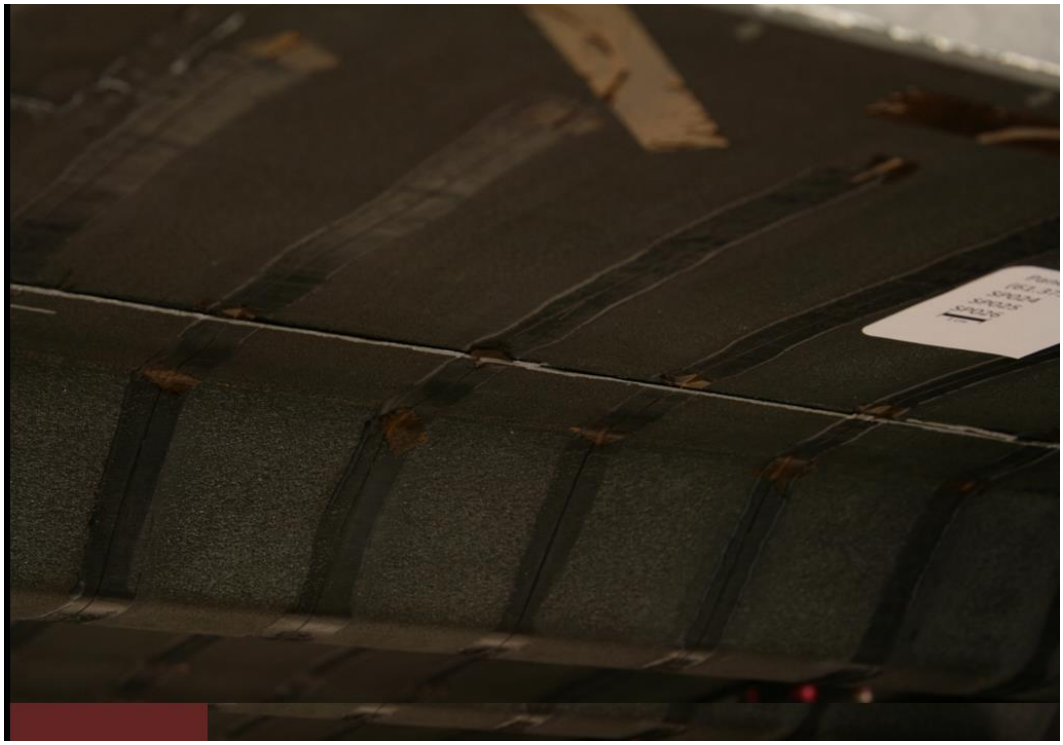

Figure 79. Type I: Unzipping of Flange at Location of Back of SP024 (432.9 J), SP025 (550.2 J), and SP026 (734.8 J).

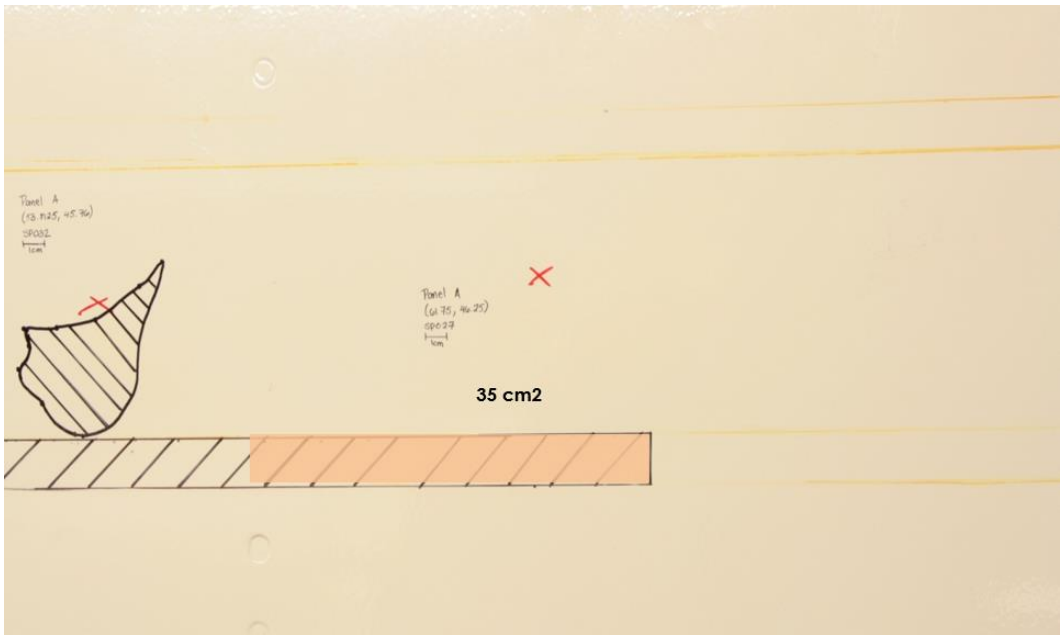

Figure 80. Type III: Front of SP027 (442.3 J).

Figure 81. Type III: Back of SP027 (442.3 J).

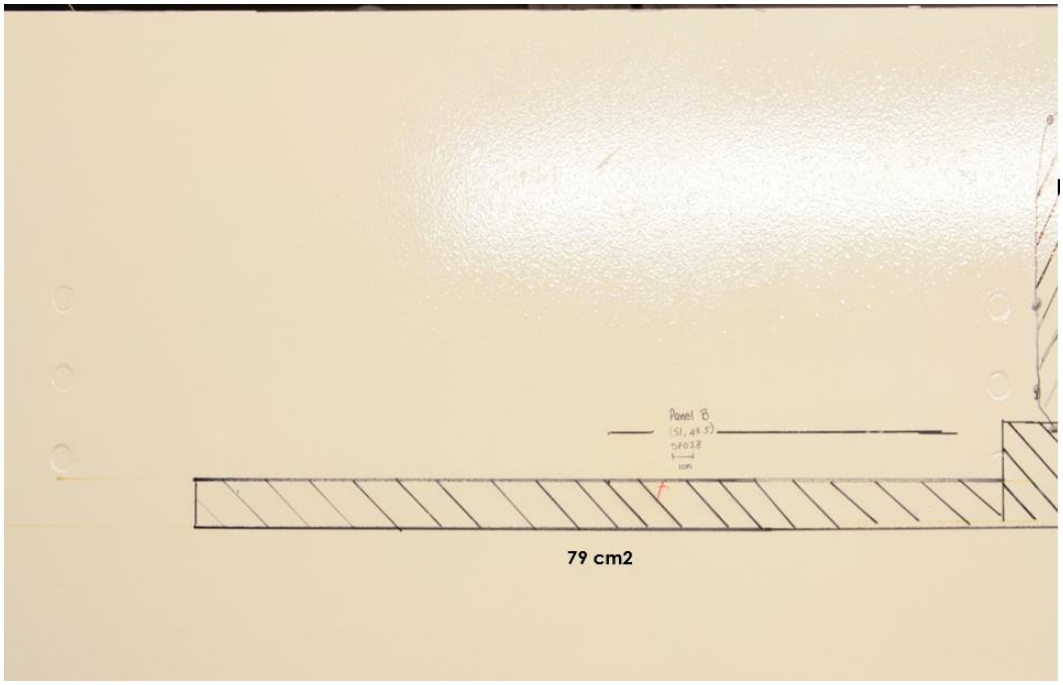

Figure 82. Type IIb: Front of SP028 (383.4 J).

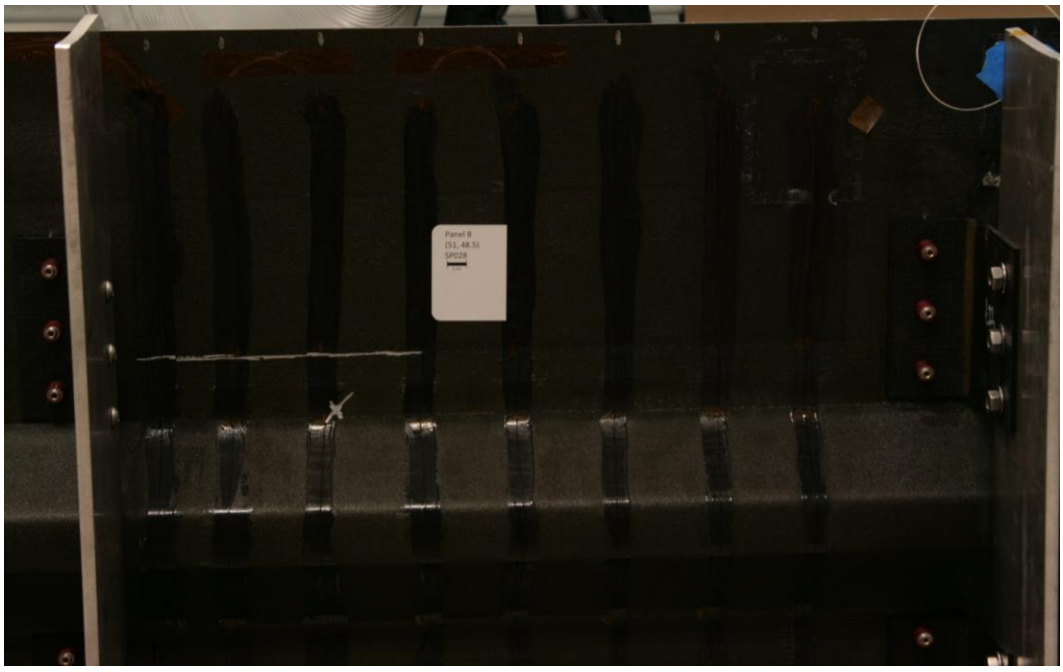

Figure 83. Type IIb: Back of SP028 (383.4 J).

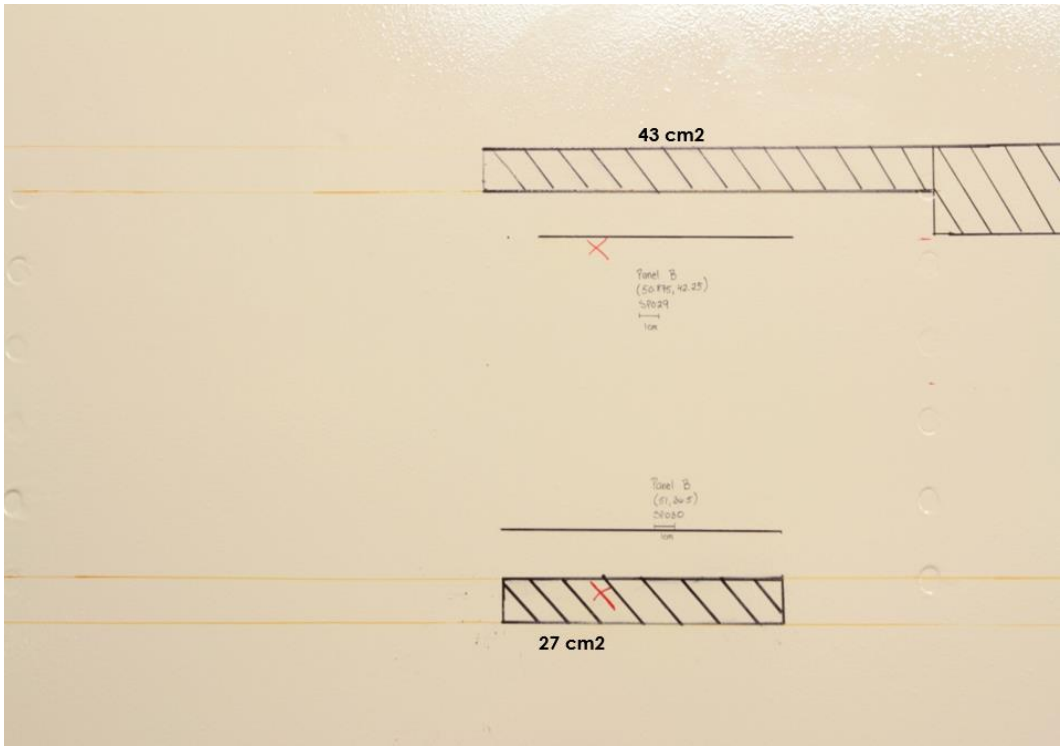

Figure 84. Type IIa: Front of SP029 (423.3 J) and SP030 (407.9J).

Figure 85. Type IIa: Back of SP029 (423.3 J) and SP030 (407.9 J).

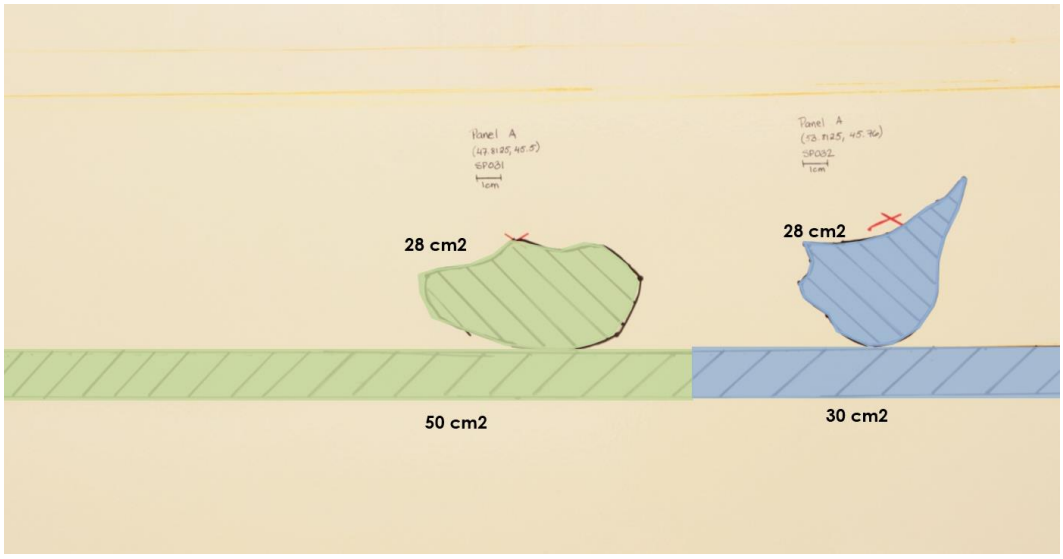

Figure 86. Type III: Front of SP031 (394.8 J) and SP032 (560.8 J).

Figure 87. Type III: Back of SP031 (394.8 J) and SP032 (560.8 J).

Figure 88. Type IIb: Back of SP033 (163.4 J), SP034 (181.2 J), SP035 (226.4 J), and SP036 (275.9 J).

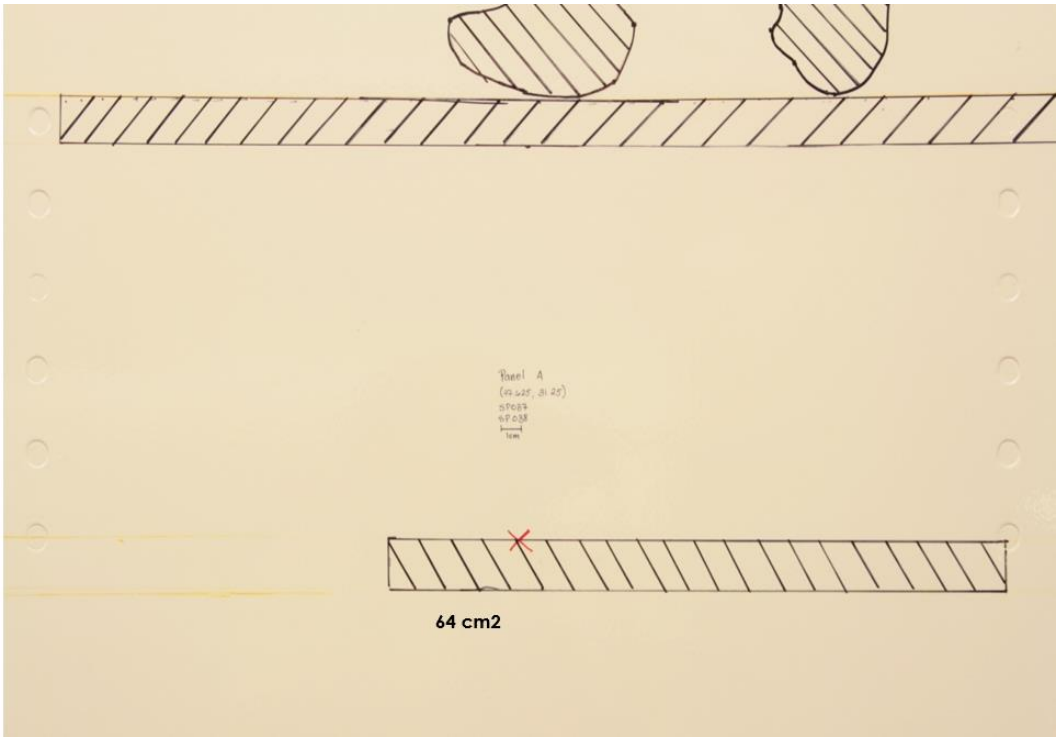

Figure 89. Type IIb: Front of SP037 (241.1 J) and SP038 (264.7 J).

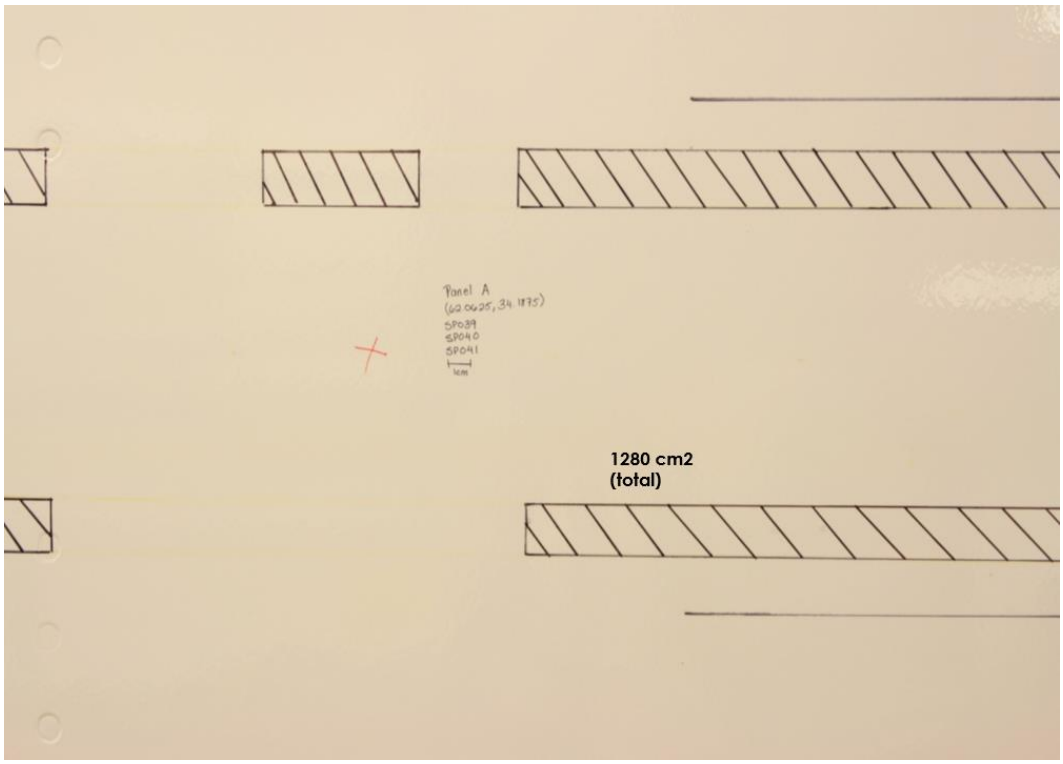

Figure 90. Type III: Front of SP039 (276.5 J), SP040 (331.7 J), and SP041 (388.3 J).

Figure 91. Type III: Back of SP039 (J), SP040 (J), and SP041 (J).

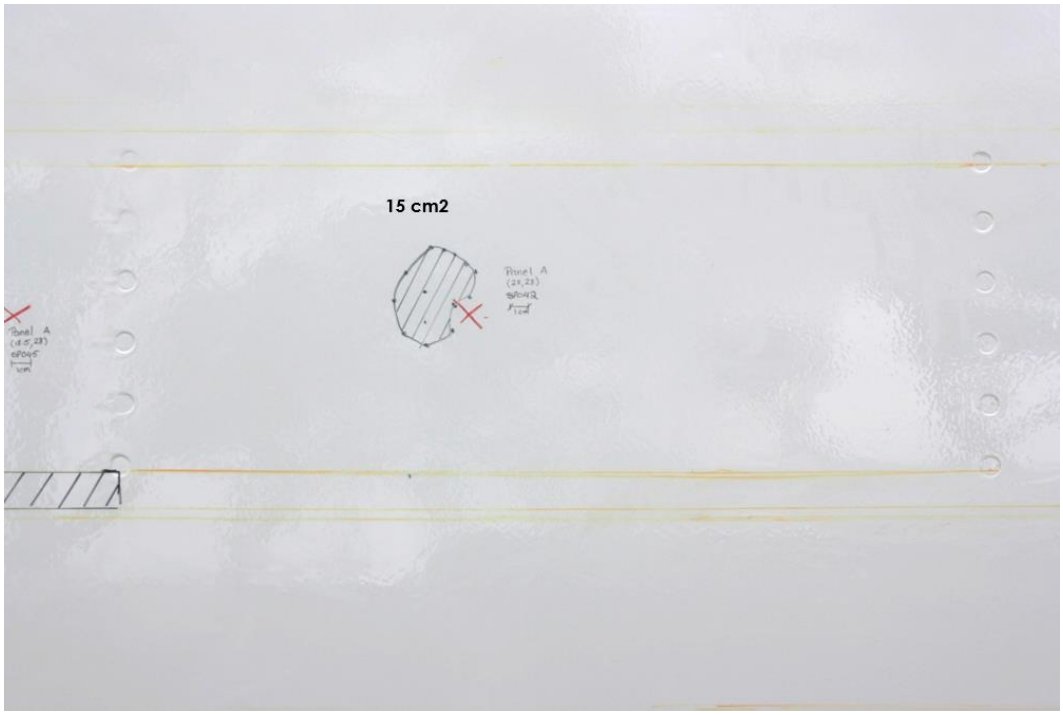

Figure 92. Type I: Font of SP042 (295.4 J).

Figure 93. Type I: Back of SP042 (295.4 J).

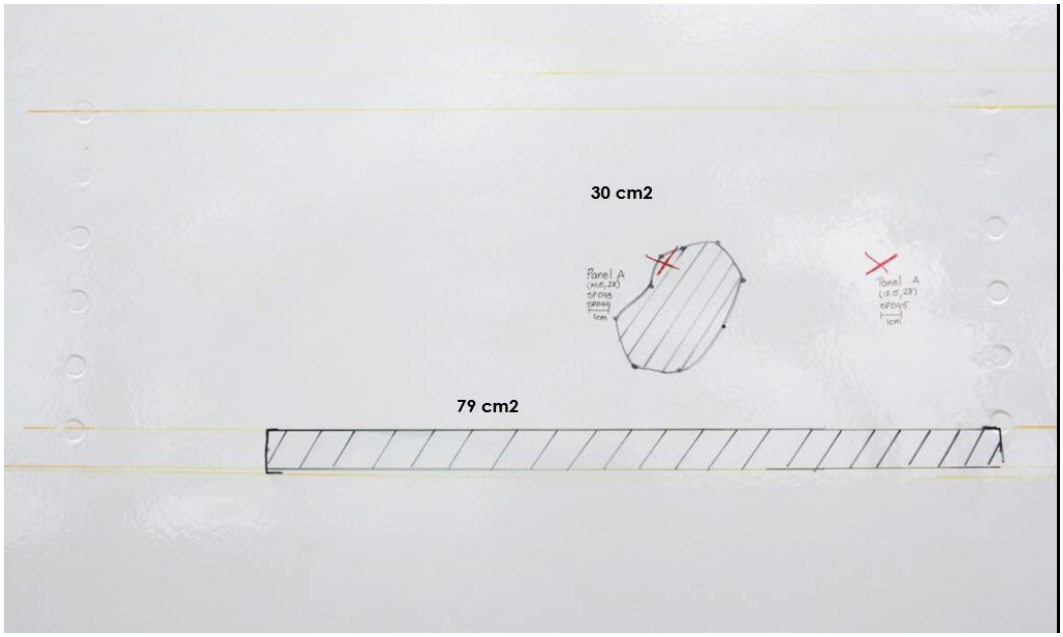

Figure 94. Type I: Front of SP043 (161.2 J), SP044 (227.0 J), and SP045 (347.1J).

Figure 95. Type I: Back of SP043 (161.2 J), SP044 (227.0 J), and SP045 (347.1J).